DOMINIK PASCAL WINDEY

CAVITY-BASED 3D COOLING OF A LEVITATED NANOPARTICLE VIA COHERENT SCATTERING

CAVITY-BASED 3D COOLING OF A LEVITATED NANOPARTICLE VIA COHERENT SCATTERING

A thesis submitted to attain the degree of

DOCTOR OF SCIENCES of ETH ZURICH
(Dr. sc. ETH Zurich)

presented by

DOMINIK PASCAL WINDEY
MSc ETH Physics, ETH Zurich

born on 14 December 1990
citizen of Germany

accepted on the recommendation of

Prof. Dr. Lukas Novotny, examiner
Prof. Dr. Tracy E. Northup, co-examiner
Prof. Dr. Tilman Esslinger, co-examiner

2022

ABSTRACT

After pioneering work on optically levitated particles in the 1970s by Ashkin, so called optical tweezers have not only become a popular tool in biology and medicine but also experienced a renaissance in vacuum trapping over the last ten years. While the broader field of optomechanics already gained popularity previously and investigated the classical-to-quantum transition in cryogenic systems at the beginning of the last decade, levitated particle optomechanics opened the door to room temperature quantum experiments. The versatile levitated particle system has been utilized in various applications, such as rotation experiments at world record speeds exceeding 6 GHz, highly sensitive force sensors or to study stochastic effects of thermodynamics. Most intriguing, however, was the transition into the quantum regime by ground-state cooling of the particle's center-of-mass motion in one dimension, setting the first milestone of genuine quantum experiments.

Ten years after the first cooling attempt, a technique adopted from the atom and ion cooling community finally led to ground-state cooling of a levitated particle. This technique, called cooling by coherent scattering, is the central scheme of this thesis. In the first part of this thesis we describe the construction of a double vacuum chamber system to efficiently trap and transfer a levitated particle into an optical cavity. In contrast to previous systems, no particle transfer to a second tweezer is necessary, minimizing the risk of particle loss and enabling experiments within minutes after particle loading.

In the second part, we present the working principle of our coherent scattering setup. It was the first pure optical trapping configuration to transition a levitated particle into high vacuum, while being stabilized exclusively through cavity cooling. At the time, we achieved record low cavity cooling center-of-mass energies reflected by an effective temperature of a few millikelvin and demonstrated genuine 3D cooling of the motional degrees of freedom.

The central feat of the coherent scattering setup is the ability to cool the particle motion in a cavity field node, reducing the impact of laser phase noise compared to the dispersive regime. In the last part of the thesis, we find that the mechanical instability of the particle position limits the suppression of phase noise, leading to particle cooling to about 10 phonons.

ZUSAMMENFASSUNG

Nach ersten bahnbrechenden Experimenten mit schwebenden Partikeln von Ashkin 1970, gewannen sogenannte optische Pinzetten an Popularität in der Biologie und Medizin. Ausserdem erfuhren sie in den letzten zehn Jahren eine Renaissance als optische Fallen im Hochvakuum. Bereits früher erfuhr das breitere Feld der Optomechanik Berühmtheit und schon am Anfang des letzten Jahrzehnts wurde mit Hilfe der Kryotechnik der Übergang von der klassischen in die Quantenwelt untersucht. Es waren jedoch schwebende Partikel, welche die Welt zu Quantenexperimenten bei Raumtemperatur ermöglichten. Schwebende Partikel, als vielseitig anwendbares System, fanden in verschiedensten Applikationen Anwendung. Dazu gehören die Rotation mit Weltrekord Geschwindigkeit von 6 GHz , hochsensitive Detektoren kleinster Kräfte und die Untersuchung stochastischer Effekte der Thermodynamik. Das interessanteste jedoch war der Übergang in die Quantenwelt durch Grundzustandskühlen der Schwerpunktsbewegung des Partikels – der erste Meilenstein auf dem Weg zu echten Quantenexperimenten.

Zehn Jahre nach den ersten Kühlexperimenten wurde Grundzustandskühlen mit Hilfe einer Technik aus der kalten Atom- und Ionenphysik endlich möglich. Diese Methode des sogenannten „kohärenten Streuens" ist zentrales Thema dieser Arbeit. Im ersten Teil der Arbeit beschreiben wir die Konstruktion einer zweiteiligen Vakuumkammer um Partikel in einer optischen Falle zu fangen und dann in einem optischen Resonator zu platzieren. Im Gegensatz zu vergleichbaren früheren Experimenten benötigen wir keinen Transfer des Partikels in eine zweite optische Falle. Dadurch können wir das Risiko eines Verlusts des Partikels minimieren und ermöglichen Kühlexperimente schon nach wenigen Minuten nach dem Laden der Falle mit einem Partikel.

Im zweiten Teil präsentieren wir die Funktionsweise unseres kohärenten Streuaufbaus. Es war der erste Aufbau, welcher es ausschliesslich mit der Kühlkraft des optischen Resonators geschafft hat, ein Partikel ausreichend zu stabilisieren, damit der Übergang ins Hochvakuum durchgeführt werden kann. Zu diesem Zeitpunkt waren wir in der Lage, den aktuellen Rekord tiefster Schwerpunktsenergien mit einem optischen Resonator aufzustellen. Wir erreichten Schwerpunktsenergien, welche effektiven Temperaturen von wenigen Millikelvin entsprachen. Darüber hinaus sind wir in der Lage, mit

Hilfe des optischen Resonators die Bewegung des Partikels in allen drei räumlichen Dimensionen zu kühlen.

Ein zentraler Vorteil des kohärenten Streuens ist die Möglichkeit, das Partikel im Knoten des elektrischen Feldes des optischen Resonators zu kühlen. Dadurch wird der Einfluss von Phasenrauschen des Lasers, im Vergleich zu Experimenten, in denen der optische Resonator direkt durch einen Spiegel angetrieben wird, reduziert. Im letzten Teil dieser Arbeit berichten wir, dass die mechanische Stabilität der optischen Falle die Unterdrückung des Phasenrauschens limitiert und dadurch eine Besetzungszahl des mechanischen Oszillators von ca. 10 Phononen erreicht wird.

FOREWORD

I could not present the results of this thesis without the contributions from various sides. In this chapter, I want to give credit to those involved and summarize their contributions. Initially the cavity team consisted of postdoc René Reimann and me. René designed the vacuum setup and custom components shown in Figs. 2.1, 2.2, 2.4 and 2.11 and started the assembly with the help of semester students. We completed the assembly together and I eventually redesigned the parts for the second generation trapping lenses and cavity mirrors. He taught me everything I needed to know to succeed in an optics lab and remained an invaluable discussion partner even after his departure to start his own lab in Abu Dhabi. The results presented in Chapter 3 were measured by me and interpreted with René. We could not have connected all the dots ourselves in a busy time without the great help of Carlos Gonzalez-Ballestero, Patrick Maurer and Oriol Romero-Isart. The theoreticians from Innsbruck developed a full theory describing our experiments and guiding our efforts to further improve the setup which I rely on in Chapter 4.

During 2020 the cavity team grew with the addition of PhD student Johannes Piotrowski and postdoc Jayadev Vijayan. Together we disassembled the whole setup and rebuilt it in the basement to improve mechanical stability. Johannes and I shared all lab work with the support of Jayadev, characterized the second generation trapping lenses and cavity mirrors and acquired the latest cooling results together that are presented in Chapter 4. Johannes designed and implemented the new two tweezer system pictured in Fig. 4.14.

I want to particularly mention the contribution of Erik Hebestreit who gave insight during the design of the vacuum setup and who built the quadrant photodiode we used to measure the data presented in Chapter 3. Felix Tebbenjohanns and Karol Luszcz advised with building custom electronic components. Karol helped to significantly reduce the electronic noise on the cavity lock. Martin Frimmer proposed the method for estimating the Stokes scattering rate in Sec. 2.2.1. The results benefited greatly from discussions with my supervisor Lukas Novotny and the other trappers Patrick Back, Laric Bobzien, Eric Bonvin, Rozenn Diehl, Jialiang Gao, Vijay Jain, Fons van der Laan, Maria Luisa Mattana, Andrei Militaru, Massimiliano Rossi and Joanna Zielinska.

CONTENTS

1

INTRODUCTION

Optomechanics explores the interaction between light and mechanical motion [1] placing the field at the intersection between two domains of classical physics, namely classical mechanics and electrodynamics. For decades mechanical objects have been described as ideal particles that can be fully localized and have a mass and electric charge identifiable with infinite precision. On the contrary, light was described as an ideal wave, characterized by a frequency or wavelength but completely delocalized in space [2]. According to classical mechanics we can measure an object's position and momentum to infinite precision which contradicts Heisenberg's uncertainty principle, setting a fundamental limit at $\hbar/2$ [3, 4]. The uncertainty principle is a central statement of quantum mechanics, a domain that emerged in the 1920s to explain the failure of Newtonian mechanics in the world of atoms [5] as well as the quantization of light as observed in the photoelectric effect [6–9] and eventually unifying the particle-wave picture [10]. In the age of modern physics, the quantum mechanical theoretical framework to study the fundamental interaction of light and mechanics has been developed. However, to create a measurable effect, experimental regimes have to be chosen very carefully. In 1873 Crookes attempted to explain the motion of the vanes of his radiometer by the repulsion of light [11], although this explanation was incorrect. It was eventually understood as a thermal effect [12, 13]. The first effect of radiation pressure on macroscopic objects was shown by Lebedew [14], as well as Nichols and Hull [15] at the beginning of the 20th century, using a modified version of the radiometer. Later, Frisch measured the deflection of an atomic beam, induced by the absorption of light [16]. Pioneering work of was achieved around the 1970s by Arthur Ashkin through trapping and manipulation of small particles [17, 18] and by Vladimir Braginsky who detected mechanical damping arising from radiation [19, 20].

In optomechanical systems one typically tries to reduce the size of the mechanical oscillator to increase its susceptibility to a weak optical force and boost the latter with the use of strong lasers or optical resonators. It therefore took almost 30 years until micro- and nanofabrication techniques as well as light sources advanced sufficiently to cool a mechanical mode with radiation pressure in 1999 [21] and eventually a plethora of platforms evolved to

maximize the light-oscillator interaction [22–30]. While scientists at the Laser Interferometer Gravitational Wave Observatory (LIGO) investigated the relevance of radiation forces for gravitational wave detection [31] many platforms had the common goal of ground-state cooling the mechanical oscillator through passive or active laser cooling techniques. Ground-state cooling of a mechanical resonator was first reported in 2010 by placing a ceramic drum resonator inside a dilution refrigerator without any laser cooling involved [32]. Soon after, the first groups also entered the quantum regime with laser cooling techniques [33, 34]. Prior to optomechanical systems various degrees of freedom of atoms [35–37] and ions [38–42] have been cooled to the quantum ground-state.

Levitated particles were among the first optomechanical systems to be studied in the 1970s and optical tweezers became a standard tool in biology and medicine in the beginning of the 21st century [43–46]. The levitated optomechanics community gained momentum in 2010 by first levitating and cooling silica microparticles in dual beam configurations [47, 48] and eventually nanoparticles in a single laser beam [49]. Various cooling techniques were employed to reduce the particle's center-of-mass motion i.e. linear feedback cooling with additional laser beams [47, 50] or by parametric feedback cooling through laser intensity modulation [49, 51–53] as well as resolved sideband cooling with optical cavities [54–58]. Initial cavity cooling protocols pumped the cavity through the mirror and trapped the particle directly in the cavity potential [59, 60], or considered a far detuned optical tweezer to separate the trapping mechanism from the cooling mechanism [61]. To simultaneously cool multiple spatial degrees of freedom of the particle, coupling to higher order cavity modes was considered [62]. Experimentally direct cavity pumping in the resolved sideband regime is ultimately limited to phonon temperatures of a few millikelvin by laser phase noise [63].

Finally, technological advances in the field of levitated optomechanics led to ground-state cooling, first in cavity systems and shortly thereafter in free space configurations. The cavity system adapted a coherent scattering configuration which had been successfully employed in the trapped atom and ion community in the past [64–67] and will be described in detail in this thesis. First coherent scattering cooling results were shown in 2019 [68, 69] with ground-state cooling one year later [70]. The technological advantages of cavity-based cooling by coherent scattering are twofold. Firstly, as light is deflected from the tweezer into the cavity we can cool the particle motion in the tweezer and cavity directions. By tilting the polarization w.r.t. the

cavity we can stabilize the particle along three axes, without a need for additional feedback mechanisms. Secondly, the interference of the tweezer and cavity fields leads to maximal optomechanical coupling of the motion along the cavity axis for the particle placed in the node of the cavity field, or equivalently, where the intensity is minimal and laser phase noise has a reduced impact. Free space systems on the other hand, capitalized on an enhanced read-out of the longitudinal motion in a backscattering configuration [71] in combination with an effective linear feedback scheme coupling to the particle's charge instead of an all-optical system [72–75].

Compared to other optomechanical systems levitated optomechanics can reach ground-state without the need for cryogenic environments as the system has no direct contact with its environment. The technological simplicity and high sensitivity make levitated optomechanics an intriguing platform for force, torque or acceleration sensing applications [76–81]. Furthermore levitated particles have been studied as rotors [82–86], librators [87–89] or as a platform for spectroscopy [90–93] or thermodynamics [94–96] and entered the strong coupling regime [97]. After reaching the hallmark of ground-state cooling and the development of advanced loading techniques [98] to reach ultra high vacuum and reducing decoherence rates, the path to genuine quantum applications are opened, as discussed by Gonzalez-Ballestero et al. [99]. Among them are the creation of non-classical states, motional entanglement, quantum delocalization and eventually quantum many-particle systems, macroscopic superposition and quantum metrology [100–102].

This thesis is structured as follows. In Chapter 2 we introduce our levitated particle cavity machine. Following the approach of [56] we implement a two vacuum chamber setup, one for trapping particles and one for cavity cooling with a mobile optical trap to prevent contamination of the mirrors in the loading process. We first explain how to operate the setup as a whole and eventually focus on the two core components, first the optical tweezer and eventually the optical cavity. To motivate our choice of components we introduce the physics necessary to derive the figures of merit that guided our decisions on the way. We finish the chapter by explaining detection techniques that we apply throughout the work. After establishing a good understanding of the machine we continue in Chapter 3 with our first cooling experiment and introduce the physics behind cavity-based cooling by coherent scattering. The experimental results and theoretical descriptions are largely based on [68] and [103] respectively. In Chapter 4 we investigate the theory from [103] in more detail to motivate modifications of the setup that should facilitate ground-state cooling. We determine trap displace-

ment noise originating from laser phase noise as the limiting factor in our ground-state cooling endeavours and discuss how to reduce the influence and eventually reach the hallmark in the future.

2

A VERSATILE LEVITATED PARTICLE CAVITY MACHINE

In this chapter we describe the cavity machine that we assembled to detect and manipulate the center-of-mass (c.m.) motion of levitated nanoparticles. Initially we focus on the operation of the high vacuum system as a whole consisting of two chambers - the trap and the science chamber - with a manual transfer system. Thereafter we describe the two components that lie at the heart of our experiments, first the optical tweezer and then the cavity. Over the course of the PhD some modifications have been implemented to improve the setup or steer it in a different direction than initially anticipated. We will refer to them as first and second generation components. In Chapter 3 we present experiments conducted with the first generation lenses and mirrors, explain their shortcomings and consequently continue to focus on the second generation in Chapter 4.

2.1 HIGH VACUUM CHAMBER

Every experiment dictates a set of requirements for the vacuum setup which can contradict each other and require compromise. The goal of our experiment is to trap a levitated nanoparticle, to reduce the pressure sufficiently far until its motion is not significantly affected by surrounding gas molecules anymore and to bring the particle into an optical cavity to scatter light into the cavity mode. The details and motivations for all these steps will be described in the following chapters, here we want to mention their consequences for our high vacuum setup. To load a particle we have to be able to vent the vacuum chamber to ambient pressure, open it and spray a particle solution into the chamber. On the other hand, to ensure that the major contribution to the particle damping is not given by residual gas scattering, but by photon recoil, the pressure needs to be reduced to less than 10^{-8} mbar [51]. Finally, to amplify the power of light scattered into the optical cavity we use high finesse mirrors $\mathcal{F} > 50$k. We define the cavity finesse formally in Eq. (2.13). It can be understood as a figure of merit to indicate the reflectivity of the mirrors. The higher the finesse, the closer the mirror reflectivity is to unity, which leads to a higher amplification of the incoming optical field inside the cavity. Solvent residues and glass
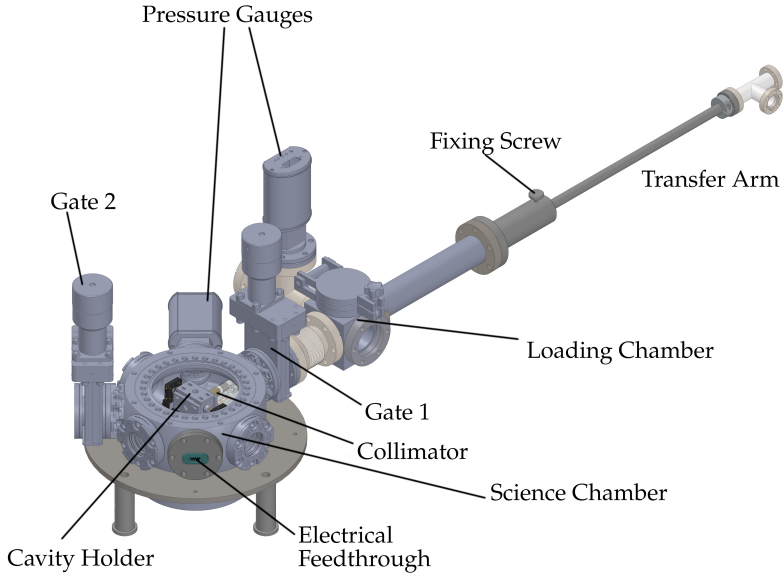
Figure 2.1: *Angled top view of high vacuum setup.* The full setup has a length of about 1.2 m from gate 2 until the edge of the transfer arm. The setup consists of two vacuum chambers, the science and the loading chamber. The science chamber can be sealed from the rest of the setup by closing gates 1 and 2. We use two pressure gauges to separately measure the pressure of the two chambers. The transfer arm, a hollow spring-loaded tube, can be pushed into the vacuum setup to move the optical tweezer from the loading into the science chamber. Not shown here are the top viewport of the science chamber, the angle valve to slowly evacuate the loading chamber, the turbo and scroll pump as well as their bellows connecting to the vacuum setup. Furthermore, not displayed are the optical fiber feedthrough, which is providing the trapping light, as well as the electric feedthrough for the nanopositioner which connects to the T-piece of the transfer arm.

particles on the mirror surface degrade the finesse significantly and prevent us from trapping the particles directly inside the cavity. These aspects lead to the conclusion to build separate loading and science chambers. The loading chamber is compact to minimize the volume that is vented with dry nitrogen to reach low pressures again after the loading procedure. The science chamber is large enough to house the cavity and can be isolated to remain at low pressure even while loading. We adopt a technique developed by Mestres et al. [56] using a mobile optical trap but initially avoid a transfer into a second stationary optical tweezer to reduce complexity.

Other experiments avoid the transfer setup by manually removing the cavity during the loading process and reinsert it afterwards as shown by Delić et al. [104]. Furthermore, Bykov et al. showed that particles can be launched from aluminum foil via acoustic desorption and trapped directly inside a Paul trap in high vacuum. In the future this technique could be extended to directly trap into an optical trap at moderate to high vacuum to bring the setup into the ultra high vacuum (UHV) regime. Moreover, the directionality of the loading technique could make it possible to directly load between the cavity mirrors without contaminating them.

The full vacuum setup is shown in Fig. 2.1 from a top angle and as a cross-section in Fig. 2.2. We explain the process of trapping a particle and coupling it to an optical cavity in Secs. 2.2 and 2.3 and want to focus on the working principle of the vacuum setup as a whole before. The key components of the high vacuum setup can be found in Tab. A.1 with their corresponding supplier and part number. We use a turbo and a scroll pump to evacuate the whole system. The science chamber, containing the optical cavity, can be sealed from the rest of the setup by closing gates 1 and 2. At the cavity facing end of the transfer arm the tweezer assembly is mounted. It consists of a collimator connected to a single mode fiber and is attached to a nanopositioner. A custom lens holder described in Sec. 2.2 attaches to the collimator, forms the optical trap and collimates the beam again. After loosening the fixing screw we can push or pull the transfer arm to move the tweezer assembly between the science and loading chamber. The transfer arm is a hollow tube which contains an optical fiber as well as wires contacting the nanopositioner. We don't show the angle valve which can be used to slowly evacuate the loading chamber after trapping a particle, while the science chamber is sealed. We monitor the pressures of both chambers separately to avoid opening the gates at too high pressure difference ($\Delta p > 25\,\text{mbar}$). To trap and transfer a particle to the science chamber we follow this protocol:
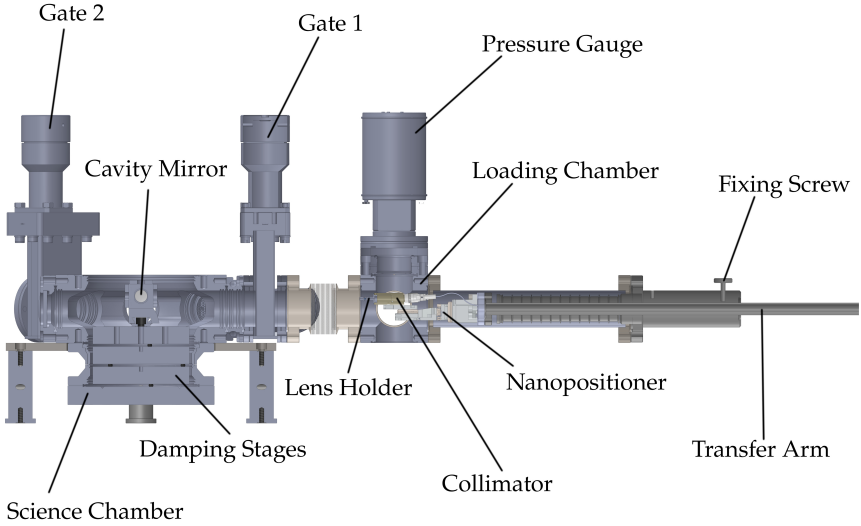
FIGURE 2.2: *Side view of high vacuum setup cross section.* The setup shown in Fig. 2.1 is cut vertically to visualize the transfer system. The optical cavity is located in the science chamber on a stack of damping stages. In the displayed configuration the transfer arm is almost completely pulled out, positioning the tweezer assembly close to the loading chamber. Not shown are the optical fiber and wires connecting to the nanopositioner which are fed through the hollow transfer arm. After loosening the fixing screw and opening gate 1 we can push the transfer arm to move the lens holder, collimator and nanopositioner assembly into the science chamber. Behind gate 1 on the side facing the science chamber we install a mechanical stop (not shown) which blocks the arm from moving in too far and provides a support to improve the arm's mechanical stability.

We assume the setup is evacuated, the transfer arm is pulled out of the science chamber and the angle valve is opened.

1. Close gates 1 and 2[1].

2. Vent the setup (loading chamber) with dry nitrogen[2].

3. Open the loading chamber (by removing a blind flange) and trap a particle with a nebulizer as described in Sec. 2.2.

4. Stop venting and close the loading chamber (by installing the blind flange again) without causing air turbulence of mechanical shocks close to the setup.

5. Close the angle valve[3].

6. Evacuate the setup with the scroll pump only and slowly open the angle valve[4].

7. Open gates 1 and 2 and loosen the the fixing screw.

8. Push the transfer arm until reaching the mechanical stop and tighten the fixing screw again.

9. Move the nanopositioner to position the particle in the center of the cavity mode as described in Sec. 2.3.

10. Turn on the turbo pump to reach high vacuum[5].

To bring vacuum systems to high or especially ultra high vacuum an important step is to bake-out the system. The techniques and principles are well explained in Turner [105, pp. 111ff] and we will summarize here briefly their key conclusions and implications. After the pumps have removed most of the nitrogen molecules from the vacuum chamber the pressure is limited initially by outgassing of water and eventually smaller molecules

---

1 The science chamber stays at a pressure of about 1×10^{-4} mbar without being connected to the pumps.

2 Typically the dominant impurity of nitrogen bottles is water vapor which would be absorbed by the vacuum chamber after venting, which would limit the smallest reachable pressure. Our nitrogen bottles have less than 0.5 ppm H_2O to reduce this effect.

3 We don't close the angle valve vacuum tight as we simply want to reduce the pump speed and avoid turbulent air flow at the particle.

4 This should bring the loading chamber to a pressure of $10^{-3} - 10^{-2}$ mbar.

5 Without baking the vacuum chamber we reach 10^{-5} mbar, with moderate baking we can go down to 10^{-7} mbar.

(H_2, CO, CO_2 and CH_4). Since these molecules outgas and readsorb it takes a long time until the turbo pump removes them. By heating up the vacuum chambers and the components inside we can increase the outgassing rate and accelerate this process. Turner et al. recommend both a pre-bake-out of the components in a vacuum furnace as well as an in situ bake-out of the installed system at temperatures as high as possible, ideally at temperatures significantly higher than 250 °C. In practice, we are able to do a pre-bake-out at 250 °C in a non-vacuum furnace and an in situ bake-out at about 150 °C, limited by cavity components and our nanopositioner. It is particularly challenging to not exceed the maximum temperature of several components while avoiding cold spots that adsorb molecules. We try to achieve this by distributing heating elements evenly around the setup, use aluminum foil for thermal isolation and heat the setup slowly to allow for thermal equilibration. With bake-out times of a few days we can obtain a pressure of 8×10^{-8} mbar which is sufficiently low to not limit our experiments and could potentially be improved significantly by higher bake-out temperatures.

2.2 OPTICAL TRAPPING AND TRANSFER OF LEVITATED PARTICLES

Optical Trapping refers to the spatial confinement of particles by the means of optical forces, first realized by Arthur Ashkin in 1970 in solution [17] and later in high vacuum [18, 106]. Particularly in life sciences strongly focused lasers for particle manipulation, commonly referred to as optical tweezers, became a successful tool, eventually rewarded the Nobel Prize in Physics in 2018 [107, 108]. Optical tweezers can not only be used to confine a particle in space but also to monitor and manipulate its (c.m.) motion as shown by Ashkin in 1977 in the form of a feedback system [109]. The techniques were refined and expanded to trap not only microparticles, but also atoms [110, 111] and nanoparticles [47, 49], paving the way to quantum control of levitated nanoparticles half a century after the pioneering works [70, 72, 73].

The basic concepts of optical levitation are well explained in review papers [99, 112] and PhD theses [113, 114]. To establish an understanding of them we summarize the conclusions of Hebestreit [114] that are relevant for this work. We focus on the trapping of silica (SiO_2) nanoparticles which offer a positive real part of polarizability α. The particle diameter is smaller than the laser wavelength λ and hence well described in a dipolar approximation. To study the dynamics of larger particles of radius $R \approx \lambda$ with volume

$V = 4\pi R^3/3$ one has to apply the full Mie theory formalism [115] or rely on geometric optics in the case of $R \gg \lambda$ [116]. In the dipole approximation the optical force can be decomposed into a gradient force $\boldsymbol{F}_{\text{grad}} \propto V$, pulling the particle towards the point of highest intensity, as well as the scattering force $\boldsymbol{F}_{\text{scat}} \propto V^2$ pushing the particle along the laser's propagation axis. For nanoparticles and for our considerations, both gravity and scattering force are negligible, only slightly displacing the trap center from the laser focus. For small enough particle displacements from the focus of a beam that is approximately Gaussian, the particle motion can be described by a harmonic oscillator. If the particle motion is insufficiently damped by scattering from gas molecules or a feedback mechanism, e.g. linear or parametric feedback [117] or cavity cooling, it experiences the nonlinearities of the confining potential. For the experiments described in this work the particle motion is well described by three uncoupled harmonic oscillators, corresponding to the spatial degrees of freedom. We choose to label the particle oscillation along the laser's polarization axis to be x, along the laser propagation direction to be z and the remaining axis of the Cartesian coordinate system to be y. The equations of motion of our three harmonic oscillators are

$$m\ddot{q}(t) + m\gamma_q\dot{q}(t) + m\Omega_q^2 q(t) = F_q^{(\text{fluct})}(t), \qquad (2.1)$$

with $q \in \{x, y, z\}$, t denoting time, $\dot{q}$ ($\ddot{q}$) the first (second) derivative w.r.t to time, γ_q the damping rate of the motion, Ω_q the oscillation frequency, m the mass of a particle and $F_q^{(\text{fluct})}$ a stochastic drive, given by random kicks from gas molecules, along direction q. The oscillation frequencies scale with optical power P_{tw} and particle density ρ as $\Omega_q = C_q\sqrt{P_{\text{tw}}/\rho}$. The proportionality constant C_q depends on the size of the focal spot. For a Gaussian beam the spot size is characterized by the beam waists or $1/e^2$ radii w_x, w_y along x, y and the Rayleigh range z_R along z. As strong focusing slightly elongates the beam along the polarization axis, the transversal frequencies are nondegenerate [118]. Furthermore, following the calculations of Hebestreit and assuming that the beam cannot be focused more tightly than the diffraction limit we conclude that $\Omega_y > \Omega_x > \Omega_z$. Additionally, optical power and tightness of focus influence stability of particle confinement given by the depth of the optical trap $U_0 \propto VP_{\text{tw}}/w_xw_y$.

Often it is more instructive to investigate the particle motion in the frequency domain instead of the time domain. The spectral power distribution

of the c.m. energy is described by the double-sided power spectral density (PSD) [114]

$$S_{qq}(\Omega) = \frac{A_q}{\pi} \frac{\Omega_q^2 \gamma_q}{(\Omega^2 - \Omega_q^2)^2 + \Omega^2 \gamma_q^2}, \tag{2.2}$$

with $A_q := \int_{-\infty}^{\infty} S_{qq} d\Omega = k_B T / m \Omega_q^2 = \langle q^2(t) \rangle$. Following again the calculations by Hebestreit we approximate S_{qq} for positive frequencies Ω by a Lorentzian line shape,

$$S_{qq}(\Omega) \approx \frac{A_q}{2\pi} \frac{\frac{\gamma_q}{2}}{(\Omega - \Omega_q)^2 + \left(\frac{\gamma_q}{2}\right)^2}, \tag{2.3}$$

Here T is the temperature of the thermal bath which couples to the oscillator and k_B the Boltzmann constant. In our experiments we apply techniques that lower the oscillation amplitude which can be interpreted as coupling the particle to an effective bath. As this effective bath only couples to the c.m. motion and does not affect the bulk or internal temperature [119] of the particle we introduce temperatures $T_{x,y,z}$ which characterize the effective bath coupled to the three oscillators. The terminology "cooling the particle motion" hence refers to lowering the c.m. temperature of the particle. The average phonon occupation $\overline{n}_q$ is then given by the Bose-Einstein distribution [120]

$$\overline{n}_q = \left[\exp\left(\frac{\hbar \Omega_q}{k_B T_q}\right) - 1 \right]^{-1} \approx \frac{k_B T_q}{\hbar \Omega_q}. \tag{2.4}$$

The approximation holds for $k_B T_q \gg \hbar \Omega_q$. Ground-state cooling is achieved for an average phonon number below 1 [70, 72, 73]. As the particle still occupies a thermal state and is not projected into a single vibrational eigenstate we write the probability $p_{x,y,z}^{(0)}$ to occupy the ground-state $n_q = 0$ given $\overline{n}_q$ [121],

$$p_q^{(0)} = 1 - \exp\left(-\frac{\hbar \Omega_q}{k_B T_q}\right) = \frac{1}{1 + \overline{n}_q}. \tag{2.5}$$

2.2.1 Rayleigh and Stokes Scattering

After discussing the concept of phonon numbers we also want to introduce the terminology of Rayleigh and Stokes scattering. Every time a photon impinges on a harmonic oscillator with occupation number n three processes may occur. One is an elastic scattering event where neither the phonon number nor the photon frequency are changed, referred to as Rayleigh scattering. However, the phonon number can increase or decrease which has to be compensated by a photon frequency decrease or increase, respectively. These two inelastic processes are denoted by Stokes and anti-Stokes scattering [122]. The recoil heating rate $\Gamma_q^{(r)}$ quantifies how many phonons are produced per second due to scattering with photons. As each phonon creation implies the emission of a Stokes photon we can use it to estimate the total Stokes scattered power. We write the recoil heating rate for the motion along y according to [51] as

$$\Gamma_y^{(r)} = \frac{1}{5}\frac{P_{dp}}{mc^2}\frac{\omega}{\Omega_y}.$$

(2.6)

Here the total scattered power of the dipole is P_{dp} with incoming light at frequency ω and the speed of light c. The power of Stokes scattered photons is then

$$P_S = \Gamma_y^{(r)}\hbar\omega_S(\overline{n}_y + 1).$$

(2.7)

The Stokes photons are at frequencies $\omega_S = \omega + \Omega_y \approx \omega$ as $\Omega_y \ll \omega$ and we find by employing Eq. (2.4) for large phonon numbers

$$\frac{P_S}{P_{dp}} \approx \frac{1}{5}\frac{k_B T_y}{mc^2}\left(\frac{\omega}{\Omega_y}\right)^2,$$

(2.8)

with T_y the center of mass temperature of the y oscillator we find for a silica particle of radius $R = 70\,\text{nm}$, trapped in an optical tweezer beam at wavelength $\lambda_{tw} = 1550\,\text{nm}$ and oscillating at $\Omega_y = 2\pi \times 150\,\text{kHz}$ in thermal equilibrium with the the surrounding gas at room temperature a ratio of $P_S/P_{dp} \approx 10^{-3}$. As the center of mass motion of the particle is cooled the amount of Stokes photons decreases further. We conclude that the stream of photons scattered by the particle predominantly consists of Rayleigh photons.

2.2.2 *High Numerical Aperture Lenses for Optical Trapping*

In the previous section we discussed that high optical power and tight focusing lead to higher trapping frequencies and deeper traps, which are both desirable. A deeper trap reduces the risk of losing a particle during experiments while systems with higher frequencies suffer less from various noise sources as we will elaborate in Sec. 4.1. In contrast to other levitated optomechanics experiments we have additional requirements to our trapping optics imposed by the setup's geometry. We show in Fig. 2.4 that the trapping optics are mounted on a nanopositioner and have to be placed between two cavity mirrors with a cavity mode living between the trapping and collimation lens. Besides having a high numerical aperture (NA) the trapping lens therefore needs to be sufficiently small to fit between the mirrors, sufficiently light to not overload the nanopositioner and have a sufficiently large working distance to not clip the cavity mode. We could relax the size constraint by placing the lenses outside of the cavity but would need to move the mirrors sufficiently far apart. This would increase the cavity mode volume, which reduces the coupling rate between particle motion and cavity mode, which is undesirable. Another option is to manufacture sufficiently small mirrors to not clip the optical tweezer. During the work of this thesis we implemented two generations of trapping lenses which are described in this section. The working principle and implementation of the two generations are very similar and are shown in Fig. 2.4. They only differ in slight modifications to the holder assembly to fit the exact lens design and focal length of the collimator to properly fill the clear aperture of the lens. In both cases we feed about $P_{\text{tw}} = 500\,\text{mW}$ of optical power at a wavelength of $\lambda = 1550\,\text{nm}$ (*NKT Koheras Adjustik E15*) through a polarization maintaining in-vacuum fiber to a collimator that overfills the trapping lens ($1/e^2$ intensity diameter of beam is about clear aperture of lens). To not heat up the cavity mirrors with the diverging tweezer we immediately collimate the beam again with a second collimation lens on the opposite side of the optical trap. This is achieved with a three part holder assembly where the outer holder has slots to insert the lenses and an external thread (M3 $\times$ 0.25) that fits into the center piece's internal thread. The pitch of the thread is small enough to in situ adjust the lens separation for collimating a laser passing through the assembly and eventually gluing the assembly in place. In Tab. 2.1 we list key parameters of the trapping lenses used. The second generation lens outperforms the first generation according to *Zemax* simulations as

well as according to our experiments despite having a lower nominal NA. This can be explained by the fact that the design wavelength of the first generation did not match the experimental wavelength and that we were not able to properly overfill the clear aperture without clipping too much light in the tweezer assembly. Another disadvantage of the generation 1 lens is its polymer replication layer which can be dissolved by IPA/ethanol during cleaning or particle trapping [6]. The main advantage of the second generation is the larger working distance which reduces clipping of the cavity mode.

	Generation 1	Generation 2
Manufacturer	A.W.I.	Lightpath
Part Number	E15456-25	0355617
Material	polymer on glass	D-ZLAF52LA(m)
Clear Aperture (mm)	1.3	0.79
Lens Diameter (mm)	1.63	1.4
Design Wavelength (nm)	1530	1550
Working Distance (μm)	141	190
Nominal NA	0.83	0.75
Ideal Input Beam Waist (μm)	650	395
Relative Trap Frequency	1	1.19
Collimator Used	S+K 60FC-4-M5-08	S+K 60FC-4-A4.5-03
Input Beam Waist (μm)	489	440
Measured $\Omega_{x,y,z}$ (kHz/2π)	$[120, 140, 40]$	$[158, 193, 60]$

TABLE 2.1: Comparison of two generations of trapping lenses. The relative trap frequency is relative to generation 1. The value is obtained from *Zemax* simulations assuming ideal overfilling of the clear aperture. The measured trap frequencies $\Omega_{x,y,z}$ correspond to an optical power of about $P_{tw} = 500(50)$ mW in the focus. To avoid clipping too much power in the tweezer assembly of generation 1 we cannot set the input waist to the ideal value, thereby lowering the trapping frequencies.

---

6 particles are dispersed in ethanol.

2.2.3 *Optical Trapping with a Nebulizer*

To trap nanoparticles we rely on the method developed and described by Gieseler [113]. We equip a commercially available nebulizer (*Omron NE-U22-W*) with a custom aluminum nozzle that confines the otherwise wide cloud of aerosol droplets to a narrow stream. When using a plastic nozzle instead we observe the aerosol condensing on the sidewalls and eventually clogging the nozzle. Our theory is that static charges on the plastic increase the pull of aerosol particles towards the sidewalls compared to the aluminum nozzle. Furthermore, condensed solvent can dissolve plastic particles and introduce them into the aerosol stream. We use commercially available SiO_2 beads in aqueous dispersion of concentration $50\,mg/ml$ by *microparticles GmbH*. As shown in Fig. 2.3 we monitor whether a particle is trapped by collecting the light that is scattered from a potentially trapped particle back into the in-vacuum fiber, through a Faraday circulator and onto the backreflection photodiode. In practice, we not only collect light scattered from the particle but also from fiber facets, leading to a homodyne measurement with a thermally drifting relative phase. This arrangement is not feasible for quantitative measurements but gives us an idea whether we have trapped a single particle or a cluster. To introduce the particles into the optical tweezer we follow these steps:

1. Mix $10\,\mu l$ of initial solution with $5\,ml$ of ethanol[7], leading to a mean value of about one nanoparticle per nebulizer droplet.

2. Sonicate the solution for at least $5\,min$ in a bath sonicator to break up particle clusters[8].

3. Fill the solution into the nebulizer and attach the aluminum nozzle.

4. Make sure that a stream of aerosol particles visibly leaves the nozzle.

5. Aim the aerosol stream at the optical tweezer, varying the distance to the focus while monitoring the backreflection photodiode.

6. Based on photodiode signal estimate if the trapped object is a single particle or a cluster. The intensity of scattered light by a dipole and hence the detector signal scales with $P_{dp} \propto V^2$ [114, 123].

---

7 Omron specifies a slightly better chemical stability for ethanol compared to IPA.
8 We observed switching to a high power sonicator can break clusters even more efficiently leading to a higher success rate of trapping single particles.
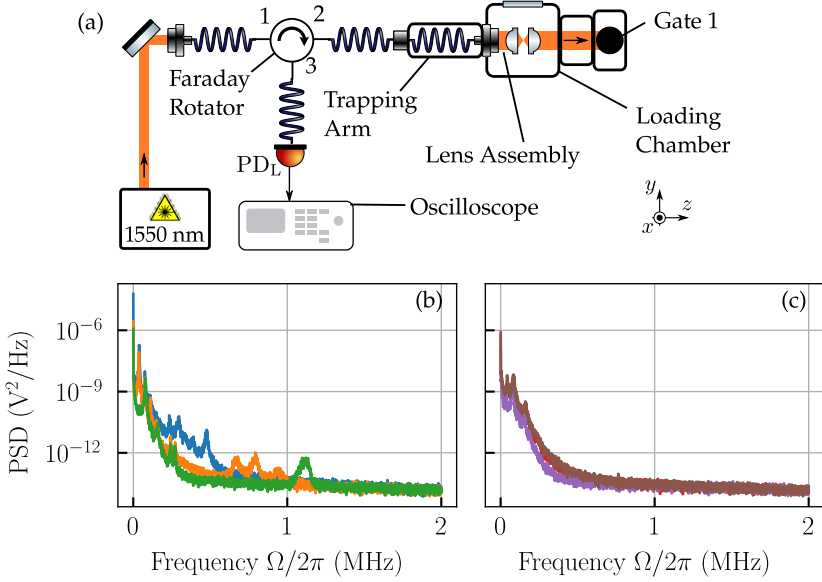
FIGURE 2.3: *Trapping setup with photodiode output.*(a) The schematic shows the optical components necessary for particle trapping. We couple a 1550 nm laser into port 1 of a fiber based Faraday circulator (*AC Photonics HPMOC315P21511S1*). The laser is coupled via port 2 to the in-vacuum fiber inside the trapping arm, passes through the lens assembly with an attached Faraday isolator (not shown) to avoid backreflections into the trap before being dumped on the closed gate 1. Light scattered backwards from the particle is collected by the trapping lens, enters the Faraday circulator via port 2 and couples out of port 3 alongside spurious reflection from fiber facets, resulting in a homodyne measurement by detector PD_L, with a thermally drifting relative phase. We plot the power spectral densities of the detected signal of six different trapping attempts in (b, c) at pressures of $1 - 10$ mbar. The power at the input is chosen such that we have $P_{tw} = 500(10)$ mW in the focus. As the free space detector is blocked by gate 1 and PD_L has no information about the transversal motion of the particle due to the fiber coupling we only expect to see peaks corresponding to the motion along z ($\Omega_z/2\pi = 40(2)$ kHz) and higher harmonics. In (b) we show single-sided PSDs of potential particle clusters. Besides peaks corresponding to the z-motion we observe broad peaks from 200 kHz onward. We attribute them to libration modes originating from the asymmetrical shape of clusters. In (c) we show single-sided PSDs of potential single particles. The DC signal is lower compared to (b) as the scattered power scales with the square of the particle volume and we do not observe higher frequency peaks. The small differences between the three curves stem from the drifting phase of the homodyne detection and the measurements not being performed at exactly the same pressure.

7. Evacuate the loading chamber to less than 10 mbar while monitoring the Fourier transform (FFT) of the photodiode signal. As the phase of our homodyne measurement drifts we see even and odd harmonics of the particle's z motion [114]. If there are additional peaks in the range up to 3 MHz, fluctuating in shape or center frequency we assume that we have trapped a cluster [9] [47, 82].

8. In case of a cluster, block the laser, vent the chamber and start again. Otherwise continue evacuating and proceed to initiate the transfer.

2.3   A FABRY-PÉROT CAVITY FOR PARTICLE DETECTION AND MANIPULATION

After introducing the concept of particle trapping in optical tweezers we focus on the second key building block of the experiment, the Fabry-Pérot cavity. It was first introduced by Charles Fabry and Alfred Pérot in 1899 as two partially transmitting planar mirrors facing each other [124], long before the invention of the laser in 1960 [125]. They have been used as narrowband optical filters, by injecting a light field into the interferometer under an angle and analyzing the measured interference pattern in reflection or transmission. Decades of engineering were necessary to obtain highly reflective curved mirrors with low absorption to create the mirrors we use in our experiments. The curvature is necessary to confine a cavity mode while a high reflectivity allows for a large amount of optical power to build up. Ideally the cavity loss is limited by mirror transmission and not absorption. This gives access to information about the field inside by probing the signal leaking out through the mirrors. The first Fabry-Pérot type resonator was coated with a thin metal dielectric film in 1939 by Geffcken at *Schott und Genossen* before the reactive gas deposition processes invented by Auwärter in 1952 practically realized environmentally stable complex thin film interference systems [126]. In the following section we summarize the cavity fundamentals necessary to characterize our optical cavity and explain the experiments thereafter.

---

[9] We are not able to measure the transversal particle motion before transfer to the science chamber. We experienced this procedure to be a good indicator of a single particle but rely on a proper size calibration at a later stage.
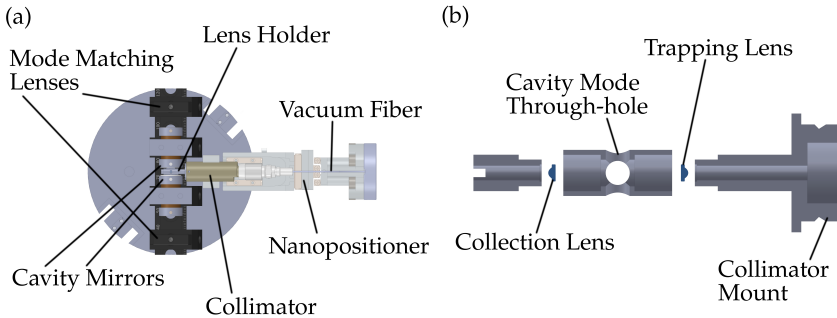
FIGURE 2.4: *High NA lens assembly for optical trapping of particles.* (a) The lens assembly positioned between the cavity mirrors is shown. We obtain this configuration after pushing in the transfer arm as described in Fig. 2.2. The side and top plates of the cavity housing are removed for demonstrative purpose. The laser used to trap particles is fed into the vacuum chamber via the polarization maintaining in-vacuum fiber, gets collimated and passes through a custom lens assembly. With the nanopositioner we place the lens assembly such that a trapped particle is in the transverse center of the cavity mode and can be moved along the cavity standing wave. (b) Exploded view of the custom lens assembly cross section. To be able to fine tune the distance between collection and trapping lens we designed a three component lens holder. The collimator mount can be fixed with screws to a *Schäfter+Kirchhoff* collimator. The trapping/collection lens has a diameter of 1.4 mm and an NA = 0.75. Both lenses are placed in slots and glued in place in their corresponding mounts. The center adapter has internal threads into which we screw the outer mounts. Thereby, we are able to keep the lenses on axis and tune the distance to properly focus and collimate the incoming beam, while in situ gluing the adapters in place. To prevent backreflections from reentering the assembly from the opposite side we glue a Faraday isolator (*Isowave I-15-LM-TD-1.4-4*) at the opposite side of the collection lens holder (not shown).

2.3.1 *Cavity Fundamentals*

We introduce the classical input-output formalism, see Loudon [127], to describe a plane-parallel cavity after choosing a convention regarding the phases picked up by reflected and transmitted light at a partially reflective surface. For an incoming light field E we define the transmitted and reflected fields to be given by $E_t = it_s E$ and $E_r = r_s E$ respectively, for real valued reflection and transmission coefficients r_s, t_s. Furthermore, we define the absorption coefficient a as well as mirror reflection $\mathcal{R} = r_s^2$, transmission $\mathcal{T} = t_s^2$ and absorption $\mathcal{A} = a_s^2$, with $\mathcal{R} + \mathcal{T} + \mathcal{A} = 1$, as a consequence of energy conservation. We consider the situation depicted in Fig. 2.5 of a light field E_{in} at frequency ω impinging on the left mirror and formulate steady-state relations for the circulating fields as well as the fields reflected from the left mirror (E_{ref}) and transmitted through the right mirror (E_{tr}),

$$
\begin{aligned}
E_1 &= it_A E_{in} + r_A E_2 \\
E_2 &= r_B E_1 e^{i2L\omega/c} \\
E_{tr} &= it_B E_1 e^{iL\omega/c} \\
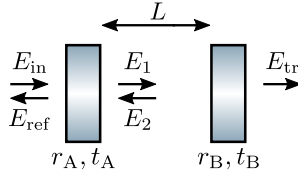E_{ref} &= r_A E_{in} + it_A E_2.
\end{aligned}
\tag{2.9}
$$

FIGURE 2.5: *Input-output formalism for plane-parallel cavity.* We consider two plane mirrors of reflection and transmission coefficients r_A, t_A, r_B, t_B. The separation of the mirrors is L and a light field E_{in} of wavelength λ is fed through the left mirror. All denoted electric fields are steady-state solutions of the cavity system. The field E_1 (E_2) refers to the fields propagating to the right (left) just after (before) the left mirror. The reflected (transmitted) field is denoted by E_{ref} (E_{tr}).

We solve the system of linear equations and derive the cavity transfer functions,

$$
\begin{aligned}
F_{tr} &:= \frac{E_{tr}}{E_{in}} = \frac{\mathcal{T}_{AB} e^{iL\omega/c}}{\mathcal{R}_{AB} e^{i2L\omega/c} - 1} \\
F_{ref} &:= \frac{E_{ref}}{E_{in}} = \frac{\sqrt{\mathcal{R}_B}(1 - \mathcal{A}_A)e^{i2L\omega/c} - \sqrt{\mathcal{R}_A}}{\mathcal{R}_{AB} e^{i2L\omega/c} - 1},
\end{aligned}
\tag{2.10}
$$

with $\mathcal{T}_{\mathrm{AB}} = t_{\mathrm{A}}t_{\mathrm{B}}$, $\mathcal{R}_{\mathrm{AB}} = r_{\mathrm{A}}r_{\mathrm{B}}$, $\mathcal{T}_i = t_i^2$, $\mathcal{R}_i = r_i^2$ and $\mathcal{A}_i = a_i^2$ for $i \in \{\mathrm{A}, \mathrm{B}\}$. From Eq. (2.10) we conclude that the light transmitted through the cavity does not contain any directional system information[10] as the transfer function is symmetric in subscripts A, B. The reflected field on the other hand contains directional information in the form of the reflectivity of mirror A and B, as well as absorption of mirror A, which will be important when discussing the Pound-Drever-Hall locking technique in Sec. 2.3.2. We can calculate the transmitted intensity normalized to the input intensity by taking the absolute value squared of the cavity transfer functions,

$$
\begin{aligned}
T_{\mathrm{tr}} := |F_{\mathrm{tr}}|^2 &= \frac{\mathcal{T}_{\mathrm{AB}}^2}{(1 - \mathcal{R}_{\mathrm{AB}})^2} \frac{1}{1 + \left(\frac{2\sqrt{\mathcal{R}_{\mathrm{AB}}}}{1 - \mathcal{R}_{\mathrm{AB}}}\right)^2 \sin^2\left(\frac{\omega L}{c}\right)} \\
&\approx \frac{\mathcal{T}_{\mathrm{AB}}^2}{(1 - \mathcal{R}_{\mathrm{AB}})^2} \frac{(\kappa/2)^2}{(\kappa/2)^2 + \Delta^2}.
\end{aligned} \tag{2.11}
$$

To obtain the approximation we have chosen $\omega = q\omega_{\mathrm{fsr}} + \Delta$ with $\omega_{\mathrm{fsr}} = \pi c/L$, the free spectral range and $q \in \mathbb{N}$. Therefore, Δ denotes the detuning from the resonance frequency and we can linearize the sine to obtain the Lorentzian lineshape, introducing κ as the full width half maximum (FWHM) or cavity linewidth,

$$
\kappa = \frac{1 - \mathcal{R}_{\mathrm{AB}}}{\sqrt{\mathcal{R}_{\mathrm{AB}}}} \frac{c}{L}. \tag{2.12}
$$

We furthermore define the finesse $\mathcal{F}$ of the cavity as the ratio of the free spectral range over the FWHM of a resonance fringe,

$$
\mathcal{F} := \omega_{\mathrm{fsr}}/\kappa = \frac{\pi\sqrt{\mathcal{R}_{\mathrm{AB}}}}{1 - \mathcal{R}_{\mathrm{AB}}}. \tag{2.13}
$$

As the expression for the reflected field is more involved we show the normalized reflected intensity and phase of the transfer function in Fig. 2.6. In Fig. 2.6(a), we tune the cavity length with cavity resonance at $\Delta L = 0$. Off resonance all of the light is reflected whereas on resonance the reflection is minimal and light is transmitted through the cavity. When tuning the cavity length over a resonance in Fig. 2.6(b), the reflected light undergoes a phase shift which we will utilize to stabilize the cavity length at $\Delta L = 0$ as described in Sec. 2.3.2.

---

10 The transmission transfer function is invariant under exchanging the positions of mirror A and B.
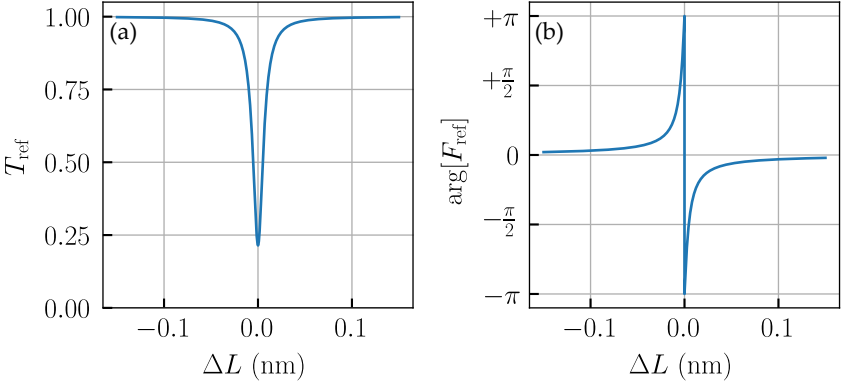
FIGURE 2.6: *Phase and squared absolute value ($\propto$ intensity) of reflected cavity field.*
For a laser of wavelength $\lambda = 1550$ nm we set the cavity length $L \approx 8$ mm. The
laser is resonant for $\Delta L = 0$. The chosen cavity parameters are $\mathcal{T}_A, \mathcal{T}_B, \mathcal{R}_A, \mathcal{R}_B =$
$[79\,\text{ppm}, 20\,\text{ppm}, 1 - 83\,\text{ppm}, 1 - 25\,\text{ppm}]$. (a) Normalized reflected intensity. On
resonance the laser couples into the cavity and the reflected intensity is minimal.
(b) Phase imprinted on the reflected field. On resonance the phase is 0, but for
positive (negative) ΔL the picked up phase is positive (negative).

In our experiments, described in the following chapters, we position a
particle inside the optical cavity to couple mechanical and optical modes.
At a later stage in Sec. 3.5.1 we will discuss the optical forces on the
particle arising from the cavity field in the context of frequency and phase
fluctuations of the input laser. To facilitate the discussion we analyze here
already the impact of input laser frequency fluctuations on the cavity
intensity profile. To do so, we solve Eq. (2.9) for E_1 and E_2 and look at the
interference pattern at position y relative to the input mirror. We find the
normalized intensity profile $T_c := |F_c|^2$ with

$$
\begin{aligned}
F_c &= (E_1 e^{i\omega y/c} + E_2 e^{-i\omega y/c})/E_{\text{in}} \\
&= \frac{it_A \left(r_B e^{\frac{2iL\Delta}{c}} + e^{\frac{2iy\omega}{c}} \right) e^{\frac{-iy\omega}{c}}}{1 - r_A r_B e^{\frac{2iL\Delta}{c}}}.
\end{aligned}
\tag{2.14}
$$

In Eq. (2.14) we have defined $\omega = q\omega_{\text{fsr}} + \Delta$ for $q \in \mathbb{N}$ to simplify the
expression. We continue to derive the normalized intensity profile,

$$T_c = \frac{\mathcal{T}_A \left[\mathcal{R}_B + 1 + 2\sqrt{\mathcal{R}_B} \left(\sin \frac{2L\Delta}{c} \sin \frac{2y\omega}{c} + \cos \frac{2L\Delta}{c} \cos \frac{2y\omega}{c} \right) \right]}{\mathcal{R}_{AB}^2 - 2\mathcal{R}_{AB} \cos \frac{2L\Delta}{c} + 1} \tag{2.15}$$

We first consider the case of two resonances separated by a free spectral range i.e. $\Delta = 0$ or $\Delta = \omega_{fsr}$.

$$T_c(\Delta = \omega_{fsr}) = \frac{\mathcal{T}_A \left\{ \mathcal{R}_B + 1 + 2\sqrt{\mathcal{R}_B} \cos[2\pi\widetilde{y}(q+1)] \right\}}{(\mathcal{R}_{AB} - 1)^2}$$

$$T_c(\Delta = 0) = \frac{\mathcal{T}_A \left\{ \mathcal{R}_B + 1 + 2\sqrt{\mathcal{R}_B} \cos[2\pi\widetilde{y}q] \right\}}{(\mathcal{R}_{AB} - 1)^2}$$

We defined the normalized cavity position $\widetilde{y} = y/L$ with $\widetilde{y} = 0$ (1) being on the input (output) mirror. We observe that for any q the two resonance are in phase on the mirrors and out of phase at $\widetilde{y} = 1/2$. Similarly, for resonances separated by $\Delta = 2\omega_{fsr}$ we can derive that the the modes are in phase on the mirrors and in the center of the cavity as shown in Fig. 2.7(a–c). The contrast between a maximum and minimum of the intensity on resonance is given by,

$$\frac{T_c^{(max)}}{T_c^{(min)}} = \frac{(\sqrt{\mathcal{R}_B} + 1)^2}{(\sqrt{\mathcal{R}_B} - 1)^2} \tag{2.16}$$

Now we want to consider the case of detunings close to a resonance $\Delta \ll \omega_{fsr}$. When detuning the input laser from a resonance we expect less light to couple to the cavity. Furthermore, as the detuned frequency does not match the resonance condition of the cavity anymore, we expect the standing wave profile to change as well. We continue our calculation to find the position of intensity extrema, as a function of input laser frequency. We expand Eq. (2.15),

$$T_c \approx \frac{\mathcal{T}_A \left[\mathcal{R}_B + 1 + 2\sqrt{\mathcal{R}_B + \mathcal{R}_B \left(\frac{2\pi\Delta}{\omega_{fsr}} \right)^2} \sin \left(\frac{2y\omega}{c} + \Phi \right) \right]}{(\mathcal{R}_{AB} - 1)^2} \tag{2.17}$$

and use Cor. A.2.2.1 to combine sine and cosine terms to find $\Phi = \pi/2$ for $\Delta = 0$ and $\Phi = \arctan(\omega_{fsr}/2\pi\Delta)$ otherwise. To find the positions of
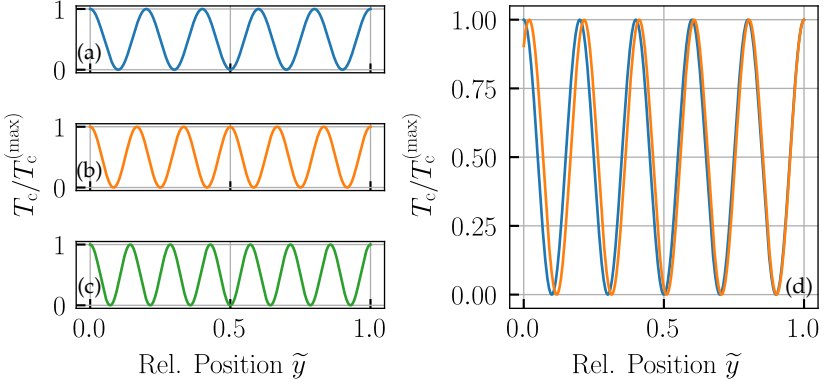
FIGURE 2.7: *Cavity intensity profile.* We show cavity intensity standing wave profiles for mirror parameters as in Fig. 2.6 and a cavity length of $L = 2.5\lambda$ to be able to plot the full profile. For a laser frequency detuned from the cavity resonance the coupling and thereby the intensity are reduced. We rescale the intensity profile to be able to compare the positions of antinodes and nodes. In the left column we plot the intensity profile for $\Delta = \{0, \omega_{\mathrm{fsr}}, 2\omega_{\mathrm{fsr}}\}$ in (a), (b) and (c) respectively. Only for (a) and (c) the intensity is minimal in the center ($\widetilde{y} = 1/2$) while it is maximal for (b). (d) We plot the intensity profiles in blue (orange) for $\Delta = 0$ ($\Delta = \omega_{\mathrm{fsr}}/10$). Increasing the detuning compresses and shifts the profile.

the intensity extrema we investigate $\theta := 2y\omega/c + \Phi$. In particular we want to find how much these positions fluctuate, as a function of laser frequency ω by differentiating θ,

$$d\theta = 2\pi \frac{d\omega}{\omega_{\mathrm{fsr}}}(\widetilde{y} - 1). \tag{2.18}$$

We linearize Φ around ∞ since $\omega_{\mathrm{fsr}} \gg \Delta$ and observe that frequency fluctuations not only affect the amount of power entering the cavity, but also the position of nodes and antinodes of the cavity field. When coupling light in through mirror A the extrema are maximally shifted at the input mirror ($\widetilde{y} = 0$) and minimally at the output mirror B ($\widetilde{y} = 1$), as shown in Fig. 2.7(d). We want to point out that this stems from our choice that there is no phase shift imprinted on the reflected field, but solely on the transmitted field. This choice is mathematically valid and conserves energy, but not necessarily physically accurately describing the reflection process.

We conclude therefore that the cavity intensity profile jitters for a frequency or phase fluctuation of the input beam. The strength of this effect scales as $d\theta \propto \frac{d\omega}{\omega_{\text{fsr}}}$ and is not uniform along the cavity axis. To understand where the effect is minimal on the other hand we require detailed knowledge about the dielectric mirror coating to accurately determine the phase which is imprinted on the reflected light [128, 129].

2.3.2 *Pound-Drever-Hall Lock*

In the laboratory we would like to be able to set and lock the cavity length L, such that the cavity is resonant with a certain frequency ω. From Eq. (2.11) it becomes evident that the transmission signal (and similarly the reflection signal) is not suitable to derive a lock signal since $T_{\text{tr}} = T_{\text{tr}}(\omega^2)$, unless we sacrifice transmitted power and lock to a point away from the maximum of the Lorentzian (side-of-fringe lock [130]). The main drawback of the side-of-fringe lock is its small capture range of $\kappa/2$[11] potentially kicking the particle out of the optical trap while the cavity falls out of lock. Additionally, the side-of-fringe lock is sensitive to power fluctuations which might arise from trapping light scattering via the particle onto the photodetector PD_{PDH}. Hence we prefer to use the Pound-Drever-Hall (PDH) technique [131]. A thorough description of the technique can be found in [132], but we would like to mention key findings and implications to our setup. The main idea behind the PDH lock is depicted in Fig. 2.6. As shown in (b) the phase picked up by the reflected field depends on cavity length, vanishing on resonance $\Delta L = 0$ and having opposite signs on both sides of resonance, making it a suitable feedback parameter. To interferometrically measure the phase we modulate sidebands onto a laser which we denote by lock laser. An electro-optic modulator (EOM) creates sidebands spaced at Ω_{s} from the lock laser carrier, creating an input field

$$
\begin{aligned}
E_{\text{in}} &= E_0 e^{i(\omega t + \beta \sin[\Omega_{\text{s}} t])} \\
&\approx E_0 \left[J_0(\beta) e^{i\omega t} + J_1(\beta) e^{i(\omega + \Omega_{\text{s}})t} + J_1(\beta) e^{i(\omega - \Omega_{\text{s}})t} \right].
\end{aligned} \quad (2.19)
$$

We use the Bessel functions of the first kind and neglect higher order sidebands since $\beta \ll 1$ [132]. For a laser of input power $P_0 \propto |E_0|^2$ we modulate sidebands of total power $P_{\text{s}} = J_1^2(\beta) P_0$ with a carrier of power $P_{\text{c}} = J_0^2(\beta) P_0$. The goal is to extract the phase picked up by the off-resonant sidebands,

---

11 The slope of T_{tr} has opposite signs on the two sides of the fringe.

by interfering them on a photodetector in reflection and converting them into an error signal $\mathcal{E}$ with electronic filters and mixers, as show in Fig. 2.8. Using the cavity transfer function we write down the reflected power and neglect terms at $2\Omega_s$, stemming from the interference of the sidebands with each other,

$$
\begin{aligned}
P_{\text{ref}} = {}& P_c T_{\text{ref}}(\omega) + P_s [T_{\text{ref}}(\omega + \Omega_s) + T_{\text{ref}}(\omega - \Omega_s)] \\
& + 2\sqrt{P_c P_s} \{ \text{Re}[F_{\text{ref}}(\omega)F_{\text{ref}}^*(\omega + \Omega_s) - F_{\text{ref}}^*(\omega)F_{\text{ref}}(\omega - \Omega_s)] \cos(\Omega_s t) \\
& \qquad + \text{Im}[F_{\text{ref}}(\omega)F_{\text{ref}}^*(\omega + \Omega_s) - F_{\text{ref}}^*(\omega)F_{\text{ref}}(\omega - \Omega_s)] \sin(\Omega_s t) \} \\
& + \text{higher order terms.} \qquad\qquad\qquad\qquad\qquad\qquad\qquad\qquad (2.20)
\end{aligned}
$$

The first line of Eq. (2.20) is blocked by an electronic high pass filter and after demodulating the output at Ω_s with the correctly adjusted phase, we obtain the error signal,

$$
\mathcal{E} = 2\nu\sqrt{P_c P_s}\, \text{Im}[F_{\text{ref}}(\omega)F_{\text{ref}}^*(\omega + \Omega_s) - F_{\text{ref}}^*(\omega)F_{\text{ref}}(\omega - \Omega_s)]. \qquad (2.21)
$$

Here ν is a constant that includes detector responsivity, gain and efficiencies of the electronic transmission line. When ω is close to resonance and the modulation frequency is chosen such that the sidebands get fully reflected $\Omega_s \gg \kappa$, we can simplify Eq. (2.21) since $F_{\text{ref}}(\omega \pm \Omega_s) = F_{\text{ref}}^*(\omega \pm \Omega_s) = \sqrt{\mathcal{R}_A} \approx 1$. As $F_{\text{ref}}(\omega) - F_{\text{ref}}^*(\omega) = 2i\,\text{Im}[F_{\text{ref}}(\omega)]$ the cosine coefficient vanishes, motivating our previous decision to pick the demodulation phase and giving us a simple expression for the error signal close to resonance,

$$
\mathcal{E}_{\text{lin}} = -8\nu\sqrt{P_c P_s} \frac{\sqrt{\mathcal{R}_B}\mathcal{T}_A}{(\mathcal{R}_{AB} - 1)^2} \frac{\Delta L \omega}{c}, \qquad (2.22)
$$

with ΔL denoting small displacements from resonance. We observe that indeed the error signal close to resonance depends both linearly on cavity length and laser frequency ω, implying that either the cavity length can be locked to the laser frequency or the other way around. Making the slope of Eq. (2.22) steeper by increasing laser power or optimizing gain parameters of the electronic circuit typically also increases noise. Since the mirror parameters are given by the type of experiment, only two optimization steps remain. Firstly, we set the sideband modulation strength β such that $P_s/P_c = 1/2$. Secondly, in the case of an asymmetric cavity (unequal reflectivities of the two mirrors) it is beneficial to choose mirror A (lock mirror)
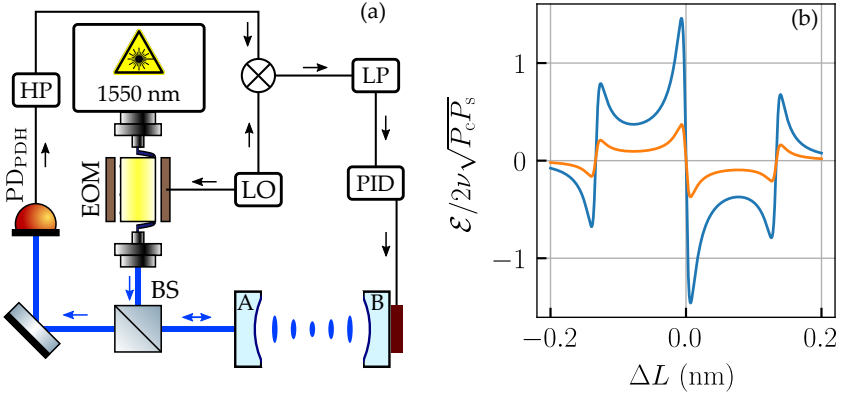
FIGURE 2.8: *Pound-Drever-Hall lock scheme with error signal.* (a) We use a fiber-based EOM, driven by a local oscillator, to create sidebands as described in Eq. (2.19). We send the beam to a beam splitter that reflects 10% towards mirror A and transmits 90% of the cavity reflection towards a photodiode. The detector signal is band-pass filtered, mixed with the local oscillator, low-pass filtered and fed to an analog PID controller. The PID controller adjusts the cavity length by driving a ring piezo behind the mirror. (b) We plot the calculated error signal as sent into the PID controller. The orange (blue) line refers to the case of coupling through the mirror of high (low) reflection.

of higher transmission and mirror B of higher reflectivity. Unfortunately, in our experiments we require to place our detection optics behind the mirror with higher transmission and have to settle with locking through the highly reflective mirror. In Fig. 2.8(b) we observe how locking through the lower finesse mirror improves the PDH error signal.

2.3.3 *Locking to the Transverse* 10 *Mode*

In our coherent scattering setup as described in Sec. 3.2 we populate an optical cavity with a lock laser through one of the mirrors and also coherently scatter light via a levitated particle from the side into the cavity. Initially we tried to minimize interference of these two fields by cross polarizing them, but eventually decided to separate them spectrally. We achieve this by coupling the lock laser to the first higher order transverse cavity mode (TEM_{10}) as described in this section.

To understand the transverse mode structure of an optical cavity one has to move away from the model of plane-parallel mirrors. In theory, we can calculate the transverse modes for any type of mirror shape and cavity length [125, 133]. If a light field maintains its transverse profile upon a cavity round trip we refer to it as a cavity mode, adopting the definition of Siegmann [125, pp. 559ff]. In practice, we only obtain modes that survive a significant amount of round-trips and qualify as high-finesse by using spherical mirrors and adhering to stability criteria regarding the cavity length. We refer to these modes as transverse modes (TEM_{nm}) where the indices n, m denote the number of dark fringes in the horizontal and vertical direction, respectively. These modes are well described by Hermite-Gaussian functions. To fulfill the longitudinal resonance condition the round-trip phase pick up has to be an integer multiple of 2π. Since the Gouy phase is different for each TEM_{nm}, also the resonance frequency differs [125],

$$\omega_{qnm} = \left[q + (n + m + 1) \frac{\arccos(\pm\sqrt{g_A g_B})}{\pi} \right] \times \frac{\pi c}{L}, \qquad (2.23)$$

with $g_i = 1 - L/\text{ROC}_i$ for $i \in \{A, B\}$ and ROC_A (ROC_B) the radius of curvature of mirror A (B). The integers q, n, m label the longitudinal and transversal modes. The $+$ sign applies for $g_A, g_B > 0$ and the $-$ sign for $g_A, g_B < 0$. In our experiment we lock the cavity length L to the frequency of the lock laser. To scatter light from a laser at a different frequency to the same cavity we need to tune the frequency such that Eq. (2.23) is fulfilled for a combination of q, n, m. There are two strategies to obtain this. We can either couple both lasers to two TEM_{00} modes, separated by a free spectral range or to two different transverse modes. For both of them one has to achieve a very stable frequency relation of the two lasers, which we obtain by picking the lock laser off from the trap laser. For our cavity geometry the free spectral range is $\omega_{\text{fsr}}/2\pi \approx 21\,\text{GHz}$ which is impossible to bridge with an acousto-optic modulator (AOM) and requires costly equipment such as a high frequency RF source and an EOM. By coupling the lock laser to the TEM_{10} we can reduce the frequency and have zero intensity in the center of the lock mode, where the particle is placed. The disadvantage is a decrease of the signal-to-noise ratio of the PDH error signal due to a reduced coupling efficiency from a typical free space TEM_{00} laser mode to the cavity TEM_{10} mode. In practice, our PDH loop is limited by electronic noise of the feedback system and not by the optical coupling efficiency.

In general an EOM does not simply shift a laser frequency, but modulates sidebands as show in Eq. (2.19). In contrast to Sec. 2.3.2 we modulate the

EOM much stronger to suppress the carrier frequency almost entirely. As a result most of the power is converted to first and higher order sidebands. The frequency spacing between TEM$_{00}$ and higher order modes can be calculated using Eq. (2.23),

$$
\begin{aligned}
\omega_{q10} - \omega_{q00} &= \frac{\arccos(\pm\sqrt{g_A g_B})}{\pi}\omega_{\text{fsr}} \\
\omega_{q20} - \omega_{q00} &= 2\frac{\arccos(\pm\sqrt{g_A g_B})}{\pi}\omega_{\text{fsr}}.
\end{aligned}
\tag{2.24}
$$

We first consider $\Omega_{\text{EOM1}} = \omega_{q10} - \omega_{q00}$, to make the first sideband resonant with TEM$_{10}$. With Eq. (2.24) we observe, that simultaneously the carrier becomes resonant with TEM$_{00}$ and furthermore also the second sideband with TEM$_{20}$ (and similarly TEM$_{11}$). We noticed in experiments, that especially the resonant carrier is able to heat up the particle, while the resonant second order sideband disturbed the PDH locking scheme. Instead of selecting a sideband with a filtering cavity [104] we decide to combine the EOM with an AOM as shown in Fig. 2.9. The AOM scatters light into different diffraction orders that are spatially separated, allowing us to pick out the first order and shifting the beam by Ω_{AOM} [134]. Since $\Omega_{\text{AOM}} \ll \omega_{q10} - \omega_{q00}$ we still need to use an EOM and choose the modulation frequencies such that $\Omega_{\text{AOM}} + \Omega_{\text{EOM1}} = \omega_{q10} - \omega_{q00}$. With this trick we can bridge the large frequency gap and make only one sideband resonant with the cavity.
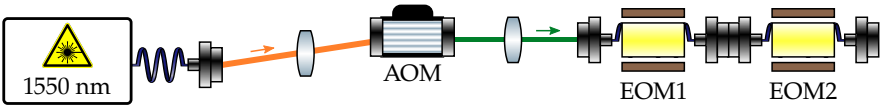

FIGURE 2.9: *Frequency shifting for* TEM$_{10}$ *lock.* A building block to derive the lock laser from the trap laser is shown. The component EOM2 is the EOM shown in Fig. 2.8(a) to derive the PDH sidebands. The other components were not shown previously to focus on the PDH scheme exclusively. The purpose of this setup is to shift the lock laser by Ω_{AOM} and then modulate sidebands at Ω_{EOM1}. The first order higher frequency sideband picks up a total frequency shift of $\Omega_{\text{AOM}} + \Omega_{\text{EOM1}}$.

2.3.4 *Designing an Optical Cavity*

In the previous sections we established that cavity mirrors have to be spherical and require placement at a precise distance. However, we did not elaborate how specific radii of curvature, cavity lengths and mirror coatings need to be chosen to suit our experiments. As we study and manipulate the particle dynamics coupled to the optical cavity the important figures of merit are the coupling strength between particle and cavity, as well as the response or readout time of the optical cavity. In Sec. 2.3.1 we studied only the steady-state properties of an optical cavity, but we can relate the cavity linewidth to the cavity storage time[12] $\tau_s = \mathcal{F}/\omega_{fsr} = 1/\kappa$ [135]. In Chapter 3 we will explain the theory behind cavity cooling in combination with coherent scattering in detail, before discussing the influence of cavity parameters on the lowest obtainable phonon numbers in Sec. 4.1. We will find out that a large optomechanical coupling rate g and a cavity linewidth similar to the mechanical frequency of the particle c.m. motion are desirable. To motivate our cavity design we want to relate these parameters to mirror properties and geometric characteristics of the setup. The optomechanical coupling rate depends on cavity mode volume $g \propto 1/\sqrt{V_c}$ (see Eq. (4.2)). The cavity mode volume is in turn given by $V_c = \pi w_c^2 L/4$, with cavity mode waist w_c and cavity length L. We can summarize how our figures of merit relate to design parameters by considering

$$g \propto \frac{2}{w_c\sqrt{\pi L}}$$
$$\kappa = \frac{1 - \mathcal{R}_{AB}}{\sqrt{\mathcal{R}_{AB}}} \frac{c}{L}. \tag{2.25}$$

We first focus on how to increase g by investigating Eq. (2.25) and following the calculations of Siegmann [125, pp. 746ff]. By minimizing w_c we increase g and have the additional benefit of reduced clipping of the cavity mode with the lens assembly as described in Fig. 2.4. As shown in Fig. 2.10, in theory we can make the mode waist arbitrarily small at the cost of approaching the edge of the green shaded stability region. In practice, aligning and locking the cavity close to the unstable region is experimentally challenging and not advisable. Instead we want to understand how the mirrors radii of curvature relate to the cavity waist. We therefore choose

---

12 We define the storage time as the time until the intensity decays by a factor $1/e$. Some references instead define it for the field decay, obtaining a factor of 2 between the two definitions.
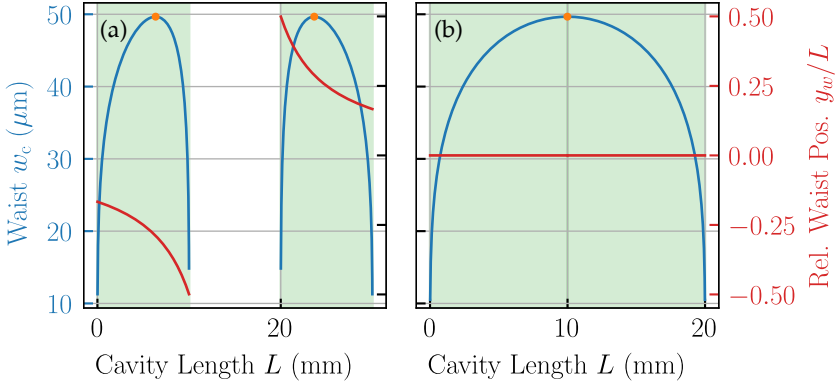
FIGURE 2.10: *Cavity mode waist of an optical cavity.* (a) and (b) show the cavity mode waist as well as its position relative to the cavity center [125], normalized by the cavity length. A relative waist position of -0.5 (0.5) corresponds to a focus on the mirror A (B), while $y_w/L = 0$ corresponds a focus in the center of the cavity. The green area denotes the stability area according to [125] while the orange dot marks the maximum mode waist. In (a) we have chosen radii of curvature of $\mathrm{ROC_A, ROC_B} = [20\,\mathrm{mm}, 10\,\mathrm{mm}]$ while (b) represents the symmetric case of $\mathrm{ROC_A} = \mathrm{ROC_B} = 10\,\mathrm{mm}$.

the cavity length to be well within the stability region, where the the cavity waist is maximal (orange dot in figure) and find

$$w_{\mathrm{c}}^2 = \frac{L\lambda}{\pi}\sqrt{\frac{g_A g_B(1 - g_A g_B)}{(g_A + g_B - 2g_A g_B)^2}} \tag{2.26}$$

$$\max(w_{\mathrm{c}}) = \sqrt{\frac{\lambda \min(\mathrm{ROC_A, ROC_B})}{2\pi}}, \tag{2.27}$$

with λ the laser wavelength. From Eq. (2.27) we see that we can achieve a small cavity mode waist by having at least one mirror with a small radius of curvature. In practice, we also need to be able to insert the optical tweezer between the cavity mirrors ($L > 5\,\mathrm{mm}$) and would like to trap the particle at the cavity mode waist position. From Fig. 2.10 we conclude that a symmetric setup ($\mathrm{ROC_A} = \mathrm{ROC_B}$) is preferable since the mode waist is always in the center of the cavity, regardless of the cavity length. To further boost g we

	Generation 1	Generation 2
Manufacturer	ECI	Layertec
Reflectivity	99.986%	(99.9975%, 99.9917%)
Transmission	125 ppm	(20 ppm, 79 ppm)
ROC (mm)	10	(10, 10)
Finesse	22k	58k
Length (mm)	6.46	6.85
Cavity Waist (μm)	48	48
Linewidth $\kappa/2\pi$ (MHz)	1.06	0.32
$\omega_{\mathrm{fsr}}/2\pi$ (GHz)	23.32	21.88
$(\omega_{q10} - \omega_{q00})/2\pi$ (GHz)	7.6	8.7
opt. coupling $|g|/2\pi$ (kHz)	49.8	47.8
Purcell Factor 2C	4.5	11.7

TABLE 2.2: Comparison of two generations of cavities. In lines with two values per generation the first value refers to mirror A, the mirror through which the cavity is locked and the second value refers to mirror B, the mirror through which the particle motion is detected. The top section of the table is according to specifications by the manufacturer, while the bottom section is extracted or derived from measurements. High finesse coatings on small radii of curvature mirrors present a challenge to manufacturers. Both creating a spherical surface with low surface roughness, as well as obtaining a homogeneous coating all over the mirror surface are not straight forward in this parameter regime. The main advantages of the second generation are a lower linewidth obtained through better mirror coatings, as well as an improved particle detection through stronger Purcell enhancement (Eq. (2.36)) and asymmetric transmission. Furthermore, the symmetric radii of curvature make it possible to position the particle in the cavity focus as shown in Fig. 2.10. All parameters apply at a wavelength $\lambda = 1550\,\mathrm{nm}$. The optomechanical coupling rates are calculated with Eq. (4.2) for a tweezer power $P_{\mathrm{tw}} = 500\,\mathrm{mW}$ and silica particles of radius $R = 70\,\mathrm{nm}$ with density $\rho = 2200\,\mathrm{kg/m^3}$ and permittivity $\epsilon_{\mathrm{p}} = 2.07$ [136, 137]. Furthermore, we used the mechanical frequencies from Tab. 2.1 for each cavity generation, matching the trapping lens generation.

reduce L as close as possible[13] to 5 mm but have to keep in mind that this also reduces the linewidth κ. To obtain the desired value for κ we choose the mirror coatings $\mathcal{R}_{AB} = \sqrt{\mathcal{R}_A \mathcal{R}_B}$ accordingly. Since we want to detect the particle motion via light leaking through one of the mirrors, instead of combining both mirror outputs or alternatively losing half the power, it is for us desirable to choose $\mathcal{R}_A > \mathcal{R}_B$. During the project we did experiments with a first generation optical cavity and finally upgraded to a second generation. A comparison of the two cavity generations is given in Tab. 2.2.

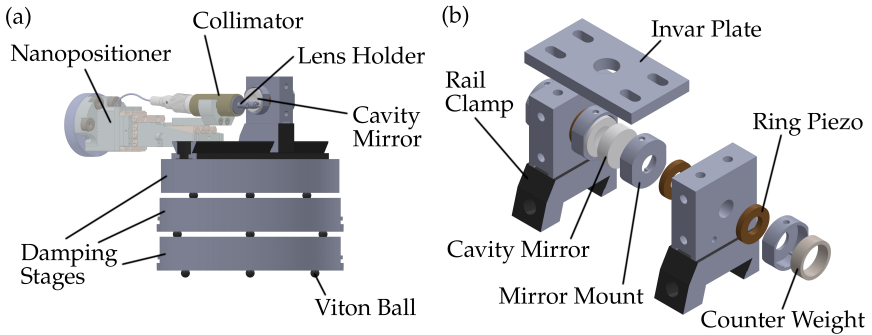### 2.3.5 *The Cavity Holder*

FIGURE 2.11: *Cavity housing with damping stages.* (a) We show the damping system of the cavity housing. For clarity we remove parts of the cavity housing as well as one mirror. The cavity mirror is mounted in a holder, which is in turn placed on a rail on the top damping stage. Each damping stage is separated by three *Viton* balls to absorb vibrations. Next to the cavity mirror we see the optical tweezer system after moving the arm into the cavity. (b) Cavity housing, with an exploded view of the right mirror holder. For clarity we removed the side invar plates (similar designs as for the top invar plate) that minimize motion of the two mirror holders w.r.t. each other. The mirror is fixed with a screw to the mirror mount which in turn is glued to a ring piezo actuator and then to the center block made from invar. The cavity length can be locked by driving the piezo actuators. To minimize holder motion while driving the piezo we choose a symmetric configuration of the same ring piezo actuator, a mirror mount and a counter weight on the opposite side of the center block. Light can be coupled into and out of the cavity through the center through-hole.

---

13 minimal length which still allows the insertion of the trapping lens assembly into the cavity
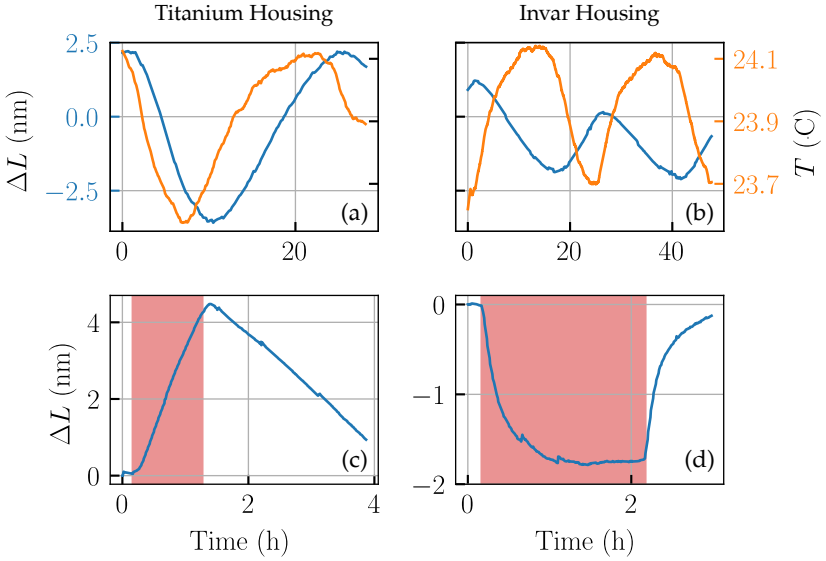
FIGURE 2.12: *Thermal drift of cavity length.* For all figures we lock an optical cavity to a laser with wavelength $\lambda = 1550$ nm by applying a voltage to a piezo actuator behind one of the mirrors. We previously calibrated the piezo expansion in nm for an applied voltage and characterized the laser frequency drift over a day to be less than 30 MHz, corresponding to cavity length fluctuations of 175 pm. The cavity housing is as described in Fig. 2.11, with side/top plates fabricated from titanium in the left column and from invar in the right column. In all figures we plot the cavity length change over time (blue curve). In (a) and (b) the optical tweezer is not placed inside the cavity and the trap laser is turned off. A temperature sensor inside the vacuum chamber measures the temperature drift over time (orange curves). We observe a slow temperature drift with periodicity of ≈ 24 h and a peak-to-peak swing of $\approx 0.5\,°C$. With a delay of ≈ 4 h the cavity reacts to the temperature drift by expanding or contracting for a temperature increase in the cases of (a) and (b) respectively. In (c) and (d) we position the optical tweezer inside the cavity and turn on the tweezer ($P_{tw} \approx 500$ mW) for a period of time (red shaded area). Some stray light is able to hit the cavity housing, thereby heating up the components. In (c) we observe a linear expansion of the cavity until the tweezer is turned off again. In (b), on the other hand, the cavity contracts and reaches an equilibrium value after ≈ 1 h.

In this section we describe the technical details of our optical cavity. In addition to an active PDH feedback system to lock the cavity length we implement a passive stabilization system to improve mechanical stability. All components are shown in Fig. 2.11. The cavity is mounted on top of a stack of three damping stages. Each stage is fabricated from steel and separated by *Viton*[14] balls. The stack including the cavity is kept under vacuum, protecting the system from acoustic noise as well as preventing contamination of the mirrors. Both cavity mirrors are mounted in cavity holders which in turn are mounted on rail clamps, cf. Fig. 2.11(b). Thereby, we have flexibility to change the cavity length, while keeping the mirrors on axis. To ensure precise alignment of the two cavity holders w.r.t. each other, we mount three invar plates from the top and the two sides to the mirror holders. Each mirror holder contains a set of a two mirror mounts, two ring piezo actuators and a counter weight. By applying a voltage to both ring piezos on opposite sides of the center block, we can change the cavity length without shaking the holder. The mirror mounts were initially fabricated from aluminum to be lightweight while the center blocks and side/top plates were made from titanium for mechanical stability. We observed that the components heated up during experiments from stray light inducing a slow drift of the cavity length which could eventually not be compensated anymore by adjusting the piezo voltage. We improved thermal stability by switching these parts to components fabricated from invar. The improvement of switching the side/top plates to invar is shown in Fig. 2.12. We observe the length drift dependence on temperature to flip sign and reduce by a factor of two in (a) and (b). Furthermore, the length change when turning on the optical tweezer inside the optical cavity saturates within a feasible time ($\approx 1\,\text{h}$). We assume that a cavity expansion originates from expansion of the side/top plates, while a contraction is due to expansion of the mirror mounts or center block. Initially the effect from the titanium plates is dominant, after replacement with invar we only observe the latter. We explain the saturation in (d) by a smaller thermal capacity of the expanding components (e.g. aluminum mirror mount).

2.4 HIGH PRECISION PARTICLE MOTION DETECTION

As the particle and especially its oscillation amplitude are too small to be seen by eye or camera, we rely on interference techniques. We use the

---

14 *Viton* is a vacuum compatible fluoroelastomer by *DuPont de Nemours*, also called *FKM* according to the DIN-ISO norm.

optical tweezer not only for trapping the particle, but also to detect the particle motion. In a homodyne detection setup the light, scattered by the particle, is interfered with a local oscillator beam at equal frequency and controlled phase difference. In a heterodyne detection setup, on the other hand, the local oscillator is shifted in frequency [138]. For the purpose of efficient detection, one must also ensure a high mode match between the local oscillator and the information pattern of the c.m. mode of interest [71]. In either way, the detector signal has to be related to an absolute particle position by applying a calibration. One option is to relate the area under the PSD to the c.m. temperature after initially calibrating the detector at moderate vacuum and no cooling techniques applied, i.e. the particle motion is in thermal equilibrium with the surrounding gas [114]. This method benefits from homodyne detection as Stokes and anti-Stokes scattered light are mapped to the same detection frequency, increasing signal-to-noise ratio compared to heterodyne detection. A second option based on sideband-thermometry is described in Sec. 4.4. It requires heterodyne detection, as the Stokes and anti-Stokes sidebands need to be spectrally separated in the detected signal. In this work we apply both homodyne and heterodyne detection schemes. As we use the quadrant photodetector built by Erik Hebestreit in combination with the calibration method he describes we refer to his thesis [114] for more details and focus in this section solely on heterodyne detection, after introducing how to obtain the right phase between signal and reference beam on a balanced detector through clever use of beam splitters.

2.4.1   *Beam Splitters and Phase Retarders*

We understand beam splitters as optical components that split an incoming light field into a transmitted and reflected component. The split ratio can be either fixed or is given by the polarization of the incoming light field, which is the case for a so-called polarizing beam splitter (PBS). We can also use beam splitters in reverse to overlap two cross-polarized incoming light beams. Phase retarders impose a phase delay between the vertical and horizontal polarization component of an incoming beam. They can be used e.g. to transform linearly polarized light into circularly polarized light (quarter-wave plate) and vice-versa or to rotate linearly polarized light (half-wave plate). In this section we discuss how wave plates can be combined with PBS to interfere two light fields on a balanced detector.
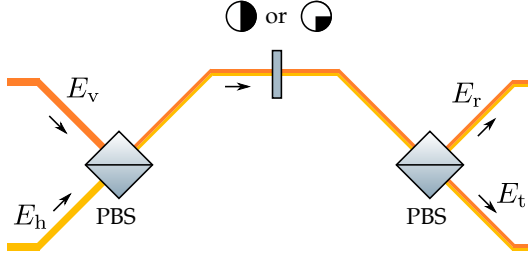
FIGURE 2.13: *Light fields passing through polarizing and phase retarding optics.* Two cross-polarized light fields are combined using a PBS, pass through either a half- or quarter-wave plate and are split again by a PBS.

To built a heterodyne detection setup as described in Chp. 2.4.2 we need to understand the impact of PBS and phase retarders on light fields as shown in Fig. 2.13. We use this setup to copropagate two cross-polarized light-fields by letting them pass through the PBS, tuning their polarization state with either a half- or quarter-wave plate and, finally, split them with a PBS. In practice, the two outputs would be sent to a balanced photodetector which subtracts the two outputs from each other. We employ the Jones calculus to describe the evolution of the fields, while propagating through the setup just described [139].

Following the Jones calculus, horizontally and vertically polarized light fields can be expressed by vectors

$$\boldsymbol{E}_{\mathrm{h}} := \begin{pmatrix} E_{\mathrm{h}} \\ 0 \end{pmatrix}, \quad \boldsymbol{E}_{\mathrm{v}} := \begin{pmatrix} 0 \\ E_{\mathrm{v}} \end{pmatrix}$$

while half- and quarter-wave plate's are represented by matrices

$$H = e^{-\frac{i\pi}{2}} \begin{pmatrix} \cos^2\theta - \sin^2\theta & 2\cos\theta\sin\theta \\ 2\cos\theta\sin\theta & \sin^2\theta - \cos^2\theta \end{pmatrix}$$

$$Q = e^{-\frac{i\pi}{4}} \begin{pmatrix} \cos^2\theta + i\sin^2\theta & (1-i)\cos\theta\sin\theta \\ (1-i)\cos\theta\sin\theta & \sin^2\theta + i\cos^2\theta \end{pmatrix}$$

as well as polarizers

$$P_h = \begin{pmatrix} 1 & 0 \\ 0 & 0 \end{pmatrix}, \quad P_v = \begin{pmatrix} 0 & 0 \\ 0 & 1 \end{pmatrix}.$$

In the wave plate matrices θ represents the angle of the wave plates fast axis w.r.t. horizontal polarization. Combining these definitions we can write down the equations for fields E_t and E_r as defined in Fig. 2.13,

$$E_t = iP_h W(E_v + iE_h)$$
$$E_r = P_v W(E_v + iE_h)$$

with $W = H, Q$ representing either the half- or quarter-wave plate. After inserting all definitions we calculate the transmitted and reflected field in the case of using a quarter-wave plate as

$$E_{t,Q} = -E_h \left(i\sin^2\theta + \cos^2\theta \right) e^{-\frac{i\pi}{4}} + iE_v \left(1 - i\right) e^{-\frac{i\pi}{4}} \sin\theta\cos\theta$$
$$E_{r,Q} = iE_h \left(1 - i\right) e^{-\frac{i\pi}{4}} \sin\theta\cos\theta + E_v \left(\sin^2\theta + i\cos^2\theta \right) e^{-\frac{i\pi}{4}}.$$

We can choose $\theta = \frac{\pi}{4}(2n - 1)$ for $n \in \mathbb{Z}$ to balance the output power of both output ports of the PBS and derive formulas for the fields,

$$E_{t,Q}\left(\theta = \frac{\pi}{4}\right) = \frac{1}{\sqrt{2}}\left(-E_h + E_v\right)$$
$$E_{r,Q}\left(\theta = \frac{\pi}{4}\right) = \frac{1}{\sqrt{2}}\left(E_h + E_v\right) \tag{2.28}$$

In contrast inserting a half-wave plate leads to

$$E_{t,H} = iE_h \left(-\sin^2\theta + \cos^2\theta \right) + 2E_v \sin\theta\cos\theta$$
$$E_{r,H} = 2E_h \sin\theta\cos\theta - iE_v \left(\sin^2\theta - \cos^2\theta \right).$$

Once again, we choose the angle that guarantees a balanced detection at the PBS output, which in this case is $\theta = \frac{\pi}{8}(2n - 1)$ for $n \in \mathbb{Z}$. The transmitted and reflected fields are

$$E_{t,H}\left(\theta = \frac{\pi}{8}\right) = \frac{1}{\sqrt{2}}\left(iE_h + E_v\right)$$
$$E_{r,H}\left(\theta = \frac{\pi}{8}\right) = \frac{1}{\sqrt{2}}\left(E_h + iE_v\right). \tag{2.29}$$

In the next step we assume that a balanced photodiode is placed behind the PBS. It detects the intensity of the reflected field and transmitted field and calculates their difference $D \propto |E_r|^2 - |E_t|^2$. Here we are only qualitatively interested in the result of the calculation, hence the proportionality. In Sec. 2.4.2 we will rigorously derive the detector signal and introduce the necessary constants. Using Eq. (2.28) and Eq. (2.29) we calculate the detector signal D,

$$
\begin{aligned}
D_Q &\propto 2\operatorname{Re}(E_h E_v^*) \\
D_H &\propto 2\operatorname{Im}(E_h E_v^*).
\end{aligned}
\tag{2.30}
$$

To derive the balanced PBS output fields we assumed certain angles for θ despite the solution not being unique. Picking a different solution will flip the signs of the detector signal as does changing which PBS port is subtracted from which. Since the physics is not affected by this we decided to simplify the calculations by picking a certain value instead of repeating the derivations for each case. Choosing a half- or quarter-wave plate to balance the signal results in the detection of different quadratures of the light field. As we are typically interested in time-averaged quantities (e.g. PSD), the phase or sign with which we detect the incident light field does not affect our measurements. After explaining how to interfere light fields on a detector with a PBS we are ready to discuss our heterodyne detection scheme in the next section.

2.4.2 *Heterodyne Detection*

This section presents the working principle of heterodyne detection. Later, in Sec. 4.3, we will be particularly interested in the influence of relative intensity noise (RIN) and phase noise on the detected signal. We consider the case of two fields $E_s(t)$ and $E_{lo}(t)$ at different frequencies, interfering on a balanced detector as depicted in Fig. 2.14,

$$
\begin{aligned}
E_s(t) &= E_s^{(0)}(t - t_0)e^{-i[\omega t - k l_0 + \phi(t - t_0)]} \\
E_{lo}(t) &= E_{lo}^{(0)}(t - (t_0 + \tau_{lo}))e^{-i[\omega_{lo} t - k_{lo} l_0 - k_{lo} L_{lo} + \phi(t - (t_0 + \tau_{lo}))]}.
\end{aligned}
\tag{2.31}
$$

The laser takes the time t_0 to travel the common path length l_0 and τ_{lo} for the additional local oscillator arm length L_{lo}. The fields $E_s^{(0)}(t - t_0)$ and $E_{lo}^{(0)}(t - (t_0 + \tau_{lo}))$ denote fluctuating amplitudes of the input laser. Since the laser takes times t_0 on the signal arm and $t_0 + \tau_{lo}$ on the local oscillator

arm until it reaches the detector we have to consider the fluctuation at the respective time in the past. The real average field amplitudes are denoted by $\overline{E}_s^{(0)}$ and $\overline{E}_{lo}^{(0)}$. Similarly $\phi(t - t_0)$ and $\phi(t - (t_0 + \tau_{lo}))$ denote the fluctuating phases of the input laser. Frequencies and wave numbers are denoted by ω, k for the signal and ω_{lo}, k_{lo} for the local oscillator. We continue by writing the balanced intensity I of a monochromatic wave in vacuum [140] as

$$
\begin{aligned}
I &= \frac{c\epsilon_0}{2} \left[|E_s(t) + E_{lo}(t)|^2 - |E_s(t) - E_{lo}(t)|^2 \right] \\
&= c\epsilon_0 \left[E_s(t)E_{lo}^*(t) + E_s^*(t)E_{lo}(t) \right].
\end{aligned}
$$

Here c, ϵ_0 are the vacuum speed of light and permittivity. The detected power is given by multiplying the intensity with the detector area. To furthermore obtain the detector output voltage D we multiply the power with the detector responsivity R_D and detector gain G,

$$
D_0 := 4GR_D\sqrt{P_s P_{lo}} \tag{2.32}
$$

$$
D_I := \frac{D}{D_0} = \frac{E_s(t)E_{lo}^*(t) + E_s^*(t)E_{lo}(t)}{2\overline{E}_s^{(0)}\overline{E}_{lo}^{(0)}} \tag{2.33}
$$

Here P_s and P_{lo} are the power of the signal and local oscillator beam per photodiode respectively. With Eq. (2.31) we derive
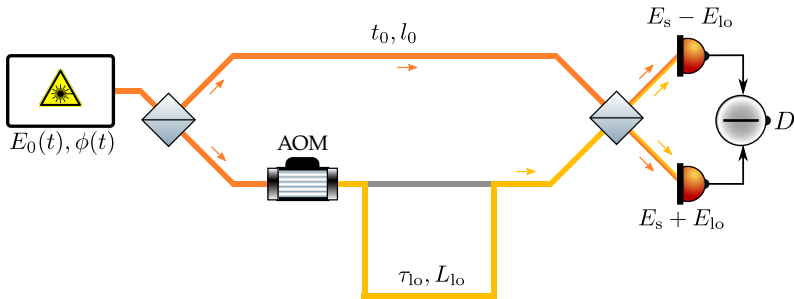

FIGURE 2.14: *Sketch of a heterodyne detection setup with fluctuating laser amplitude and phase. A laser with a fluctuating amplitude $E_0(t)$ and phase $\phi(t)$ is split. The laser on the upper path travels a distance l_0 within a time t_0 before impinging on a balanced detector. The laser on the lower arm is frequency shifted by an AOM and travels an additional distance of L_{lo} within a time τ_{lo} before being detected.*

$$\frac{E_s(t - t_0)E_{lo}^*(t - (t_0 + \tau_{lo}))}{E_s^{(0)}(t - t_0)E_{lo}^{(0)}(t - (t_0 + \tau_{lo}))} = \exp\{i[\Delta\omega t + \phi_0 + \Delta\phi(t)]\}$$

$$\Delta\omega := \omega_{lo} - \omega$$

$$\Delta\phi(t) := \phi(t - (t_0 + \tau_{lo})) - \phi(t - t_0)$$

$$\phi_0 := (k - k_{lo})l_0 - k_{lo}L_{lo}$$

and find the detector signal $D(t)$, by inserting the expression into Eq. (2.33),

$$\frac{D(t)}{D_0} = \frac{E_s^{(0)}(t - t_0)E_{lo}^{(0)}(t - (t_0 + \tau_{lo}))}{\overline{E}_s^{(0)}\overline{E}_{lo}^{(0)}} \cos\left(\Delta\omega t + \phi_0 + \Delta\phi\right). \qquad (2.34)$$

In the absence of amplitude and phase fluctuations of the input laser the expression simplifies to

$$D(t) \propto \sqrt{P_s P_{lo}} \cos\left(\Delta\omega t + \phi_0\right). \qquad (2.35)$$

We obtain a beating signal on the detector at frequency $\Delta\omega$, the difference frequency of signal and reference beam. The phase ϕ_0 depends on the path length difference of the two arms. It becomes evident from this expression, that a heterodyne detection is useful for sideband-thermometry. For $\Delta\omega \neq 0$ we are able to spectrally separate the Stokes sideband at $\Delta\omega - \Omega_q$ and anti-Stokes sideband at $\Delta\omega + \Omega_q$ of oscillator $q \in \{x, y, z\}$.

2.4.3 *Cavity Detection and Purcell Enhancement*

Recently, free space levitated particle experiments were able to detect the particle motion precisely enough to feedback cool its motion to the quantum ground-state [72, 73]. So far only the motion along the tweezer axis (z) can be measured accurately enough in free space to sufficiently cool the particle motion [71]. In levitated cavity optomechanics the increased detection efficiency, referred to as Purcell enhancement, enables ground state cooling and detection of the motion transversal to the tweezer [70]. In 1946 Edward Mills Purcell discovered the enhancement of spontaneous emission rates of atoms inside a resonant cavity [141]. Resonant cavities not only enhance spontaneous emission, but also light scattering rates [142] which can be quantified by the Purcell factor $2C$,

$$2C := \frac{P_{\text{c}}}{P_{\text{dp}}} = \frac{24c^2}{\pi\omega_{\text{c}}^2}\frac{\mathcal{F}}{w_{\text{c}}^2}. \tag{2.36}$$

We consider a dipole, driven by a free-space laser beam. The dipole scatters light and is placed inside an optical cavity. The Purcell factor gives the power of light scattered into the cavity P_{c} over the power scattered into free space P_{dp} (i.e. not into the cavity mode). The parameters in Eq. (2.36) are the cavity finesse $\mathcal{F}$, the cavity frequency ω_{c} and mode waist w_{c}. To increase the scattering into the cavity, it is therefore beneficial to minimize the mode waist, while increasing the cavity finesse.

In Fig. 2.15 we show our implementation of homo- and heterodyne setups, with qualitative detector outputs. In particular the heterodyne detector output is more involved than shown here, which will be discussed in Sec. 4.4. We want to give here a brief comparison between free space homodyne and cavity heterodyne detection to explain our choices of detection setups in the next chapters. We can calibrate the homodyne detector and relate the area under the peak in Fig. 2.15(b) to the particle's c.m. temperature, as described in [114]. To calibrate the detector it is crucial to turn off the cooling mechanism and bring the particle to thermal equilibrium with the surrounding gas. Once the free space detector is calibrated, we can extract c.m. temperatures for any cavity detuning or gas pressure, as long as the power of the trap beam does not drift. This robustness motivates us to use the free space detector for initial cooling experiments, which we present in Chapter 3.

At c.m. temperatures of a few millikelvin we reach the noise limit of the free space detector. Since the experimental stability does not allow for longer measurement times, we require to increase the detection efficiency. We obtain this through Purcell enhancement of the light scattered into the cavity and a detector behind the cavity mirror. To relate the area under the measured peak on the cavity detector to a c.m. temperature we need to calibrate the detector. We show in (c) that the heights of Stokes ($\Omega = \omega_{\text{lo}} - \Omega_y$) and anti-Stokes ($\Omega = \omega_{\text{lo}} + \Omega_y$) peaks depend on the cavity transfer function (see Sec. 2.3.1). The cavity linewidth is typically fixed during experiments, but the detuning can be tuned to affect the cooling strength of the cavity. If we far detune the cavity $\Delta \gg \Omega_y$ the c.m. motion is not cooled anymore, but also the detector signal disappears. It is therefore impossible to calibrate the detector with a particle in thermal equilibrium with the surrounding gas. Furthermore, the calibration factor depends on cavity detuning, as the amount of light coupling into the cavity in
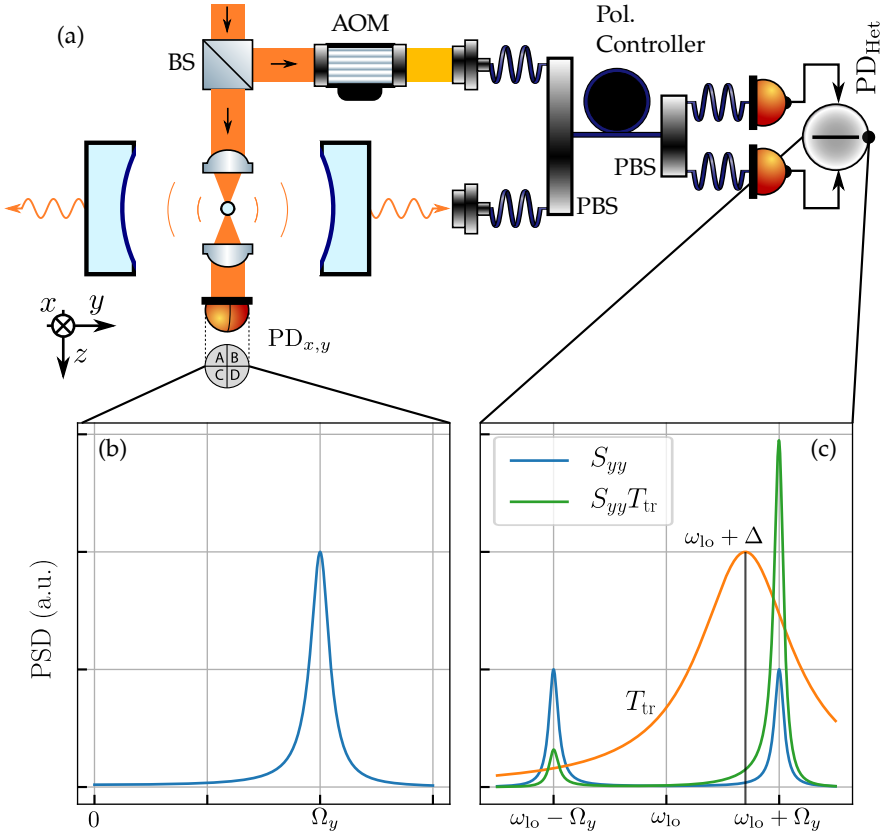
FIGURE 2.15: *Homo- and heterodyne detection with an optical cavity.* (a) A laser enters from the top left. Before forming an optical tweezer that traps a particle inside an optical cavity we pick off a portion of the light, which is frequency shifted by ω_{lo} and acts as a local oscillator. Light scattered from the particle in the forward direction is detected by a quadrant photo detector (QPD). Light coupled to the cavity, as well as the local oscillator are fed into a fiber-based version of the heterodyne detection scheme shown in Fig. 2.14. (b) Light scattered from the particle interferes on the QPD with light passing by the particle. By subtracting the signal of quadrant B and D from quadrants A and C we perform a homodyne measurement of the motion along *y*-direction. (c) Heterodyne measurement of the cavity output signal. Stokes and anti-Stokes peaks appear at $\omega_{lo} - \Omega_y$ and $\omega_{lo} + \Omega_y$ with reduced signal-to-noise compared to the homodyne detection. We overlay the cavity transfer function (orange) with a detuning of Δ to show how the anti-Stokes (Stokes) signal is enhanced (suppressed).

turn also depends on detuning. We can circumvent the direct calibration by using both the calibrated free space and cavity detector. In a regime where the free space detector is not yet limited by signal-to-noise, we can attribute a c.m. temperature to the cavity detector and thereby cross-calibrate the cavity detector. Once the signal-to-noise limit of the free space detector is reached, we can still measure c.m. temperatures with the cavity detector. Since experimental drifts affect the cavity detector more severely, the improvement on signal-to-noise comes with the cost of robustness.

To benefit from Purcell enhancement on the cavity detector we do not require a heterodyne detection scheme. However, it is convenient to use one, to be able to apply a technique referred to as sideband-thermometry, which we will explain in Sec. 4.4. This technique does not require detector calibration, but extracts c.m. temperatures directly from the asymmetry between the Stokes and anti-Stokes sidebands. To obtain accurate results through sideband-thermometry poses its own challenges, which we will discuss later.

3D COOLING OF A LEVITATED PARTICLE BY COHERENT SCATTERING

In 2019 we observed genuine cooling of all three spatial degrees of freedom of a nanoparticle levitated by an optical tweezer and coherently scattering into an optical cavity [68]. Additionally, we developed a theory describing our findings [103]. Simultaneously Delić et al. reported similar findings [69] and were the first to use the developed technique to ground-state cool a levitated nanoparticle in 2020 [70]. In the following sections we introduce our coherent scattering setup and summarize the theory which describes the particle-cavity dynamics.

3.1 THE COHERENT SCATTERING SETUP

So far we have introduced the core building blocks of our versatile levitated particle cavity machine in Chapter 2. In this chapter we elaborate on the interplay of optical tweezer with cavity and present our measurement results. After our initial 3D cooling experiments [68] the setup underwent several upgrades to lower the reachable c.m. phonon numbers. Those upgrades will be discussed in Sec. 4.1. At this point we focus on the state of the setup during the initial experiments as shown in a simplified sketch in Fig. 3.1. The components used to build the setup are listed in Tab. A.2. The experiments presented in this chapter are all performed using the first generation trapping lens (Tab. 2.1) as well as the first generation cavity (Tab. 2.2).

We split laser light at a wavelength $\lambda = 1550.0(5)$ nm into two beams, the lock beam at frequency $\omega_c = 2\pi c/\lambda$ and the tweezer beam. Subsequently the tweezer beam is sent through two AOMs in double-pass configuration shifting the frequency by Δ [143], resulting in a frequency $\omega_{tw} = \omega_c - \Delta$. The lock laser is phase modulated by an EOM to create sidebands and couples to the TEM_{00} mode of our optical cavity. The z polarized lock beam with an optical power of $11(1)\,\mu W$ is back reflected from the cavity and detected with a photodiode PD_{PDH}. From the detector signal we derive the Pound-Drever-Hall error signal and stabilize the cavity length at $L =$
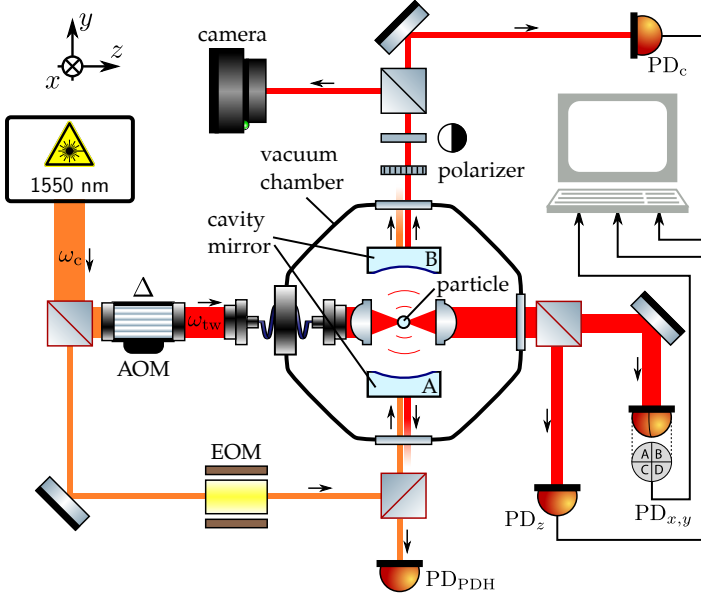
FIGURE 3.1: *Simplified coherent scattering setup for 3D cooling.* A single nanoparticle is levitated in an optical tweezer trap and positioned in the mode of an optical cavity. The particle is driven by the trapping light and scatters into the cavity mode as well as into free space. This scattered light is detected by the cavity photodetector PD_c and by the free space photodetectors PD_z and $PD_{x,y}$, respectively. We use a camera to image the mode leaking out of the cavity to ensure that both particle scattered light and lock beam couple to the TEM_{00} mode. Beam splitters with a black (red) border are polarizing (non-polarizing) beam splitters and the half circle indicates a half-wave plate.

6.46(8) mm as described in Sec. 2.3.2. The cavity linewidth is $\kappa/2\pi = 1.06(8)$ MHz and the finesse is $\mathcal{F} = 22(2) \times 10^3$.

The trap beam's detuning Δ can be tuned by controlling the AOM modulation frequency resulting in $\Delta/2\pi \in [-10, 10]$ MHz. To avoid trap power fluctuations when frequency tuning we feed the AOM output to a fiber amplifier, which operates in saturation. The amplifier output enters the vacuum chamber through a polarization-maintaining optical fiber, is collimated and forms an optical tweezer inside the lens holder assembly as described in Sec. 2.2. The silica particle with a radius of 70(5) nm is trapped in the x polarized tweezer beam with a focal power of $P_{tw} = 500(5)$ mW.

The particle motion is detected by our free space detectors PD_z and $PD_{x,y}$ with trap frequencies on the order of $\Omega_{x,y,z} \approx 2\pi \times \{120, 140, 40\}$ kHz.

Similar to [56] we can move the optical tweezer to scan the particle position along the cavity axis. Thermal drifts of the loading arm that hold the nanopositioner limit the particle position stability along the cavity axis to 50 nm as we will further elaborate in Sec. 4.2. We monitor the power behind cavity mirror B with PD_c. The signal on the photodiode is maximal for the particle at the center of the transversal Gaussian mode and at the intensity maximum along the standing wave (antinode) which is expected according to our calculations presented in Fig. 3.6. Since tweezer and lock beams are cross-polarized we use a polarizer to filter out the latter on the detection side of the cavity (behind mirror B).

3.2   POSITION DEPENDENT COOLING

In our first measurement, displayed in Fig. 3.2, we study the 3D c.m. temperatures $T_{x,y,z}$ and damping rates $\gamma_{x,y,z}$ of the particle as a function of gas pressure p. The c.m. temperatures are obtained from the area under the PSDs of the free space detectors $PD_{x,y}$ and PD_z as touched upon in Sec. 2.2 and thoroughly explained in [114]. We place the particle at different positions relative to the cavity intensity profile corresponding to different markers in the plot. A particle at the intensity maximum or anti-node is indicated by ▼, at the steep slope by ♦ and at the intensity minimum or node through ●. For cavity cooling by coherent scattering, the cavity is blue detuned from the tweezer light ($\Delta = 2\pi \times 400$ kHz). Fig. 3.2(a–c) show that the temperatures along all axes decrease, as the pressure and therewith heating due to interaction with room temperature gas molecules are reduced. Along x and y we observe lowest temperatures $T_x \approx 100$ mK and $T_y \approx 3$ mK at the node, limited by interaction with residual gas. For z, however, we find lowest temperatures $T_z \approx 80$ mK at the anti-node, starting to level off around a pressure of 10^{-4} mbar.

One key finding of experiment and theory is that not only the particle motion along the cavity axis (y) couples to the cavity mode, but also along the tweezer axis (z). By introducing a small tilt of the tweezer polarization and creating an overlap between x and the cavity axis we can not only couple the cavity mode to the y and z motion, but also x. To explain the particle-tweezer-cavity interaction we write down the interaction Hamiltonian according to [103, 144],

$$\hat{H}_{int} = -\frac{\alpha_{dp}}{2}\left[\boldsymbol{E}_{tw}(\hat{\boldsymbol{R}},t) + \hat{\boldsymbol{E}}_c(\hat{\boldsymbol{R}}) + \hat{\boldsymbol{E}}_{free}(\hat{\boldsymbol{R}})\right]^2$$
$$= \hat{H}_{t-t} + \hat{H}_{c-c} + \hat{H}_{f-f} + \hat{H}_{t-c} + \hat{H}_{t-f} + \hat{H}_{c-f}. \tag{3.1}$$

The polarizability of the particle α_{dp} is given in Eq. (3.13). The operator $\hat{\boldsymbol{R}}$ denotes the c.m. position relative to the focus of the optical tweezer. The intense tweezer field is treated as a classical field $\boldsymbol{E}_{tw}$ while the free space and cavity modes, populated via light scattered by the particle are represented by operators $\hat{\boldsymbol{E}}_{free}$ and $\hat{\boldsymbol{E}}_c$. According to [103] for small particles and away from the photon recoil limit we can neglect $\hat{H}_{f-f} \propto \hat{\boldsymbol{E}}_{free}^2$, $\hat{H}_{t-f} \propto \boldsymbol{E}_{tw}\hat{\boldsymbol{E}}_{free}$ and $\hat{H}_{c-f} \propto \hat{\boldsymbol{E}}_{free}\hat{\boldsymbol{E}}_c$. The term $\hat{H}_{t-t} \propto \boldsymbol{E}_{tw}^2$ represents the optical tweezer and is responsible for trapping of the particle. The remaining two terms $\hat{H}_{c-c} \propto \hat{\boldsymbol{E}}_c^2$ and $\hat{H}_{t-c} \propto \boldsymbol{E}_{tw}\hat{\boldsymbol{E}}_c$ incorporate the direct cavity drive and coherent scattering contribution respectively [97]. After a transformation the interaction between the system degrees of freedom is [103]

$$\hat{V}_0 = \sum_{q=\{x,y,z\}} (g_q - \alpha_c g_{cq})\hat{c}^\dagger(\hat{b}^\dagger + \hat{b}) + \text{H.c.} \tag{3.2}$$

Here $\hat{c}$ ($\hat{b}$) and $\hat{c}^\dagger$ ($\hat{b}^\dagger$) are the photon (phonon) annihilation and creation operators, respectively. The optomechanical coupling rates quantify the interaction strength between optical and mechanical modes. In Eq. (3.2) we introduced two optomechanical coupling rates g_q and g_{cq}. They arise from the terms $\hat{H}_{t-c}$ and $\hat{H}_{c-c}$ in the interaction Hamiltonian. We refer to the first one as the coherent scattering optomechanical coupling rate as it originates from the interference of tweezer and cavity field and denote the latter as direct optomechanical coupling rate. The motion along the tweezer axis (z) does not directly couple to the cavity and hence $g_{cz} = 0$. The transformation to obtain $\hat{V}_0$ includes a displacement of cavity modes mapping $\hat{c} \mapsto \hat{c} + \alpha_c$. The coefficient α_c can be calculated according to [103], but it is not straight-forward. Since the direct optomechanical coupling rates are negligible for our experimental parameters [103] we focus on the coupling rates originating from coherent scattering,

$$\begin{bmatrix} g_x \\ g_y \\ g_z \end{bmatrix} = -(G/2) \begin{bmatrix} k_c x_{zpf} \sin\phi \sin\theta \\ k_c y_{zpf} \sin\phi \cos\theta \\ -i k_{tw} z_{zpf} \cos\phi \end{bmatrix}, \tag{3.3}$$
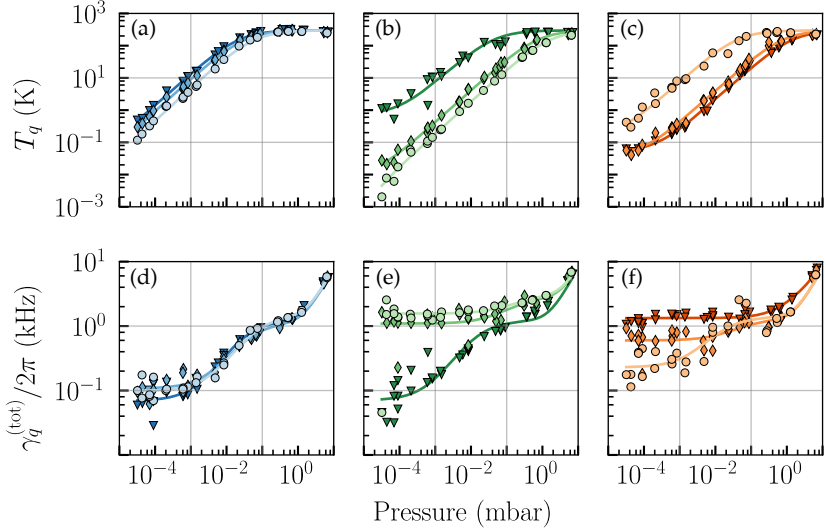
FIGURE 3.2: *Three-dimensional cavity cooling of an optically levitated nanoparticle by coherent scattering.* For a cavity detuning $\Delta = 2\pi \times 400\,\text{kHz}$ we show the cooling as a function of pressure along x in the first column (blue), along y in the second column (green) and along z in the third column (red). The cooling is compared for a nanoparticle positioned at the node ($\bullet$), steep slope ($\blacklozenge$) and anti-node ($\blacktriangledown$) of the cavity standing wave. (a–c) Particle temperatures. (d–f) Particle damping rates. Both temperatures and damping rates decrease as a function of gas pressure and are position dependent. Solid lines represent a fit to a two bath model and a damping rate model given by Eqs. (3.5) and (3.8).

with $G = \alpha_{\text{dp}} E_0 \sqrt{\frac{\omega_\text{c}}{2\hbar\epsilon_0 V_\text{c}}}$, $k_\text{c} = k_\text{tw} = 2\pi/\lambda$ and $q_{\text{zpf}} = \sqrt{\frac{\hbar}{2m\Omega_q}}$ the zero-point fluctuation of oscillator $q \in \{x, y, z\}$. The particle mass is denoted by m, the cavity mode volume by V_c and the electric field amplitude E_0 in the focus of an approximative Gaussian beam is given by $E_0 = \sqrt{4P_{\text{tw}}/c\epsilon_0\pi w_x w_y}$. Here ϵ_0 is the vacuum permittivity and w_x, w_y are the $1/e^2$ intensity radii of the focused beam. The angle $\theta \approx 10°$ denotes the tilt of the trap's y axis w.r.t the cavity axis. The angle ϕ indicates the particle position relative to the cavity intensity profile. For $\phi = 0$ the particle is at the intensity maximum or anti-node ($\blacktriangledown$), for $\phi = \pi/4$ at the steep slope ($\blacklozenge$) and for $\phi = \pi/2$ at the intensity minimum or node ($\bullet$). According to Eqs. (3.2) and (3.3) we can convert phonons into cavity photons and vice versa at rates, that depend

on the tweezer polarization and particle position. If we choose the correct cavity detuning and linewidth we can enhance the process that annihilates phonons and dissipate cavity photons to the environment, thereby cooling the particle motion. We will investigate how the cavity cooling rate depends on optomechanical coupling rate, cavity detuning and linewidth in Sec. 4.1. We point out here that either the x, y axes or z axis can be cooled effectively, but not all at the same time, due to the dependence on ϕ. When choosing $\phi = 0$ the cavity is strongly populated and phase noise can potentially limit the cooling performance as reported in the case of direct cavity pumping [63]. Furthermore, the particle scatters x-polarized light like a dipole predominantly in the y direction, thereby coupling more information about the y motion into the cavity. Combining these arguments, the y oscillator is the one most promising for ground-state cooling. To describe our measurements in Fig. 3.2(a–c) we employ a coupled bath model to fit the solid lines. Following the approach in [51] we assume that the oscillators are in equilibrium with a set of thermal baths,

$$\overline{n}_q = \frac{\Gamma_q}{\gamma_q} = \frac{\Gamma_q^{(p)} + \Gamma_q^{(r)} + \Gamma_q^{(d)}}{\gamma^{(p)} + \gamma_q^{(r)} + \gamma_q^{(c)}}. \tag{3.4}$$

Here Γ_q and γ_q are the phonon heating and damping rates of oscillator $q \in \{x, y, z\}$ respectively. For large phonon numbers as is the case in Fig. 3.2 we can write $\overline{n}_q = k_B T_q / \hbar \Omega_q$ according to Eq. (2.4) and obtain for the c.m. temperatures

$$T_q = \frac{\widetilde{\Gamma}_q}{\gamma_q} = \frac{\widetilde{\Gamma}^{(p)} + \widetilde{\Gamma}_q^{(r)} + \widetilde{\Gamma}_q^{(d)}}{\gamma^{(p)} + \gamma_q^{(r)} + \gamma_q^{(c)}}. \tag{3.5}$$

The temperature and phonon heating rates are related through $\Gamma_q = k_B \widetilde{\Gamma}_q / \hbar \Omega_q$. The rates $\widetilde{\Gamma}^{(p)}$ and $\gamma^{(p)}$ originate from a coupling to the surrounding gas molecules, are dominant at high pressure but become gradually more negligible when approaching ultra high vacuum [47, 145],

$$\gamma^{(p)} \approx 0.619 \frac{6\pi R^2}{m} p \sqrt{\frac{2M}{\pi N_A k_B T}} \tag{3.6}$$

$$\widetilde{\Gamma}^{(p)} = T \gamma^{(p)}. \tag{3.7}$$

Here the particle radius and mass are given by R and m, while the gas pressure and temperature are p and T. We denote the molar mass of the surrounding air by M and Avogadro's constant by N_A. The approximation of Eq. (3.6) breaks down at high pressure but describes the system well at moderate vacuum [114]. A coupling to the photon bath is described by the rates $\widetilde{\Gamma}^{(r)}$ and $\gamma_q^{(r)}$ which only become comparable to the coupling to the surrounding gas at pressures below 10^{-8} mbar [51]. The optical cavity cools and thereby damps the particle motion which is expressed by $\gamma_q^{(c)}$. We add an additional heating rate $\widetilde{\Gamma}^{(d)}$ which incorporates other heating sources which we will investigate below.

In Fig. 3.2(d–f) we independently extract the damping rates from the width of the peak in the PSD. At high pressures cavity backaction is negligible and the damping decreases linearly with pressure as shown in Eq. (3.6). In the intermediate pressure regime ($\approx 10^{-2}$ mbar) cooling is not yet strong enough to dominate the damping and gas damping is not strong enough anymore to prevent the particle from experiencing nonlinearities of the trapping potential. Following the calculations of [114] the measured peak width $\gamma_q^{(tot)}$ (FWHM) can be related to the damping rates through

$$\gamma_q^{(tot)} = \sqrt{\gamma_q^{(nl)2} + \left(\gamma^{(p)} + \gamma_q^{(c)}\right)^2}. \tag{3.8}$$

The nonlinear broadenings $\gamma_q^{(nl)}$ depend on the trapping beam Duffing parameters and all three oscillation amplitudes. Finally, at sufficiently low pressure and for efficient cavity cooling, the damping rates level off, and $\gamma_q \rightarrow \gamma_q^{(c)}$ reaching a maximal cavity damping of $2\pi \times 1.3\,\text{kHz}$. We obtain the solid lines in Fig. 3.2(d–f) by a fit to Eq. (3.8).

3.3 CAVITY COOLING DYNAMICS

Relaxation measurements are a useful tool to measure cooling and heating rates independently [146]. We normally require the particle to be in thermal equilibrium to attribute an effective temperature T_{cm}. In relaxation measurements we investigate the dynamics from one thermal state into another one, either from uncooled to cooled or the other way around. The rate equation describes the time evolution of the average particle energy during the relaxation process. Since it is intrinsically impossible to wait for equilibration during the relaxation process, we have to repeat the measurement many
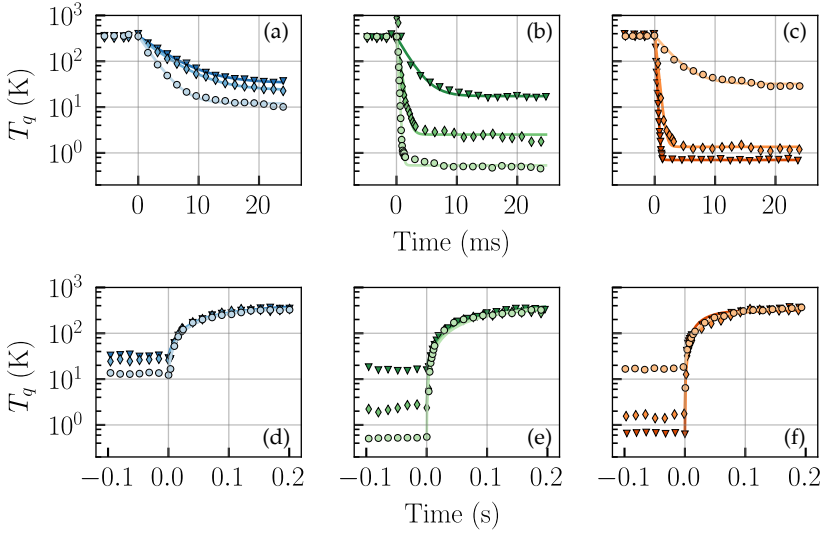
FIGURE 3.3: *Cavity cooling and reheating time traces of a nanoparticle* at $p = 3(1) \times 10^{-3}$ mbar averaged over > 150 realizations. Markers and colors as in Fig. 3.2. (a–c) At $t = 0$ cavity cooling is turned on and the decrease of T_x, T_y and T_z is shown over time. (d–e) At $t = 0$ cavity cooling is turned off and the increase of T_x, T_y and T_z is shown over time. Solid lines represent fits of the particle temperatures to a bounded exponential growth model (Eq. (3.9)).

times and average over all realizations (> 150) to find the average energy. Instead of solving the rate equation, here we use the result from [114],

$$T_q(t) = T_q^{(\infty)} + (T_q^{(0)} - T_q^{(\infty)})e^{-\gamma_q^{(eq)}t}. \tag{3.9}$$

We define the initial c.m. temperature of the process as $T_q^{(0)}$, the final one as $T_q^{(\infty)}$ and the equilibration rate as $\gamma_q^{(eq)}$. We conduct the relaxation experiments at $3(1) \times 10^{-3}$ mbar as there the particle motion is mainly damped by cavity backaction, when turning on the cavity (see Fig. 3.2(d–f)). Additionally, the gas heating rate is sufficiently high to observe equilibration in less than a second after turning off the cavity. Technically we turn the cavity on and off by switching the detuning Δ from $2\pi \times 400$ kHz to $2\pi \times 20$ MHz and vice versa.

In case of our cavity cooling experiments (Fig. 3.3(a–c)), where we start from the uncooled state and instantaneously turn on cavity cooling ($t = 0$), the relaxation rate is given by the cavity cooling rate $\gamma_q^{(eq)} = \gamma_q^{(c)}$. The fitted rates agree better than a factor of two with values obtained from the PSD peak width as shown in Fig. 3.2. The remaining discrepancy is explained by uncertainties of the pressure measurement and drifts of the system (e.g. tweezer power, particle position).

In case of the heating experiments (Fig. 3.3(d–f)) where we start from a cooled particle and suddenly turn off cavity cooling ($t = 0$) we expect the heating rate to be dominated by residual gas heating as we are not in the recoil limit ($\gamma_q^{(eq)} = \widetilde{\Gamma}^{(p)}/T_q^{(\infty)}$). Indeed, we extract $\gamma_q^{(eq)} \approx 2\pi \times 2.5(5)\,\text{Hz}$ along all three motional axes as expected from gas heating (Eq. (3.6)). We want to point out that any heating rate (e.g. $\widetilde{\Gamma}_q^{(d)}$) that originates from a feedback mechanism via the optical cavity is hidden in these experiments. The reason is that, when turning off the cooling mechanism by detuning the cavity to $\Delta = 2\pi \times 20\,\text{MHz}$, we also remove the heating effect.

3.4 CAVITY COOLING PARAMETERS

In our third experiment we confirm that our parameters do not significantly limit our cooling efficiency. So far, we have used a detuning $\Delta = 2\pi \times 400\,\text{kHz}$ and a tweezer power $P_{tw} = 500(5)\,\text{mW}$. Since our optical trap is fiber coupled it becomes technically challenging to increase optical power significantly without harming the fiber facet. In Fig. 3.4(a–c) we show the position dependent particle temperatures as a function of detuning. Since the cavity linewidth is large compared to the mechanical frequencies of the particle ($\kappa > \Omega_{x,y,z}$), the optimal detuning $\Delta = 2\pi \times 400\,\text{kHz}$ is approximately the same for all three oscillators. For $\Delta \lesssim 2\pi \times 300\,\text{kHz}$ we enter a regime where $g^2 \gtrsim |\Delta|\Omega_{x,y,z}$ and the system becomes dynamically unstable which results in particle loss [103, 147].

At large detunings, $\Delta \gtrsim 2\pi \times 10\,\text{MHz}$, we observe no influence of the cavity on the particle c.m. temperatures. This motivates the chosen detuning of $2\pi \times 20\,\text{MHz}$ for switching off cavity cooling in the experiments shown in Fig. 3.3. In Fig. 3.4(d) we show the c.m. temperature of the x, y (z) oscillator, for the particle positioned in the cavity node (antinode) as a function of trapping power. Sweeping the power from 240 to 500 mW results in stronger cavity cooling and lower particle temperatures. The fiber-coupled optical tweezer prevents us from increasing the power further. In Sec. 4.1 we will analyze the power dependence of cavity cooling in detail. According to
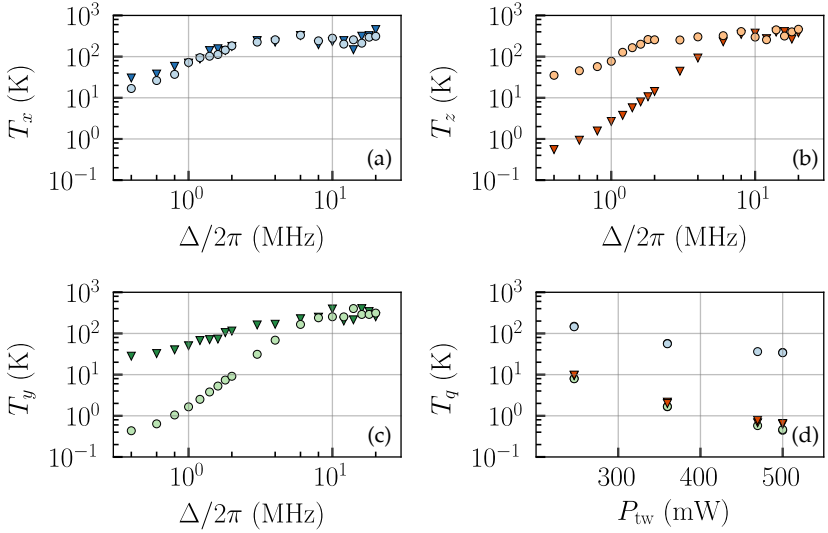
FIGURE 3.4: *Detuning and power dependence of 3D cavity cooling* at $p = 3(1) \times 10^{-3}$ mbar. Markers and colors as in Fig. 3.2. (a–c) At tweezer power $P_{\mathrm{tw}} = 0.50(5)$W the nanoparticle temperatures increase as the cavity detuning Δ reaches values $\gtrsim \kappa$. (d) Particle c.m. temperatures for best cooling positions of the particle as function of tweezer power at detuning $\Delta = 2\pi \times 400$ kHz.

Eq. (4.2) we indeed expect the optomechanical coupling and hence cooling rate to slightly increase for higher trapping power. When interpreting the trend in Fig. 3.4(d) we have to be careful, increasing the power not only increases the optomechanical coupling rate, but also the trap frequencies. As the trap frequencies approach Δ also the enhancement of anti-Stokes scattering becomes stronger and thereby the cavity cooling. Once the trap frequencies are sufficiently close to Δ the power increase becomes less impactful and potentially even increases the relevance of trap displacement noise $\widetilde{\Gamma}_q^{(\mathrm{d})}$. Additionally, increasing trap power in our setup is challenging due to the fiber coupling of the optical tweezer. In Sec. 4.1 we will discuss the impact of all experimental parameters on minimal phonon occupations in more detail, based on the theory of [103].

3.5 LIMITS OF CAVITY COOLING BY COHERENT SCATTERING

In our first experiment, shown in Fig. 3.2 we were able to match the data to a coupled bath model by introducing an additional heating rate $\widetilde{\Gamma}_q^{(d)}$ which we refer to as trap displacement noise in [68, 103] accounting for a shaking of the optical tweezer w.r.t the cavity intensity profile. To test the validity of this we employ a more complex model that is derived by solving the Hamiltonian in Eq. (3.1) according to [103]. The average phonon number is given by

$$\overline{n}_q = \frac{A - B + C}{4|g_q|^2 \Delta \kappa \Omega_q [4|g_q|^2 \Delta - (\Delta^2 + \kappa^2)\Omega_q]}, \tag{3.10}$$

with

$$
\begin{aligned}
A =\,& 2|g_q|^4 \Delta [\Delta^2 \kappa + \kappa^3 + 4\Delta\Omega_q(\Gamma_q/2 - \kappa) + 2\kappa\Omega_q^2] \\
B =\,& \Gamma_q/2\Omega_q(\Delta^2 + \kappa^2)[\kappa^2 + (\Delta - \Omega_q)^2][\kappa^2 + (\Delta + \Omega_q)^2] \\
C =\,& |g_q|^2\{-\kappa\Omega_q(\Delta^2 + \kappa^2)[\kappa^2 + (\Delta - \Omega)^2] \\
& + \Gamma_q\Delta[2\Omega_q^4 + \Omega_q^2(2\kappa^2 - 5\Delta^2) + (\Delta^2 + \kappa^2)^2]\}.
\end{aligned}
$$

The formula is valid at low gas pressure (i.e. the damping due to gas molecules $\gamma^{(p)} \ll \Omega_q, \kappa, |g_q|$ for $q \in \{x, y, z\}$) and only one motional axis is allowed to couple to the cavity at once. The thermal bath of free space particle experiments consists of the surrounding gas, the feedback system and incident photons. In addition we have to include the optical cavity in our coupled bath model. Both the cavity and particle exchange energy and both are in contact with the environment. To obtain a coupled bath expression as proposed in Eq. (3.4) we consider different limits of Eq. (3.10) taking into account the time scales of the different interactions and choosing a cavity detuning $\Delta = \Omega_q$. We write [103]

$$
\overline{n}_q \approx
\begin{cases}
\Gamma_q/\kappa & \text{for } \kappa/2 \ll |g_q| \ll \Omega_q \\
2\Gamma_q/\kappa & \text{for } \kappa/2 \approx |g_q| \ll \Omega_q \\
\kappa\Gamma_q/4|g_q|^2 & \text{for } |g_q| \ll \kappa/2 \ll \Omega_q.
\end{cases}
\tag{3.11}
$$

Here $\Gamma_q = \Gamma_q^{(r)} + \Gamma_q^{(d)} + \Gamma_q^{(p)}$ denotes the sum of all relevant phonon heating rates, that we introduced in Sec. 3.2. As explained before we ne-

glect photon recoil $\Gamma_q^{(r)}$ and write the expression for the trap displacement noise [103, 148, 149],

$$\Gamma_q^{(d)} = \frac{\pi}{2} \frac{\Omega_q^2}{q_{\text{zpf}}^2} S_{qq}^{(d)}.$$

(3.12)

To match our definition of heating rates we introduced a factor of two w.r.t the definitions in [103]. For the experiments presented in this chapter, the requirements for the approximations of Eq. (3.11) are not fulfilled as $|g_y| < \Omega_y < \kappa/2$. We will be able to use the approximative expressions after modifications to the setup which we will discuss in the next chapter. At this point, we describe the measured c.m. temperatures with Eqs. (2.4) and (3.10) and find indeed non-vanishing values for the trap displacement noise $\Gamma_{x,y,z}^{(d)} = 2\pi \times \{84\,\text{kHz}, 15\,\text{kHz}, 21.5\,\text{MHz}\}$ [103]. The impact of trap displacement noise is similar along x and y, but significantly stronger for the z motion. We explain the difference by the position of the particle during the cooling experiments. The minimal c.m. temperatures for the motion along the x and y direction are found for a particle in the node. In order to cool the motion in the z direction, on the other hand, the particle is placed at the antinode, where the population of the cavity field is maximal. We expect any fluctuating forces on the particle, which scale with the intensity of the cavity mode, to be more relevant at the antinode. Hence the cooling along the z direction would be affected more strongly. We believe laser phase noise, which translates into trap displacement noise, to be the origin of this effect. We will briefly explain how these two effects are connected in the next section and have a more thorough discussion on heating effects in Sec. 4.1.

3.5.1 *Cavity Input-Output Formalism with a Pumped Particle*

In this section we apply the formalism from Sec. 2.3.1 but instead of injecting a laser into the cavity through a mirror [127], we coherently scatter light into the cavity via a trapped particle. Since the particle radius in our experiments is smaller than the wavelength we assume a dipolar scatterer. The analogous calculation was conducted in [123, 142] to describe the coherent scattering of an atom into a cavity. We can therefore rely on their results by substituting the polarizability of an atom by that of a particle. The polarizability of a dipole in vacuum is given by [114, 118]

$$\alpha_{dp} = \epsilon\epsilon_0 V_p \tag{3.13}$$

$$\epsilon := 3\frac{\epsilon_p - 1}{\epsilon_p + 2}.$$

The dielectric constant of silica at a laser wavelength $\lambda = 1550\,\text{nm}$ is approximately $\epsilon_p = 2.07$ [136]. We note here, that $\text{Im}\,\epsilon_p = 0$ as the intrinsic losses of silica at the laser wavelength are negligible compared to the radiative correction. The effective polarizability to account for radiative losses is then [114, 118]

$$\alpha = \frac{\alpha_{dp}}{1 - i\frac{k^3}{6\pi\epsilon_0}\alpha_{dp}} \approx \alpha_{dp} + i\frac{k^3}{6\pi\epsilon_0}\alpha_{dp}^2. \tag{3.14}$$

We consider an input field E_{tw} scattering from a dipole. The dipole is placed inside an optical cavity and some of the scattered light couples into a TEM$_{00}$ mode of the cavity. The scattered field coupled into the cavity mode E_S is given by [123]

$$E_S = i\beta E_{tw} \tag{3.15}$$

$$\beta = \frac{k}{\pi w_c^2}\frac{\alpha}{\epsilon_0}. \tag{3.16}$$

The factor β accounts for the mode overlap of the dipole field with the cavity mode of waist w_c. To derive the expression, one has to assume the distance of the mirrors to the particle to be much larger than the wavelength of the input field and use the far-field approximation of the dipole field. We furthermore assume that the optical tweezer is polarized along the x direction, transversal to the cavity axis y. Thereby, the dipole scatters maximally into the cavity. We are now able to define a set of steady-state fields (E_1 and E_2) that build up inside the cavity and leak through the mirrors, as shown in Fig. 3.5. Both E_1 and E_2 are defined at the particle position, propagating in opposite directions. The particle is centered along the x, as well as z axes and placed at y_0 along the cavity of length L. As in Sec. 2.3.1 the field reflection and transmission coefficients are denoted by r_A and t_A (r_B and t_B) for mirror A (B). We formulate a set of self-consistent equations

$$E_1 = E_S + r_A E_2 e^{ik_{tw}(L+2y_0)}$$
$$E_2 = E_S + r_B E_1 e^{ik_{tw}(L-2y_0)}$$
$$E_A = it_A E_2 e^{ik_{tw}(L/2+y_0)} \qquad (3.17)$$
$$E_B = it_B E_1 e^{ik_{tw}(L/2-y_0)}$$
$$E_S = i\beta(E_{tw} + E_1 + E_2).$$

The first two equations incorporate the phase relation between right (E_1) and left (E_2) circulating fields and the scattered light. The third and fourth lines express the fields leaking through the cavity mirrors by propagating the circulating fields. The last equation takes into account that the particle not only scatters the input field from the tweezer, but also light from the cavity mode. The cavity field E_c is then given by the superposition of the two counter-propagating fields,

$$E_c = E_1 e^{ik_{tw}y_c} + E_2 e^{-ik_{tw}y_c} \qquad (3.18)$$

where y_c denotes a position inside the cavity relative to the particle position. We solve the set of equations (Eq. (3.17)) to find expressions for the counter-propagating intra-cavity fields. The fields leaking through the mirrors can be easily obtained by multiplying with the appropriate factors. The solutions are given by

$$E_1 = -i\beta F E_{tw} \left[r_A e^{ik_{tw}(L+2y_0)} + 1 \right] \qquad (3.19)$$
$$E_2 = -i\beta F E_{tw} \left[r_B e^{ik_{tw}(L-2y_0)} + 1 \right] \qquad (3.20)$$

with a dimensionless complex transfer function,

$$F = \left\{ i\beta \left[r_A e^{ik_{tw}(L+2y_0)} + r_B e^{ik_{tw}(L-2y_0)} + 2 \right] + r_A r_B e^{2ik_{tw}L} - 1 \right\}^{-1}. \qquad (3.21)$$

We apply the formalism and initially focus on the field leaking through mirror B. We previously claimed that we can relate the power leaking through mirror B to the particle position relative to the cavity intensity profile. To legitimize this we investigate $I_B \propto |E_B|^2$ and $I_c \propto |E_c|^2$ in Fig. 3.6. (a) The normalized intensity behind one of the mirrors as a function of particle position is shown. We focus on three distinct positions with a
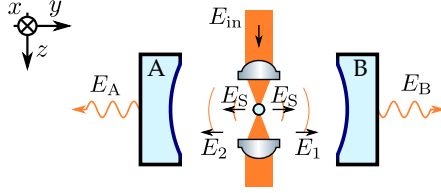
FIGURE 3.5: *Input-Output formalism of a particle coherently scattering into an optical cavity.* A laser field E_{tw} is scattered from a levitated particle into the cavity. The scattered light populates a cavity mode and in turn scatters from the particle. The total scattered field is then given by E_S. We define the steady-state right traveling field at the particle position as E_1 and the left traveling field as E_2. The fields leaking out of the cavity through mirror A (B) is denoted by E_A (E_B). The particle is located in the center of the cavity mode along x and z directions and at position y_0 relative to the middle between the two mirrors.

particle placed at the intensity maximum (▼), the steep slope (♦) and close to the minimum (●). For each of the three positions we calculate the cavity intensity profile in the vicinity of the particle. We normalize the cavity intensity by the intensity leaking through mirror B and show the results in (b). We conclude that indeed the power leaking through the mirror is a good indicator for the particle position relative to the intensity profile. In Sec. 4.2 we will measure the drift of the trap center relative to the cavity. To accurately relate detector signal and particle position we derive an expression for the intensity measured behind mirror B. We observe that the intensity on the cavity detector not only depends on particle position, but also detuning. As we try to enhance anti-Stokes scattering in our experiment the cavity frequency is detuned by $\Delta = \omega_c - \omega_{tw} \approx \Omega_y \ll \omega_{fsr}$. For detunings small compared to the free spectral range and silica particles of typical experimental size we find by combining Eqs. (3.17), (3.19) and (3.21),

$$\frac{|E_B|^2}{|E_{tw}|^2} \approx \frac{|\beta|^2 \mathcal{T}_B \omega_{fsr}^2}{4\pi^2 \mathcal{R}_{AB}} \frac{1 + r_A^2 \pm 2r_A \cos(2k_{tw}y_0)}{\Delta^2 + (\kappa/2)^2}. \tag{3.22}$$

If the cavity length is chosen such that there is a field maximum (minimum) in the cavity center the $+$ $(-)$ sign has to be chosen. The intensity transmission coefficient of mirror B is denoted by $\mathcal{T}_B = t_B^2$. The average intensity reflection coefficient of both mirrors is $\mathcal{R}_{AB} = r_A r_B$. Furthermore, the cavity linewidth is denoted by κ, the detuning by Δ and the free spectral range by ω_{fsr}.
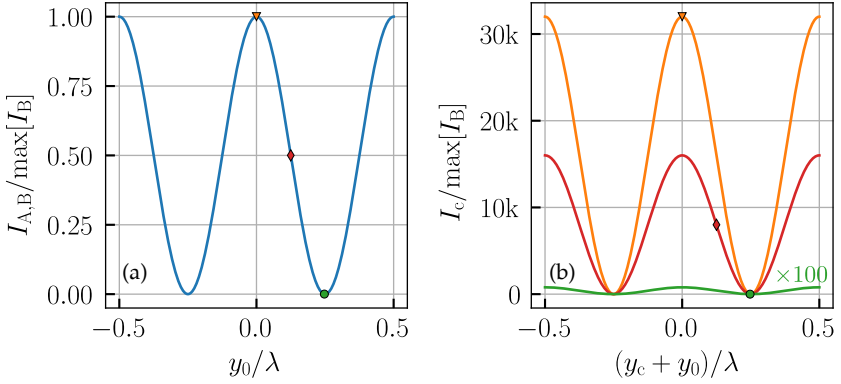
FIGURE 3.6: *Circulating cavity and output intensity for pumping by coherent scattering.* The cavity parameters are as discussed in Sec. 3.1 and presented in Tab. 2.2 for generation 1. The data is obtained for an input power of $P_{tw} = 500$ mW and a particle radius $R = 70$ nm. (a) We show the relative intensity leaking through mirrors A and B. As the transmission and reflection coefficients are the same for both mirrors the transmitted intensity is fully symmetric. The output intensity is maximal for $y_0 = 0$ and minimal at $y_0 = \lambda/4$, with a periodicity of $\lambda/2$. (b) We choose three values for y_0 as indicated in (a) by colored markers at the intensity maximum (▼), the steep slope (♦) and close to the minimum (●) for numeric reasons ($y_0 = 0.99\lambda/4$). We plot the intensity profile in the vicinity of the particle for each case. For the particle positioned in the intensity maximum the amplification of the field w.r.t. to the field leaking out of the cavity is on the order of the cavity finesse $\mathcal{F} \approx 22k$. For the particle positioned close to the intensity minimum we multiply the curve with a scaling factor of 100 to improve visibility.

We continue by investigating the force on the levitated particle at a fixed position inside the cavity. We will use this to gain intuition on how trap displacement noise may arise and influence our cooling results in the previous sections. A dielectric particle in an optical field $\mathbf{E}$ experiences a time averaged optical force $\langle \mathbf{F}_{opt} \rangle$ [114, 118]

$$\langle \mathbf{F}_{opt}(\mathbf{R}) \rangle = \frac{\mathrm{Re}\,\alpha}{2} \sum_{i \in \{x,y,z\}} \mathrm{Re}(E_i^* \nabla E_i) + \frac{\mathrm{Im}\,\alpha}{2} \sum_{i \in \{x,y,z\}} \mathrm{Im}(E_i^* \nabla E_i). \quad (3.23)$$

The total optical force acting on the particle is given by the sum of the tweezer and cavity field. We define the center of the cavity in y direction

as the origin of our reference frame. The focus of the optical tweezer is located at y_{tw} and the particle is at position $y_0 = y_{tw} + y$. We previously defined E_c as the cavity field at y_c relative to a particle at position y_0. The strongly focused optical tweezer is formally described by an Airy disk, consisting of a strong central lobe and outer rings [118]. However, in typical cooling experiments the particle does not experience regions of the optical tweezer more than 100 nm away from the focus, but rather stays in the center of the strong central lobe. To gain a qualitative understanding of the particle-cavity interaction, it is therefore feasible to write the x polarized optical tweezer in Gaussian approximation as [114]

$$\boldsymbol{E}_{tw} = E_0 \exp \left[-\frac{(y_0 - y_{tw} + y_c)^2}{w_y^2} \right] \boldsymbol{n}_x, \qquad (3.24)$$

with $E_0 = \sqrt{4P_{tw}/(c\epsilon_0 \pi w_x w_y)}$ for beam waists $w_x \approx w_y \approx 1\,\mu m$. The cavity field is x polarized like the optical tweezer and has a Gaussian transversal profile with waist $w_c = 48\,\mu m$, resulting in a total field

$$\boldsymbol{E} = \boldsymbol{E}_{tw} + E_c \exp \left(-\frac{x_0^2 + z_0^2}{w_c^2} \right) \boldsymbol{n}_x \qquad (3.25)$$

As the particle is centered w.r.t. to the cavity transversal profile with a negligible movement relative to the large beam waist we can assume $x_0 = z_0 = 0$, to focus on the motion along the y axis. We write for the y component of the force at the particle position

$$\langle F_{opt} \rangle (y_0) = \frac{\mathrm{Re}\,\alpha}{2} \mathrm{Re} \left[E_x^* \frac{\partial E_x}{\partial y_c} \right]_{y_c=0} + \frac{\mathrm{Im}\,\alpha}{2} \mathrm{Im} \left[E_x^* \frac{\partial E_x}{\partial y_c} \right]_{y_c=0} \qquad (3.26)$$

The first term is often referred to as the gradient force $\langle F_{grad} \rangle$ whereas the second one is denoted by scattering force $\langle F_{scat} \rangle$ [118]. In our system the scattering force along the cavity axis is orders of magnitude smaller than the gradient force. We therefore neglect it and show the gradient force for different particle positions and first generation cavity and trapping lens parameters in Fig. 3.7. We overlay the gradient force exerted from the bare tweezer on the total gradient force to compare the difference. For a tweezer focus at the cavity field antinode, as shown in (a), we observe a slightly steeper slope for the blue curve at $y = 0$. As the total field intensity at the
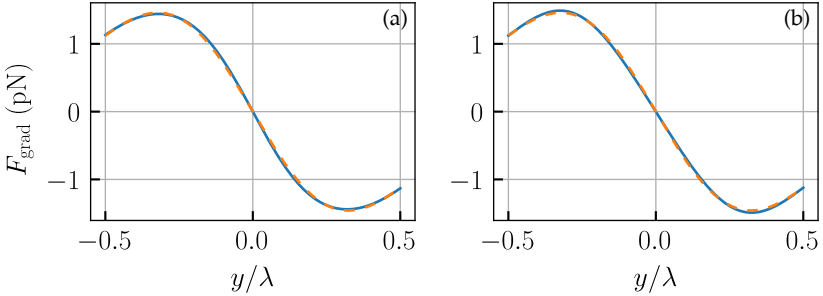
FIGURE 3.7: *Gradient force on a dielectric particle in a cavity tweezer field.* The experimental parameters are as in Fig. 3.6. The solid blue lines correspond to the total force exerted on the particle while the dashed orange lines denote force of a bare tweezer without a cavity field, for reference. We show the gradient force acting on the particle, as a function of position relative to the center of the tweezer trap. In (a) we place the trap center at the cavity antinode, whereas in (b) the trap center is placed at the cavity node.

antinode is higher than the tweezer intensity alone, the trap stiffens. This effect is referred to as optical spring effect [31, 150, 151]. In (b) we place the trap center at the cavity node and observe the opposite result. Instead of steepening the slope, the cavity makes the curve slightly flatter. In our experiments we observe this effect through higher trapping frequencies for a particle at the cavity antinode than at the cavity node.

We conclude from this discussion, that a particle, placed at different points along the cavity intensity wave, experiences additional optical forces. These forces affect the spring constant of the optical trap and thereby may resonantly or parametrically drive the particle motion [152]. Resonant and parametric driving of the particle motion require intensity or trap displacement noise at frequencies around the particle frequencies. [114, 152]. In Sec. 4.2 we analyze the mechanical stability of the optical tweezer and observe only vibrations below $\Omega_m = 2\pi \times 1\,\text{kHz}$. In Sec. 2.3.1 we explained that laser frequency or phase noise results in a displacement of the cavity intensity profile. As the mechanical vibration is too slow to directly affect the particle motion, we believe that the trap displacement noise in our experiments stems from laser phase noise. The mechanical vibration, however, limits our ability to place the particle close to the cavity node, which in turn affects how strongly the elastic scattering into the cavity

can be suppressed. Laser intensity fluctuations cannot explain the heating rates in our measurements. Indeed, RIN could parametrically drive the particle motion, but the main drive would stem from the intense tweezer field alone. Hence the heating effect would be visible in our reheating measurements in Sec. 3.3.

We used a steady-state formalism, as it gives an intuitive idea of both the optical spring effect and the light fields that build up inside the cavity. It is helpful, to understand the consequences of slow drifts of the trap position inside the cavity, but we have to be careful, if we want to consider effects around the particle oscillation frequency. The cavity field is built up from light scattered by the particle, which in turn depends on the particle position. As the cavity field is not created instantaneously, our static model cannot account for fast dynamical effects. We need to consider the Hamiltonian in Eq. (3.1) or investigate a dynamical model to explain the process of particle cooling. We outline here how laser phase noise can induce trap displacement noise in a static picture, but believe a detailed analysis, that links the two in a dynamical model would be valuable. In Sec. 4.1 we will use phase noise heating rates from the literature [69, 153, 154] to motivate upgrades to our setup.

4

TOWARDS GROUND-STATE COOLING OF A LEVITATED PARTICLE

In Chapter 3 we discussed our cavity-based coherent scattering cooling experiments in a regime where the particle c.m. temperature was still limited by kicks from the surrounding gas molecules, but an additional noise of the system started playing a role. Based on our measurements we expect to reach lower phonon numbers with an improved vacuum system, but will be limited by the additional noise before cooling to quantum ground-state. Additionally, the lowest c.m. temperature[1] that we were able to measure was close to the signal-to-noise limit of our free space detector. As the stability of the setup does not permit to measure for sufficiently long, to overcome the signal-to-noise limit, we need to enhance the detection efficiency. Since we were limited both in cooling and detection of the c.m. motion we decided to analyze how to effectively upgrade the system, based on the theory in [103] and the experiences we collected during the initial measurements.

To enhance the detection efficiency, recent free space ground-state cooling experiments [72, 73] focused on cooling the motion along the tweezer axis (z). With a detection setup in backreflection they were able to benefit from the asymmetric information distribution in the scattered light field [71]. To cool the motion along z in our experiment is not feasible, as it requires to position the particle in the cavity antinode. A particle at the antinode strongly populates the cavity with scattered light and limits the minimal phonon number more severely than for a particle in the cavity node, as discussed in Sec. 3.2. At the node on the other hand, we are only able to cool the motion along the cavity axis (y). The solution to overcome the detection limit is to use the optical cavity not only as a cooling system, but also as a detection tool as mentioned in Sec. 2.4.3.

It seems convenient to use the optical cavity both for c.m. motion cooling and detection, but it also complicates the discussion of the right cavity parameters. We are not allowed to find the right parameters for cavity cooling and cavity detection independently, but have to find compromises. The strategy in our discussion will be to first determine a parameter range

---

1 $T_y \approx 3\,\mathrm{mK}$, which corresponds to $\overline{n}_y \approx 450$

in which ground-state cooling is possible, within experimentally realistic boundary conditions. Only after that we analyze which parameters within this parameter range also enable efficient detection. Based on the discussion we motivate the choice for our second generation trapping lens (Tab. 2.1) and cavity mirrors (Tab. 2.2).

After finding a suitable parameter range we continue to describe the remaining limitations of our upgraded setup, namely the mechanical stability of the trap center and noise sources in the heterodyne detection. Thereafter we describe sideband-thermometry in combination with a cavity enhanced detection. We apply the technique in measurements with our most recent cavity configuration and present the minimal average phonon number on the order of $\overline{n}_y \approx 10$. Finally, we conclude the chapter by describing additional upgrades that can bring the setup into the quantum ground-state.

4.1   REQUIREMENTS FOR GROUND-STATE COOLING

In this section we present a favorable parameter regime for optical tweezer and cavity while not sacrificing detection efficiency. The analysis is based on the theory developed in collaboration with Gonzalez-Ballestero et al. [103]. Before starting a quantitative analysis we qualitatively explain the influence of the most important parameters.

Mechanical Frequency—Ground-state cooling benefits from a high frequency of the mechanical oscillator, in our case the c.m. motion along the cavity axis at frequency Ω_y. A high mechanical frequency leads to a reduction of the thermal phonon number as $\overline{n}_y \approx k_B T_{cm}/\hbar\Omega_y$. Since the particle is susceptible to noise (mechanical, acoustic or also $1/f$) around its motional frequency it is easier to isolate it from the environment at higher frequencies. Furthermore, laser phase noise is lower at higher frequencies as seen in Sec. 4.3, reducing the excess heating and facilitating data analysis. Additionally, a higher frequency technically facilitates entering the resolved-sideband regime, since we can allow for a larger cavity linewidth κ and thus cavity mirrors with a lower reflectivity. Current high finesse mirror coatings achieve high reflectivity by reducing transmission, but offer only a minimal intensity absorption value of about 1 ppm. Using mirrors with lower reflectivity therefore benefits the detection efficiency, as more photons are transmitted than absorbed. The mechanical frequency scales with experimental parameters as [114]

$$\Omega_y \propto \sqrt{\frac{\epsilon_{\mathrm{p}} - 1}{\rho(\epsilon_{\mathrm{p}} + 2)}} \frac{\sqrt{P_{\mathrm{tw}}}}{w_{\mathrm{tw}}^2}. \tag{4.1}$$

The first factor in Eq. (4.1) depends on material properties like the dielectric function ϵ_{p} and density ρ of the particle (in our case silica), but not the particle size. Indeed, other materials than silica have been levitated optically i.e. nanodiamonds [155, 156] or ytterbia [91] and even strongly absorbing particles made from metal or dye-impregnated glycerol [157–159]. However, none of them have been brought into high vacuum (below a few mbar). The exact loss mechanism in the case of nanodiamonds is under debate. It is not clear if the particle burns and evaporates or if it is lost through Brownian motion due to an increased internal temperature. In either case, the problem originates from the absorption of laser power and lack of surrounding gas particles to equilibrate the internal temperature to the environment. Until more suitable materials for optical trapping than silica are found, we can increase the frequency either by increasing the power $\propto \sqrt{P_{\mathrm{tw}}}$ or tighter focusing $\propto w_{\mathrm{tw}}^{-2}$. We achieve the latter by switching to our second generation lens (Tab. 2.1). An increase in trap power on the other hand is only possible by switching from a fiber coupled tweezer to a free space setup. In general changing optical power not only affects the mechanical frequency, but also optomechanical coupling and phase noise heating, as discussed below and has to be done cautiously.

Cavity Linewidth—The cavity linewidth κ has to be considered particularly carefully to achieve the right trade-off between an efficient particle read-out with a large linewidth and efficient sideband-resolved cooling with a narrow linewidth. To cool the particle motion we blue detune the cavity from the tweezer with $\Delta \approx \Omega_y$, to the anti-Stokes sideband. All light scattered from the particle is then filtered by the cavity transfer function, a Lorentzian centered at Δ with FWHM κ. On one hand, sideband-thermometry requires the detection of the suppressed Stokes scattered light and not only the enhanced anti-Stokes scattering as we explained in Sec. 2.4.3. On the other hand, we can suppress Rayleigh scattering while enhancing anti-Stokes scattering with a narrow cavity linewidth. We could add a weaker measurement laser to probe Stokes and anti-Stokes scattering separately one or two free spectral ranges away from the optical tweezer, increasing technical complexity and potentially adding heating mechanisms. Instead, we choose a linewidth that is just wide enough to resolve both Stokes and anti-Stokes scattering, but also narrow enough to achieve low

occupation numbers. In practice, technical restrictions also set boundaries for the cavity linewidth $\kappa \propto (1 - \mathcal{R}_{AB})/L$ (see Eq. (2.25)). For our second generation cavity we obtained mirrors with a combined reflectivity $\mathcal{R}_{AB} = \sqrt{\mathcal{R}_A \mathcal{R}_B} \approx 99.9892\%$. To minimize cavity mode volume and in turn increase optomechanical coupling strength g, we choose the mirrors with smallest radius of curvature commercially available (ROC = 10 mm). The cavity stability condition limits the cavity length at $L < 20$ mm, corresponding to the lowest possible linewidth $\kappa_{\min} = 2\pi \times 135$ kHz. On the other extreme, the shortest cavity we can build, with enough space to position an optical tweezer inside is $L > 6$ mm. The maximal achievable linewidth is therefore $\kappa_{\max} = 2\pi \times 429$ kHz.

Optomechanical Coupling—The final parameter that determines cooling performance is the coupling between the mechanical modes of the trapped particle and the optical cavity mode. The coupling for all three oscillators is given in Eq. (3.3). Since we focus on ground-state cooling the motion along the cavity axis (y), we define $g := G k_c y_{zpf}/2$ and insert all definitions from Sec. 3.2 to analyze the influence of experimental parameters,

$$g = \pi^{5/4} \sqrt{\frac{1}{\lambda^3} \sqrt{\frac{\epsilon^3 c}{\rho}}} \times \sqrt[4]{P_{tw} \frac{\Omega_x}{\Omega_y}} \times \sqrt{\frac{V}{V_c}}. \tag{4.2}$$

We define ϵ in Eq. (3.13) as a parameter depending only on the dielectric function of silica, at the trapping wavelength. We assume that material parameters (ϵ, ρ) are fixed and observe that the dependence on trapping power is only very weak. The remaining tuning parameters are laser wavelength and particle volume relative to cavity mode volume. To increase g it would be beneficial to choose a shorter wavelength for our experiments than $\lambda = 1550$ nm. But the disadvantage is compensated by highly efficient optical components, optical coatings, low phase noise lasers[2] and a larger distance between cavity node and antinode ($\lambda/2$) making the particle positioning less critical. The largest particles trapped in our group have a radius of approximately $R \approx 200$ nm [83] and the smallest mode volume is obtained close to the minimal cavity length $L \approx 6$ mm. Assuming a tweezer power of $P_{tw} = 500$ mW and particles made from silica, we calculate the maximal optomechanical coupling strength of $g_{\max} \approx 2\pi \times 249$ kHz. At the other extreme, we can trap the smallest commercially available silica particles which are on the order of $R \approx 50$ nm and set the cavity length to $L = 15$ mm and obtain $g_{\min} \approx 2\pi \times 20$ kHz.

In general the dependence of minimal phonon number on g is complicated, as shown in Eq. (3.10). However, for $g \ll \kappa/2 \ll \Omega_y$ we find a cavity cooling rate of $\gamma_y^{(c)} = 4g^2/\kappa$ according to Eq. (3.11). In Fig. 4.1 we analyze the validity of the approximation close to ground state for our parameter regime. To do so, we set the heating rate to $\Gamma_y = 2\pi \times 50\,\mathrm{kHz}$, which is low enough to reach ground-state in our parameter regime and discuss
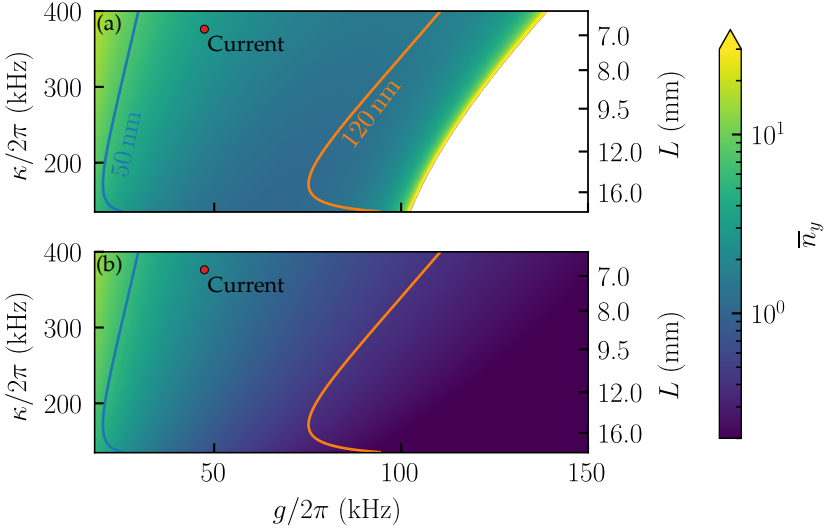

FIGURE 4.1: *Phonon occupations in our experimental parameter regime.* We compare the achievable phonon occupations for the motion along the y direction in the parameter regime discussed in this section, for a heating rate of $\Gamma_y = 2\pi \times 50\,\mathrm{kHz}$. (a) The phonon occupation according to the full model of Eq. (3.10) is shown for possible cavity linewidths and optomechanical couplings for our second generation trapping lens and cavity. The mechanical frequency is $\Omega_y = 2\pi \times 193\,\mathrm{kHz}$ and we choose a cavity detuning $\Delta = \Omega_y$. By changing particle size and cavity length we can explore different regions of the parameter regime as indicated by the curves for radii $R = \{50, 120\}\,\mathrm{nm}$. For $g \approx 2\pi \times 120\,\mathrm{kHz}$ the system becomes unstable. (b) We show the phonon occupation for the same parameters as in (a) but using the approximative formula for the case of $|g_y| \ll \kappa/2 \ll \Omega_y$ from Eq. (3.11). In particular in the regime of $g < 2\pi \times 60\,\mathrm{kHz}$, the two formulas show a good agreement. The red dot shows our current configuration in the lab for particles of radius $R = 70\,\mathrm{nm}$.

below which heating rates are actually experimentally realistic. We want to see here, how well the more general formula of Eq. (3.10) agrees with the approximation $\bar{n}_y = \Gamma_y \kappa / 4g^2$ from Eq. (3.11). Both figures show the minimum phonon number for different combinations of optomechanical coupling rate and cavity linewidth. We add a blue and orange curve to show which particle radius enables us to explore a certain parameter regime. The red dot denotes the parameters of the second generation cavity when cooling silica particles of radius $R = 70\,\mathrm{nm}$, our latest experimental configuration. Especially for moderately large coupling rates $g < 2\pi \times 60\,\mathrm{kHz}$ the approximative cavity cooling rate is justified. Therefore, increasing the optomechanical coupling rate is a viable strategy to decrease the minimal phonon number. However, at a certain threshold the system becomes dynamically unstable indicated by a white area in Fig. 4.1(a) and phonon numbers increase prior to that. Disregarding any excess heating effect, one would suggest that a particle radius of $R = 120\,\mathrm{nm}$ would be ideal and ground-state could be reached for a heating rate $\Gamma_y < 2\pi \times 0.1\,\mathrm{MHz}$, corresponding to a residual gas heating at a pressure of $p \approx 2 \times 10^{-6}\,\mathrm{mbar}$.

Heating Mechanisms—So far we have discussed the figures of merit to improve cooling rates. As the final phonon occupation is reached by the competition of heating and cooling effects we cannot focus on optimizing only one of the two and neglecting the negative implications of the other. In free space experiments with levitated particles a variety of effects have been investigated that could potentially increase the particle's c.m. temperature. Among them are heating due to RIN, trap displacement noise and photon shot noise [51, 160]. For typical experimental parameters all of these effects are masked by residual gas heating until pressures of $< 10^{-8}\,\mathrm{mbar}$ are reached. However, in context of particle trapping with optical cavities it was reported, that laser phase noise limits cooling performance already at pressures on the order of $\approx 10^{-6}\,\mathrm{mbar}$ suggesting that this effect is dominant over other technical limitations [63]. In Fig. 2.7 we showed that laser frequency or phase noise shifts the cavity intensity profile relative to the optical tweezer (displacement noise). The fluctuating optical force on the particle depends on the cavity population, which we can reduce by positioning the particle at the cavity node and thereby suppressing elastic scattering into the cavity. Therefore, phase noise heating is reduced, but not entirely eliminated, due to thermal drifts of the mechanics moving the particle away from the cavity node [69]. We extract the recoil heating rate $\Gamma_q^{(\mathrm{r})}$ [103], RIN heating rate $\Gamma_q^{(\mathrm{RIN})}$ [51] and phase noise heating rate $\Gamma_q^{(\mathrm{PN})}$ [69] from the literature and match them with our definitions,

$$\Gamma_q^{(r)} = \frac{\pi\epsilon_0}{15\hbar}\left(\frac{\epsilon V E_0}{2\pi}\right)^2 k^5 q_{\mathrm{zpf}}^2 N_q, \quad N_{x,y,z} = \{1,2,7\} \tag{4.3}$$

$$\Gamma_q^{(\mathrm{RIN})} = \pi\Omega_q^2 S_{RR}\bar{n}_q \tag{4.4}$$

$$\Gamma_q^{(\mathrm{PN})} = \frac{G^2\cos^2(\phi)|g_q|^2}{\kappa^2\left[\left(\frac{\kappa}{2}\right)^2 + \Delta^2\right]}S_{ff}. \tag{4.5}$$

The laser relative intensity and frequency noise are given by S_{RR} and S_{ff} respectively. The other parameters are the dielectric function ϵ_0, the particle volume V, the wave number of the field impinging on the particle k, the zero point fluctuation q_{zpf} of oscillator $q \in \{x,y,z\}$, the cavity linewidth κ and detuning Δ, as well as the particle position relative to the intensity maximum ϕ. The parameters ϵ and G are defined in Eq. (3.13) and below Eq. (3.3), respectively.

Since our particle is subject to both the tweezer field and the cavity field, in principle we need to the take the recoil and RIN heating rates from both fields into account. However, we are primarily interested in the heating effects close to the cavity node. There the peak intensity at the particle position is dominated by the optical tweezer, since the tweezer is more than an order of magnitude more strongly focused than the cavity field. We also want to point out that the heating due to RIN depends on the phonon occupation number as it is a parametric effect and therefore also becomes negligible when approaching the ground-state.

In [69, 153, 154] the heating effect that arises from phase noise is denoted by an excess average phonon number[3]. To compare the different heating effects with each other it is more convenient for us to convert this into a heating rate. We have shown above, that in our cavity parameter regime the average phonon number is well approximated by $\bar{n}_y = \Gamma_y\kappa/4g^2$ and thereby we can define a heating rate through $\Gamma_y := 4\bar{n}_y g^2/\kappa$. Inserting the expression from [69, 153, 154] into this definition we obtain Eq. (4.5).

In Sec. 4.2 we will discuss the mechanical stability of the optical trap relative to the cavity in detail. To already take into account, that the optical tweezer moves w.r.t. the cavity intensity profile at $\Omega_\mathrm{m} < 200\,\mathrm{Hz}$, we write the trap center position as $y_0 = y_\mathrm{m}\sin(\Omega_\mathrm{m}t)$. Since both the cooling and the heating rates, as well as the particle oscillation frequencies are orders

---

3 The phase noise phonon occupation seems to give reasonable heating contributions for similar experiments. As discussed in Sec. 3.5.1 phase noise has a few effects on the particle motion and a thorough analysis of the exact manifestation would be valuable.
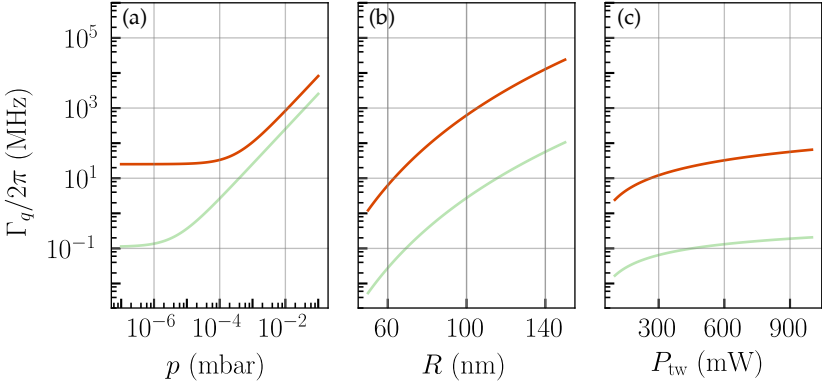
FIGURE 4.2: *Phase noise heating for different trapping parameters.* We assume the second generation cavity parameters, laser phase noise of $S_{ff} = 2\pi \times 0.8\,\mathrm{Hz}^2/\mathrm{Hz}$ as specified by the manufacturer and a thermal tweezer motion relative to the cavity intensity profile of amplitude $y_m = 50\,\mathrm{nm}$. In all figures the green (red) curve denotes heating rates for the motion along y (z) and a particle positioned at the node (antinode). (a) The total heating rate is shown. The dominant contribution is from residual gas scattering at high pressures until phase noise becomes dominant at a pressure of $10^{-3}\,\mathrm{mbar}$ in the antinode and $10^{-5}\,\mathrm{mbar}$ at the node. We assume a particle size of $R = 70\,\mathrm{nm}$ and trapping power of $P_{tw} = 500\,\mathrm{mW}$. (b) We show the phase noise heating rate for a fixed trapping power $P_{tw} = 500\,\mathrm{mW}$ for different particle radii R. (c) The phase noise heating rate is plotted for a fixed particle radius $R = 70\,\mathrm{nm}$ and varying trapping power P_{tw}.

of magnitude higher then the mechanical motion of the trap, it might seem feasible to let the particle slowly drift through the cavity node and focus on a time window where the particle is close enough to it and phase noise becomes negligible. Unfortunately, the detection scheme requires us to record data for much longer than $1/\Omega_m$ to overcome detection noise. We therefore define $\phi_{an} = k_{tw}y_0$ for a particle at the antinode and $\phi_n = \phi_{an} + \pi/2$ for a particle at the node. By integrating Eq. (4.5) over t we can calculate the average heating rate. As there is no compact analytical result for the integration we approximate the average heating rate by inserting the time averaged phonon number and time averaged optomechanical coupling rate. To test the validity of this approach we integrate Eq. (4.5) numerically and find no significant deviation from the approximations in Eq. (4.6) for our parameter regime. We therefore write for the phase noise heating rates

$$\Gamma_y^{(PN)}(\phi_n) \approx \frac{G^4(k_{tw}y_m)^2\{k_{tw}y_{zpf}[1-(k_{tw}y_m)^2/4]\}^2}{8\kappa^2\left[\left(\frac{\kappa}{2}\right)^2+\Delta^2\right]}S_{ff}$$

$$\Gamma_z^{(PN)}(\phi_{an}) \approx \frac{G^4[1-(k_{tw}y_m)^2/2]\{k_{tw}z_{zpf}[1-(k_{tw}y_m)^2/4]\}^2}{4\kappa^2\left[\left(\frac{\kappa}{2}\right)^2+\Delta^2\right]}S_{ff}.$$

(4.6)

In Fig. 4.2 we visualize the results from Eqs. (4.3), (4.4) and (4.6). For typical experimental parameters $P_{tw} = 500\,\text{mW}$ and $R = 70\,\text{nm}$, the influence of photon recoil $\Gamma_{y,z}^{(r)} \approx 2\pi \times \{0.7, 7.4\}\,\text{kHz}$ and RIN $\Gamma_{y,z}^{(RIN)} \approx 2\pi \times \{0.2, 0.02\}\,\text{kHz}$ are negligible. To calculate $\Gamma_{y,z}^{(RIN)}$ we assume a phonon occupation of $\overline{n}_q = 1000$ and $S_{RR} = -125\,\text{dB/Hz}$ as specified by the manufacturer[4]. As previously mentioned, we require pressures of $p < 10^{-6}\,\text{mbar}$ for ground-state cooling. In Fig. 4.2(a) we observe that the heating is dominated by phase noise below $10^{-3}\,\text{mbar}$ along the z axis and $10^{-5}\,\text{mbar}$ along the y axis preventing ground-state cooling in this regime. The phase noise heating contribution is calculated assuming $S_{ff} = 2\pi \times 0.8\,\text{Hz}^2/\text{Hz}$ as specified by *NKT Photonics* and $y_m = 50\,\text{nm}$. To reduce the influence of phase noise we can decrease the particle size or reduce trapping power, as shown in Fig. 4.2(b, c) at the cost of also lowering the cooling rates. To lower phase noise heating without any negative effects on the cooling rate we need to reduce the noise figure of the trapping laser by using a filter cavity [69] or improve the mechanical stability of the optical tweezer w.r.t. the cavity.

4.1.1   *Optimal parameters for Ground-State Cooling*

In the previous section we have discussed which figures of merit have to be considered to increase the cooling rates of our system or lower the heating rates. Some have clear implications like choosing the right trapping lens and cavity mirrors which we have implemented by switching to a second lens and cavity generation. Other implications, like improving the mechanical stability of the system are more challenging to implement and are discussed in Sec. 4.2. Here we focus on finding the minimal phonon occupation for our system by tuning parameters that do not have a clear negative or positive effect, as they are e.g. increasing cooling and heating rates at the same time. Those parameters are the particle radius R, cavity
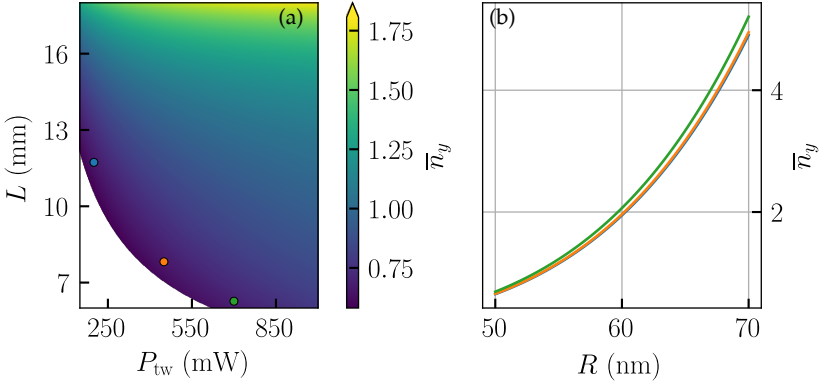
---

4 *NKT Koheras ADJUSTIK E15*

FIGURE 4.3: *Minimal phonon numbers for experimental parameters.* The results of both figures are obtained through Eq. (4.7) and assuming $\Gamma_q^{(P)} < \Gamma_q^{(PN)}$, as well as $S_{ff} = 2\pi \times 0.8\,\text{Hz}^2/\text{Hz}$ and $y_m = 50\,\text{nm}$. (a) The minimal phonon number is shown as a function of trapping power P_{tw} and cavity length L for a particle radius $R = 50\,\text{nm}$. The lowest phonon number is obtained close to the masked area in the bottom left which violates the resolved sideband criterion $\Omega_y > \kappa/2$. Towards the top right cooling becomes less efficient. (b) To show the relevance of the particle size we choose three combinations of cavity length and trap power marked in (a) by colored markers and plot the minimal phonon number against the particle radius $((L, P_{tw}) = \{(11\,\text{mm}, 200\,\text{mW}), (7.8\,\text{mm}, 450\,\text{mW}), (6.3\,\text{mm}, 700\,\text{mW})\})$. The cooling performance depends strongly on particle size but there is no significant difference between choosing a long cavity and low trap power or a short cavity and high trap power.

length L and trapping power P_{tw}. Combining Eqs. (3.11) and (4.6) under the condition $|g_q| \ll \kappa/2 \ll \Omega_q$ and assuming that the gas pressure is sufficiently low $\Gamma_q^{(P)} < \Gamma_q^{(PN)}$, we derive the phonon occupation limited by phase noise heating,

$$\bar{n}_y = \frac{G^2 (k_{tw} y_m)^2 S_{ff}}{8\kappa \left[\left(\frac{\kappa}{2}\right)^2 + \Delta^2 \right]} \tag{4.7}$$

$$\bar{n}_z = \frac{G^2 \left[1 - \frac{(k_{tw} y_m)^2}{2} \right] S_{ff}}{4\kappa \left[\left(\frac{\kappa}{2}\right)^2 + \Delta^2 \right]}. \tag{4.8}$$

	Low g	Medium g	High g
Trap Power P_{tw} (mW)	200	450	700
Cavity Length L (mm)	11.7	7.8	6.3
Optom. Coupling $g/2\pi$ (kHz)	16.8	25.3	32.4
Mech. Frequency $\Omega_y/2\pi$ (kHz)	122	183	228
Linewidth $\kappa/2\pi$ (kHz)	220	330	411
Phase Noise Heat. $\Gamma_y^{(\text{PN})}/2\pi$ (kHz)	5.1	7.8	10.2

TABLE 4.1: We compare the parameters for the three different cooling configurations of Fig. 4.3. Experimentally we choose a configuration by setting the cavity length and trapping power which affects the parameters listed but results in the same phonon number. For all settings we use a particle radius of $R = 50\,\text{nm}$ and $S_{ff} = 2\pi \times 0.8\,\text{Hz}^2/\text{Hz}$. The color of each column matches the marker in the figure. We decide to name each configuration according to the optomechanical coupling relative to each other. For $y_{\text{m}}/\lambda < 25$ each configuration reaches ground-state.

As phase noise heating is less significant at the cavity node, we investigate the requirements for ground-state cooling of the y motion in Fig. 4.3 by plotting the results of Eq. (4.7) for different cavity lengths L, trapping powers P_{tw} and particle radii R. In Fig. 4.3(a) we show that we obtain the lowest phonon numbers close to the edge of the sideband resolved regime $\Omega_y \approx \kappa/2$. The mechanical stability of the optical tweezer w.r.t. the cavity dictates how close to the edge we have to operate to reach ground-state. In Fig. 4.3(b) we investigate three specific configurations of the parameter regime of (a), namely the low g, medium g and high g configuration according to Tab. 4.1. All three configurations benefit from small particle sizes and cool to the same phonon occupation of $\bar{n}_y < 1$ for $y_{\text{m}}/\lambda < 25$. The low g configuration has the smallest phase noise heating rate, but also the smallest cavity cooling rate while the high g configuration has a higher phase noise heating rate which is compensated by a higher cavity cooling rate. At first glance it seems like there is no particular reason to choose one over the other for ground-state cooling, but there are some aspects that were so far neglected. For simplicity, we assumed that laser phase noise is equally strong at the mechanical frequency for the three configurations. In practice, it depends on the specific system but typically decreases for higher frequencies, favoring the high g configurations for experiments. Additionally, we assumed that residual gas heating is negligible compared to phase

noise heating. Comparing the rates from Tab. 4.1 with Eq. (3.6) we require a pressures of $p < \{4, 6, 8\} \times 10^{-7}$ mbar for the low, medium and high g configurations respectively. If the vacuum level cannot be reached but the mechanical stability is sufficient it can be advantageous to choose a larger particle to increase the cooling rate even though the heating rate increases as well. So far we did not investigate the detection of the particle motion in ground-state, but focused on reaching it. Since the dipole scattered power scales with $P_{\mathrm{dp}} \propto \mathrm{Im}\,\alpha$ [123] and $\mathrm{Im}\,\alpha \propto V^2$ [114], a larger particle scatters more light and can therefore be detected more easily, thereby favoring the high g configuration. To summarize the results of this discussion in theory the low, medium and high g configurations are equivalent, but if it is technically possible to increase the trapping power, the high g setup is favorable in the experiment.

4.2   MECHANICAL STABILITY OF THE TRAP CENTER

After showing how crucial a precise and stable position of the optical tweezer w.r.t. the cavity intensity profile is, we discuss the stability of our setup. For experiments only a relative motion is relevant, therefore it does not matter if it is the cavity or tweezer which moves. However, to eventually improve the system it is necessary to determine the exact effects that destabilize the setup.

4.2.1   *Characterization of the Mechanical Stability*

In this section we conduct two independent measurements to determine the mechanical stability. The first requires to trap a particle and position it inside the cavity, as shown in Fig. 4.4(a). Since the intensity of the light leaking out of the cavity depends on the position of the particle (Sec. 3.5.1), we can detect the frequency and amplitude of the relative motion of cavity and tweezer with a photodetector at the output mirror. We start from the heterodyne detector signal in Eq. (2.34) and set $\phi_0 = \Delta\phi = 0$, since we are only interested in the amplitude of the signal. The detector signal is

$$D = 4GR\sqrt{P_{\mathrm{B}}P_{\mathrm{lo}}}\cos(\Delta\omega t), \qquad (4.9)$$

with P_{B}, the power of the field leaking through output mirror B and the detuning between the optical tweezer and local oscillator $\Delta\omega = \omega_{\mathrm{tw}} - \omega_{\mathrm{lo}}$. We then insert the field leaking through mirror B for a cavity pumped
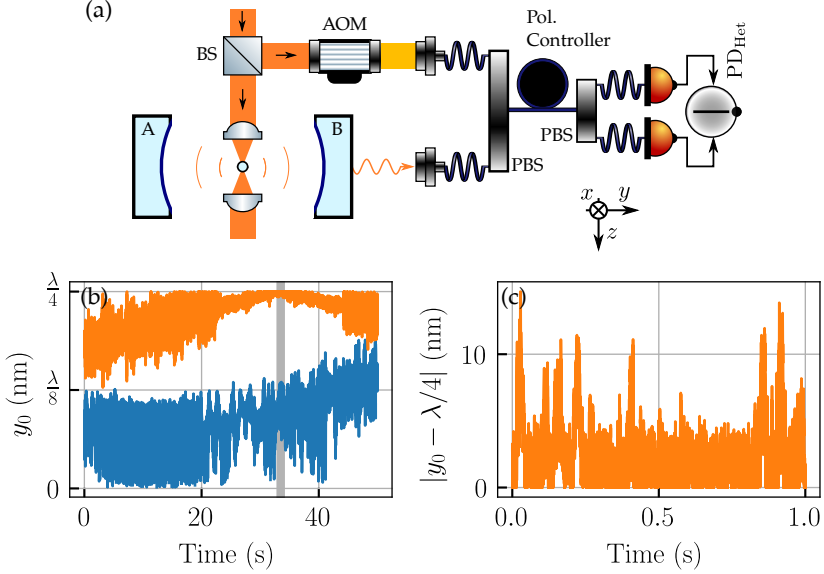
FIGURE 4.4: *Trap center drift relative to optical cavity.* (a) The setup works as described in Fig. 2.15, after removing the homodyning detector and choosing $\Delta\omega = 2\pi \times$ 1 MHz, for a laser wavelength $\lambda = 1550$ nm. (b) By moving the trapping lenses, we position the particle at the cavity field antinode (blue) or node (orange) at time $t = 0$ and measure the thermal drift by converting the detector signal to a particle position by applying Eq. (4.12). For $y_0 = 0$ nm ($y_0 = \lambda/4$) the particle is at the antinode (node). (c) We show the trap center displacement from $t = 33$ s to $t = 34$ s (grey shaded in (b)) for a particle positioned in the cavity node. The short term stability is better than 10 nm while the long term drift governs the full range from node to antinode.

by light scattered via the levitated particle as derived in Eq. (3.22). To simplify the expression, we assume highly reflective mirrors $r_A \approx r_B \approx 1$ and introduce the proportionality factor A_D,

$$D = A_D \sqrt{P_B[1 + \cos(2ky_0)]} \cos(\Delta\omega t) \tag{4.10}$$

$$A_D = \frac{|\beta E_{in}|^2 \mathcal{T}_B \omega_{fsr}^2}{\pi^2} \frac{GR\sqrt{2P_{lo}}}{\Delta^2 + (\kappa/2)^2}. \tag{4.11}$$

We define $\widetilde{D} = D(t = n2\pi/\Delta\omega)$ for $n \in \mathbb{N}$, the demodulated detector signal as well as $\widetilde{D}_0 = \widetilde{D}(y_0 = 0)$. We experimentally determine $\widetilde{D}_0$ by positioning the particle in the cavity antinode ($y_0 = 0$). Finally, we can invert Eq. (4.10) to find

$$\cos(2ky_0) = \left(\frac{\widetilde{D}}{\widetilde{D}_0}\right)^2 - 1. \tag{4.12}$$

In Fig. 4.4(c, d) we use this result to convert the signal strength of the carrier in our heterodyne detection to the particle position relative to the cavity. (c) We can either position the particle close to the antinode (blue curve) or node (orange curve) of the cavity field and observe the thermal drift over the course of almost one minute. As we are mostly interested in the stability around the node, we show the drift from $t = 33\,\text{s}$ to $t = 34\,\text{s}$ (grey shaded) in (d). For short enough time periods we have a better stability than $10\,\text{nm}$, while the trap drifts from node to antinode in about one minute. The dominant short time drift happens at frequencies around $\Omega_m = 2\pi \times 100\,\text{Hz}$.

Measuring the movement of the optical cavity is technically difficult and is expected to be the minor effect as the housing is very rigid and mounted on several damping stages. The cavity mirrors are both attached to piezos that are driven to lock the cavity length to an external laser. If only one cavity mirror is driven, the mirror can follow a drift of the other cavity mirror. Thereby, the cavity stays locked as the length is constant, but the whole cavity shifts w.r.t. the optical tweezer. Applying the same
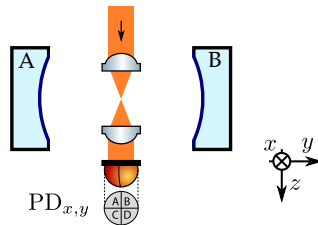

FIGURE 4.5: *QPD setup for optical tweezer drift detection.* There is no particle trapped and therefore also no light scattered into the cavity. We focus the collimated light from the optical tweezer on a QPD about 1m away from the tweezer and balance the detector by steering the beam with a mirror (not shown). The setup is sensitive to motion along x and y direction, but cannot detect a drift along z.

voltage to both mirrors reduces this effect. To be able to reach the cavity center with the trapping lenses the mobile optical trap is mounted on a free hanging nanopositioner as discussed in Sec. 2.3.5. The optical tweezer is therefore more prone to mechanical excitation when compared to the cavity. To measure the thermal drift of the optical tweezer we focus the collimated light from the tweezer without a trapped particle on a QPD as shown in Fig. 4.5. To be maximally sensitive we place the QPD about 1 m away from the collection lens. The detector is balanced with a mirror very close to the detector to minimize the influence of thermal motion of the mirror compared to the tweezer. Any transversal motion of the tweezer arm creates an imbalance on one of the two channels of the QPD.

We integrate the QPD signal for 80 s and show the PSDs of the two QPD channels in Fig. 4.6. Each channel measures predominantly the motion of the tweezer arm along x (polarization or gravity) and y (cavity), respectively. For the motion along y we observe mechanical vibrations close to 98 Hz,
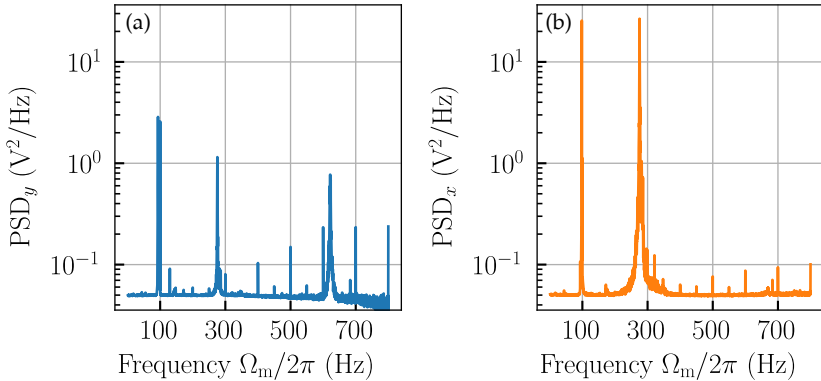

FIGURE 4.6: *Mechanical stability of the optical tweezer arm.* The optical tweezer light is collimated and focused on a QPD as shown in Fig. 4.5. We show the PSD of the y and x channel of the QPD. The sharp features at exact multiples of 100 Hz are due to electronic noise of the detector. The broader features stem from movement of the tweezer arm, which results in a power imbalance on the different quadrants of the QPD. (a) Along the cavity (y) direction, the arm moves at frequencies close to 98 Hz, 280 Hz and 620 Hz. (b) In direction of the tweezer polarization (x), which coincides with the direction of gravity, the arm moves also at frequencies close to 98 Hz, as well as 280 Hz, but not at 620 Hz.

280 Hz and 620 Hz. In particular the motion at 98 Hz we already noticed in the data presented in Fig. 4.4. For the motion along x the displacement is generally stronger than for the motion along y. When recording spectra at different moments in time we observe that the amplitude and frequency of the arm excitation fluctuate. It is expected that devices from the building infrastructure (e.g. pumps or air-conditioning systems) have a varying driving strength. We particularly observed that people talking or walking inside the room visibly affect how strongly the arm vibrates. Along the cavity axis we require a position stability of fractions of the wavelength while the stability along x and z is less criticial. Transversely to the cavity axis the coupling of the particle to the cavity scales with the $1/e^2$ intensity mode radius and not the wavelength ($w_c = 48\,\mu$m).

We conclude this section by summarizing that the dominant short term mechanical vibration of the optical tweezer w.r.t. the optical cavity happens at a frequency of $\Omega_m \approx 2\pi \times 98$ Hz and limits the position stability to $y_m \approx 10$ nm. Due to the design of the setup and the observations in Fig. 4.6, we suspect predominantly the optical tweezer to move and not the optical cavity.

4.3   CLASSICAL NOISE SOURCES IN HETERODYNE DETECTION

We plan to detect the ground-state c.m. motion signal of our particle via heterodyne detection. This minute particle signal can be rendered undetectable by laser phase noise and RIN. Furthermore, in Sec. 3.5 we discussed that laser phase noise (translated into trap displacement noise) affects our cooling abilities. In the previous section we concluded, that the mechanical vibration of the tweezer arm limits our ability to place the particle in the cavity antinode. It is therefore important to understand the impact of laser noise, entering the system via residual Raleigh scattering due to the particle displacement. By analyzing the detection noise we therefore not only obtain the detection limit, but also further investigate the process, that determines our minimal phonon occupation. Here, we therefore investigate how laser phase noise and RIN influence the heterodyne detection signal. To build an understanding of this involved noise propagation processes, we first investigate the simpler free space heterodyne detection scenario. In a second step we extend our model to our case of interest, by adding an optical cavity into one of the heterodyne interferometer arms. To clarify in which way laser noise enters the detector signal, we remind ourselves of

the heterodyne setup depicted in Fig. 2.14 and reiterate the fields on the detector,

$$E_s(t) = E_s^{(0)}(t - t_0)e^{-i[\omega t - kl_0 + \phi(t - t_0)]}$$
$$E_{lo}(t) = E_{lo}^{(0)}(t - (t_0 + \tau_{lo}))e^{-i[\omega_{lo}t - k_{lo}l_0 - k_{lo}L_{lo} + \phi(t - (t_0 + \tau_{lo}))]}.$$

In Sec. 2.4.2 we found the intensity on the heterodyne detector as

$$I = \frac{c\epsilon_0}{2}\left[|E_s(t) + E_{lo}(t)|^2 - |E_s(t) - E_{lo}(t)|^2\right].$$

One large benefit of a balanced detection is the rejection of correlated, common mode noise by eliminating the terms $|E_{lo}(t)|^2$ and $|E_s(t)|^2$ [161]. We point out, that photon shot noise indeed scales with laser power, but cannot be balanced away as the stream of photons on the two detectors is uncorrelated. Any detection noise that stems from the interference of the local oscillator and signal beam is not balanced away and will be investigated in this section. We will first focus on phase noise and then RIN in free space heterodyning. Then we introduce a dynamic cavity model proposed by [162], to repeat the derivations and find the expressions for a cavity-based detection. Starting point of all these calculations is the detector signal derived in Sec. 2.4.2, given by

$$\frac{D(t)}{D_0} = \frac{E_s^{(0)}(t - t_0)E_{lo}^{(0)}(t - (t_0 + \tau_{lo}))}{\overline{E}_s^{(0)}\overline{E}_{lo}^{(0)}}\cos\left(\Delta\omega t + \phi_0 + \Delta\phi\right). \qquad (4.13)$$

We remind ourselves, that $\Delta\omega = \omega_{lo} - \omega$ is the local oscillator detuning and ϕ_0 the phase that arises from the arm length difference. The constant $D_0 = 4GR_D\sqrt{P_sP_{lo}}$ depends on the power of the two beams, as well as impedance gain and responsivity of the detector. For the phase noise discussion it is particular important to recall

$$\Delta\phi(t) = \phi(t - (t_0 + \tau_{lo})) - \phi(t - t_0). \qquad (4.14)$$

The first term here is the phase of the input laser at time $t - (t_0 + \tau_{lo})$, whereas the second one is the phase of the input laser at $t - t_0$.

4.3.1 *Phase Noise*

In this section we consider a laser without RIN i.e. $E_s^{(0)}(t - t_0) = E_s^{(0)}(t) = \overline{E}_s^{(0)}$ and $E_{lo}^{(0)}(t - (t_0 + \tau_{lo})) = E_{lo}^{(0)}(t) = \overline{E}_{lo}^{(0)}$. Furthermore, we assume, that phase noise has the form

$$\phi(t) = \beta_{PN} \sin(\Omega t + \psi). \tag{4.15}$$

Here β_{PN} denotes the amplitude of phase noise at frequency Ω, given in units of rad. To find the implication of phase noise on the detector output we insert the definition into Eq. (4.14). For a phase noise amplitude $\beta_{PN} \ll 2\pi$ with an arbitrary phase ψ, we simplify $\Delta\phi$ by applying the sum to product identity from App. A.2.1 and define $\psi_0 := \psi - \Omega t_0$ to find

$$\begin{aligned}
\Delta\phi(t) =& \beta_{PN} \sin\{\Omega[t - (t_0 + \tau_{lo})] + \psi\} - \beta_{PN} \sin[\Omega(t - t_0) + \psi] \\
=& - 2\beta_{PN} \sin\left(\frac{\Omega\tau_{lo}}{2}\right) \cos\left(\Omega t - \frac{\Omega}{2}\tau_{lo} + \psi_0\right).
\end{aligned} \tag{4.16}$$

Since $\beta_{PN} \ll 2\pi$ also $\Delta\phi \ll 2\pi$ and we can expand Eq. (4.13) after applying the angle sum identity from App. A.2.1,

$$\begin{aligned}
\frac{D}{D_0} =& \cos[\Delta\omega t + \phi_0 + \Delta\phi(t)] \\
=& \cos(\Delta\omega t + \phi_0) \cos[\Delta\phi(t)] - \sin(\Delta\omega t + \phi_0) \sin[\Delta\phi(t)] \\
\approx& \cos(\Delta\omega t + \phi_0) - \Delta\phi(t) \sin(\Delta\omega t + \phi_0).
\end{aligned} \tag{4.17}$$

After inserting Eq. (4.16) into Eq. (4.17) and applying the trigonometric product to sum identity from App. A.2.1 we obtain

$$\begin{aligned}
\frac{D}{D_0} =& \cos(\Delta\omega t + \phi_0) \\
& + \beta_{PN} \sin\left(\frac{\Omega\tau_{lo}}{2}\right) \sin\left[(\Delta\omega + \Omega)t + \phi_0 + \psi_0 - \frac{\Omega\tau_{lo}}{2}\right] \\
& + \beta_{PN} \sin\left(\frac{\Omega\tau_{lo}}{2}\right) \sin\left[(\Delta\omega - \Omega)t + \phi_0 - \psi_0 + \frac{\Omega\tau_{lo}}{2}\right].
\end{aligned} \tag{4.18}$$

The first line in Eq. (4.18) is what we expected from a heterodyne measurement in the absence of noise. As in Eq. (2.35) we observe a signal at the

beating frequency $\Delta\omega$. In the second and third line we observe sidebands at $\Delta\omega \pm \Omega$. The strength of the sidebands depends on the phase noise amplitude β_{PN} as well as the time delay introduced by the delay line τ_{lo}.

To analyze our measurements it is often more convenient to investigate the signal in the frequency domain. We use the definition of the Fourier transform $\widehat{\phi}(\Omega)$ to find the single-sided PSD of phase noise $\widetilde{S}_{\phi\phi}(\Omega) = 4\pi \lim_{T\to\infty} |\widehat{\phi}(\Omega)|^2/T$, according to [114, 163]. To write the Fourier transform of the sine we introduce the Dirac delta function $\delta(\Omega' - \Omega)$ and write

$$\widetilde{S}_{\phi\phi}(\Omega') = 2\pi\delta(\Omega' - \Omega)\beta_{PN}^2. \tag{4.19}$$

Applying also the Fourier transform to Eq. (4.18) and choosing Ω' such that the carrier is at 0, we can write for the double-sided PSD of the detector signal due to phase noise

$$\begin{aligned} S_{VV}^{(PN)}(\Omega')/2\pi = &\frac{(\beta_{PN}D_0)^2}{2} \sin^2\left(\frac{\Omega\tau_{lo}}{2}\right) \delta(\Omega' - \Omega) \\ &+ \frac{(\beta_{PN}D_0)^2}{2} \sin^2\left(\frac{\Omega\tau_{lo}}{2}\right) \delta(\Omega' + \Omega). \end{aligned}$$

We substitute Eq. (4.19) and replace Ω' for Ω to find

$$S_{VV}^{(PN)}(\Omega) = \frac{D_0^2}{2} \sin^2\left(\frac{|\Omega|\tau_{lo}}{2}\right) S_{\phi\phi}(|\Omega|). \tag{4.20}$$

With Eq. (4.20) we see how laser phase noise $S_{\phi\phi}$ affects the noise floor in heterodyne measurements, generating noise sidebands around the carrier. We now repeat this analysis to derive a similar formula for RIN, before addressing the influence of an optical cavity.

4.3.2 *Relative Intensity Noise*

Following the approach from the previous section we now consider a laser without phase noise i.e. $\phi(t - t_0) = \phi(t - (t_0 + \tau_{lo})) = 0$. We assume that the electric field amplitude fluctuates as

$$E_0(t) = \overline{E}_0[1 + \beta_{RIN} \sin(\Omega t + \psi)], \tag{4.21}$$

with an average field amplitude $\overline{E}_0$. Again we consider the case in which fluctuations are small compared to the average field $\beta_{\text{RIN}} \ll 1$ at frequency Ω with an arbitrary phase ψ. We repeat the calculations from the previous sections assuming RIN instead of phase noise in App. A.1.1. We neglect noise that scales with β_{RIN}^2 and find the detector signal as

$$
\begin{aligned}
\frac{D}{D_0} = {}& \cos(\Delta\omega t + \phi_0) \\
&+ \beta_{\text{RIN}} \cos\left(\frac{\Omega\tau_{\text{lo}}}{2}\right) \sin\left[(\Delta\omega + \Omega)t + \phi_0 + \psi_0 - \frac{\Omega\tau_{\text{lo}}}{2}\right] \\
&- \beta_{\text{RIN}} \cos\left(\frac{\Omega\tau_{\text{lo}}}{2}\right) \sin\left[(\Delta\omega - \Omega)t + \phi_0 - \psi_0 + \frac{\Omega\tau_{\text{lo}}}{2}\right].
\end{aligned}
\tag{4.22}
$$

Before discussing the result we want to Fourier transform the detector signal, as we did in the case of phase noise. To be consistent with literature we first define the relative intensity $\text{RI}(t) = |E_0(t)|^2/|\overline{E}_0|^2 - 1$ [164–166]. Inserting our expression for the electric field and dropping terms that scale with β_{RIN}^2 we find

$$
\text{RI}(t) \approx 2\beta_{\text{RIN}} \sin(\Omega t + \psi).
\tag{4.23}
$$

The single-sided PSD of RIN is then defined by $\text{RIN}^2 = 4\pi|\widehat{RI}(\Omega)|^2$ with the Fourier transform of the relative intensity $\widehat{RI}(\Omega)$ leading to [163, 164]

$$
\text{RIN}^2(\Omega') = 2\pi\delta(\Omega' - \Omega)4\beta_{\text{RIN}}^2.
\tag{4.24}
$$

We can now Fourier transform Eq. (4.22) and use the defintion of RIN^2 to find

$$
S_{VV}^{(\text{RIN})}(\Omega) = \frac{D_0^2}{8} \cos^2\left(\frac{|\Omega|\tau_{\text{lo}}}{2}\right) \text{RIN}^2(|\Omega|).
\tag{4.25}
$$

With Eqs. (4.20) and (4.25) we are now able to characterize the noise figures of the laser, $S_{\phi\phi}(\Omega)$ and $\text{RIN}^2(\Omega)$, based on measurements of the heterodyne PSD $S_{\text{hh}} = S_{VV}^{(\text{PN})} + S_{VV}^{(\text{RIN})}$. To characterize phase noise it is feasible to choose a long delay line since $S_{VV}^{(\text{PN})} \to 0$ for $\tau_{\text{lo}} \to 0$. If we are limited by RIN or phase noise in our measurements we need to tune τ_{lo}

such that the stronger contributor is suppressed. As one of the two scales with the sine and the other with the cosine, it is not possible to eliminate both at the same time. In Fig. 4.10 we will use these results to find, that in our case, phase noise has a stronger contribution than RIN and use Eq. (4.20) to measure $S_{\phi\phi}$. Before considering the experimental results we continue the calculation to derive the influence of an optical cavity in one of the detection arms.

4.3.3 *Dynamic Cavity Model*

To capture the time delay introduced by a cavity we have to utilize a dynamic model and cannot rely on the steady-state cavity input output formalism used in Sec. 2.3.1. We follow the approach of [135, 162] and write the cavity output field $E_s(t)$ as a superposition of fields that entered the cavity at different times in the past as shown in Fig. 4.7.

For simplicity, we consider a cavity with symmetric mirror coatings, such that both mirrors have the same reflectivity, transmission and absorption. As in Sec. 2.3.1 the intensity reflectivity is given by $\mathcal{R}$, the transmission as $\mathcal{T}$ and absorption as $\mathcal{A}$. We further define $\tau_n := (2n+1)\tau$, the time a beam requires for $n + 1/2$ round trips and find the transmitted field

$$E_s(t) = -\mathcal{T} \sum_{n=0}^{\infty} \mathcal{R}^n E_s^{(0)}(t - \tau_n) e^{-i[\omega(t-\tau_n)+\phi(t-\tau_n)]}. \qquad (4.26)$$

The minus sign arises from our phase convention regarding transmitted and reflected fields as discussed in Sec. 2.4.1. The factor $\mathcal{T}$ indicates that every field has to be transmitted through the input and output mirror. The factor $\mathcal{R}^n$ takes into account that per round trip the light field has to be reflected from both mirror surfaces once. We choose to write an infinite series for mathematical convenience. In practice, of course the laser is not turned on infinitely long before starting measurements, but since $\mathcal{R} < 1$ contributions from the past get suppressed exponentially, and a steady-state is reached for times $\gg 1/\kappa$. Furthermore, $\mathcal{R} < 1$ also guarantees convergence of the series and we don't have to worry about cutting the series after a finite number of reflections. Without phase noise $\phi(t) = 0$, the factor $e^{i\omega\tau_n}$ indicates whether contributions from different input times add up constructively or cancel each other out. On resonance we find $\omega\tau_n = 2\pi m$, $m \in \mathbb{N}$ leading to constructive interference of all summands. As in the previous sections $E_s^{(0)}$ and ϕ are functions of $(t - \tau_n)$. They
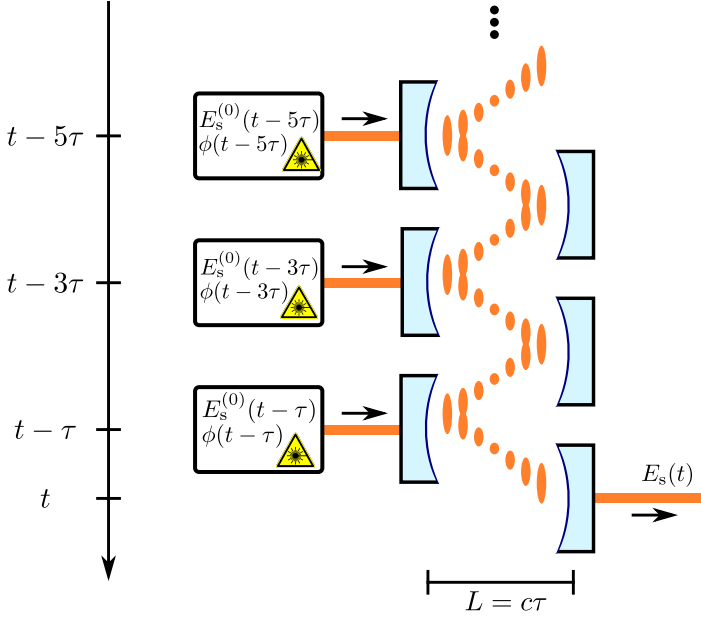
FIGURE 4.7: *The dynamic cavity model.* Influence of a cavity on phase noise and RIN. We consider the output field $E_\mathrm{s}(t)$ as a superposition of time-delayed input fields entering the cavity at $t - \tau, t - 3\tau, t - 5\tau, ...$ with τ being half of the round trip time. The laser's RIN, imprinted in $E_\mathrm{s}(t)$, and laser phase noise, imprinted in $\phi(t)$, have to be considered at the respective delayed times.

represent amplitude and phase noise of the input laser at times delayed by τ_n.

4.3.4 *Heterodyne Detection with an Optical Cavity*

In this chapter we modify the setup from Sec. 2.4.2 by adding an optical cavity into the signal arm as shown in Fig. 4.8.

We use Eq. (4.26) and write down the fields impinging on the two photodiodes of the heterodyne detector

$$E_\mathrm{s}(t) = -\mathcal{T} \sum_{n=0}^{\infty} \mathcal{R}^n E_\mathrm{s}^{(0)}\big(t - (t_0 + \tau_n)\big) e^{-i[\omega t - kl_0 - \omega\tau_n + \phi(t - (t_0 + \tau_n))]}$$

$$E_\mathrm{lo}(t) = E_\mathrm{lo}^{(0)}\big(t - (t_0 + \tau_\mathrm{lo})\big) e^{-i[\omega_\mathrm{lo} t - k_\mathrm{lo} l_0 - k_\mathrm{lo} L_\mathrm{lo} + \phi(t - (t_0 + \tau_\mathrm{lo}))]}. \tag{4.27}$$
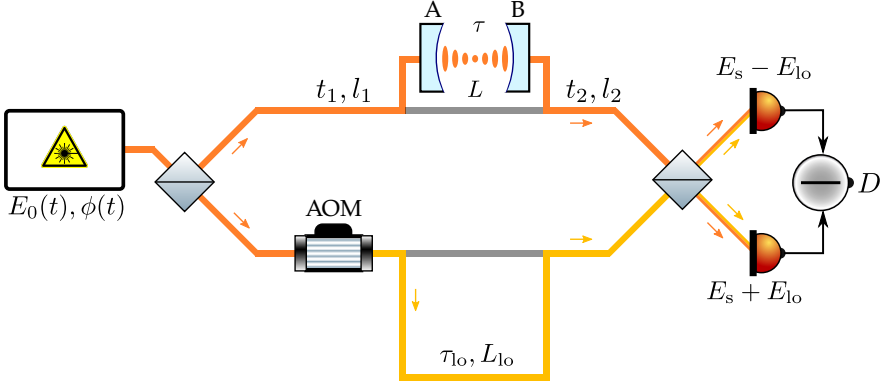
FIGURE 4.8: *A simplified sketch of a heterodyne detection scheme including an optical cavity. A laser with a fluctuating amplitude $E_0(t)$ or fluctuating phase $\phi(t)$ is split. The laser on the upper path travels a distance l_1 in time t_1 before entering an optical cavity. After leaving the optical cavity the laser travels a distance l_2 in time t_2 before being detected. The laser on the lower arm is frequency shifted by an acousto-optic modulator and travels a distance of L_{lo} in time τ_{lo} in addition to $l_0 = l_1 + l_2$.*

To simplify calculations we define

$$E_s^{(n)}(t) := E_s^{(0)}\big(t - (t_0 + \tau_n)\big)e^{-i[\omega t - kl_0 - \omega\tau_n + \phi(t-(t_0+\tau_n))]} \tag{4.28}$$

$$D_n := \frac{\big(E_s^{(n)}(t)E_{\text{lo}}^*(t) + E_s^{(n)*}(t)E_{\text{lo}}(t)\big)}{2\overline{E}_s^{(0)}\overline{E}_{\text{lo}}^{(0)}}. \tag{4.29}$$

Repeating the calculations from Sec. 2.4.2 we find the balanced detector signal

$$D = -\mathcal{T}D_0 \sum_{n=0}^{\infty} \mathcal{R}^n D_n. \tag{4.30}$$

4.3.5 *Phase Noise in Presence of an Optical Cavity*

As in the free space case we assume phase noise of the input laser according to Eq. (4.15). To find the total detector signal we first focus on simplifying the expression for D_n. We define $\phi_0^{(n)} := \phi_0 + \omega\tau_n$ as well as $\tau_{\text{lo}}^{(n)} := \tau_{\text{lo}} - \tau_n$

and $\psi_0^{(n)} := \psi_0 - \Omega \tau_n$ and observe that the derivation can be mapped to the free space calculation from Sec. 4.3.1. Afterwards, we can insert the expression into Eq. (4.30) and use identities to calculate the limit of the sum. The full calculation can be found in App. A.1.2. We write the total detector signal in the case of phase noise as $D^{(\mathrm{PN})} = D_{\mathrm{c}} + D_{\Omega}^{(\mathrm{PN})} + D_{-\Omega}^{(\mathrm{PN})}$. The different terms correspond to the carrier and the sidebands at $\pm\Omega$ with,

$$D_{\mathrm{c}} = \mathcal{T} D_0 C \sin(\Delta\omega t + \omega\tau + \phi_0 + \Phi)$$

$$D_{\Omega}^{(\mathrm{PN})} = \frac{\mathcal{T}\beta_{\mathrm{PN}} D_0}{2} C_{\Omega}^{(\mathrm{PN})} \sin[(\Delta\omega + \Omega)t + \Phi_{\Omega}^{(\mathrm{PN})}]$$

$$D_{-\Omega}^{(\mathrm{PN})} = \frac{\mathcal{T}\beta_{\mathrm{PN}} D_0}{2} C_{-\Omega}^{(\mathrm{PN})} \sin[(\Delta\omega - \Omega)t + \Phi_{-\Omega}^{(\mathrm{PN})}].$$

The coefficient C and phase of the carrier Φ depend on laser frequency and cavity length. For a laser frequency $\omega = \omega_{\mathrm{c}} - \Delta$ detuned by Δ and close to the cavity resonance ω_{c} we find (see Eq. (A.5) in the appendix)

$$D_{\mathrm{c}} = D_0 \frac{\mathcal{T}}{\mathcal{A} + \mathcal{T}} \sqrt{\frac{(\kappa/2)^2}{(\kappa/2)^2 + \Delta^2}} \sin(\Delta\omega t + \omega\tau + \phi_0 + \Phi). \qquad (4.31)$$

The factor in front of the sine matches the Lorentzian transfer function which we derived in the input-output formalism in Sec. 2.3.1. We continue to investigate the sideband expressions. The coefficients $C_{\Omega}^{(\mathrm{PN})}$, $C_{-\Omega}^{(\mathrm{PN})}$ and the phases $\Phi_{\Omega}^{(\mathrm{PN})}$ and $\Phi_{-\Omega}^{(\mathrm{PN})}$ depend on laser frequency, cavity length, local oscillator delay and sideband frequency. All definitions are given in the appendix in App. A.1.1. The PSD of the heterodyne detector signal, in presence of phase noise is therefore given by

$$S_{VV}^{(\mathrm{PN})}(\Omega) = \frac{(D_0 \mathcal{T})^2}{8} S_{\phi\phi}(|\Omega|) \times \begin{cases} (C_{\Omega}^{(\mathrm{PN})})^2, & \text{for } \Omega > 0 \\ (C_{-\Omega}^{(\mathrm{PN})})^2, & \text{for } \Omega \leq 0 \end{cases} \qquad (4.32)$$

If we compare this to the free space case of Eq. (4.20) we observe that the dependence on local oscillator delay τ_{lo} has become more involved. In the free space case, we are able to suppress phase noise entirely, by setting $\tau_{\mathrm{lo}} = 0$. We can understand this by investigating the cavity output field E_{s}. The output field can be described as a sum of input fields, as shown in Fig. 4.7. All these input fields are attenuated and delayed, inside the cavity,

depending on their number of round trips. We are only able to suppress the contribution of one of these input fields, by setting the correct local oscillator delay.

4.3.6 *Relative Intensity Noise in Presence of an Optical Cavity*

Before we are able to compare and interpret all our results, we finish the derivation of heterodyning noise. In this section we assume the same amplitude fluctuations as in the free space configuration, given by Eq. (4.21). The procedure to derive the detector signal is the same as in Sec. 4.3.5 and the full derivation can be found in App. A.1.3. We write the total detector signal in the case of phase noise as $D^{(\text{RIN})} = D_\text{c} + D_\Omega^{(\text{RIN})} + D_{-\Omega}^{(\text{RIN})}$,

$$D_\Omega^{(\text{RIN})} = \frac{-\mathcal{T}\beta_{\text{RIN}}D_0}{2}C_\Omega^{(\text{RIN})}\sin[(\Delta\omega + \Omega)t + \Phi_\Omega^{(\text{RIN})}]$$

$$D_{-\Omega}^{(\text{RIN})} = \frac{\mathcal{T}\beta_{\text{RIN}}D_0}{2}C_{-\Omega}^{(\text{RIN})}\sin[(\Delta\omega - \Omega)t + \Phi_{-\Omega}^{(\text{RIN})}].$$

We do not investigate the expression for D_c again, as the result is the same as in the case of phase noise. We continue to write the PSD of the heterodyne detector, which is limited by RIN as,

$$S_{VV}^{(\text{RIN})}(\Omega) = \frac{(D_0\mathcal{T})^2}{32}\text{RIN}^2(|\Omega|) \times \begin{cases} (C_\Omega^{(\text{RIN})})^2, & \text{for } \Omega > 0 \\ (C_{-\Omega}^{(\text{RIN})})^2, & \text{for } \Omega \leq 0 \end{cases}. \qquad (4.33)$$

The expression of $S_{VV}^{(\text{RIN})}$ and $S_{VV}^{(\text{PN})}$ in a cavity heterodyne detection setup take a similar form. To understand the differences, we have to investigate the coefficients $C_{\pm\Omega}^{(\text{RIN})}$ and $C_{\pm\Omega}^{(\text{PN})}$. We summarize their definitions from Apps. A.1.2 and A.1.3 as

$$C_\Omega^{(\text{PN})} = \sqrt{C_0(\omega, \Omega) - C_{sc}(\omega, \Omega)}$$

$$C_{-\Omega}^{(\text{PN})} = \sqrt{C_0(\omega, -\Omega) - C_{sc}(\omega, -\Omega)}$$

$$C_\Omega^{(\text{RIN})} = \sqrt{C_0(\omega, \Omega) + C_{sc}(\omega, \Omega)}$$

$$C_{-\Omega}^{(\text{RIN})} = \sqrt{C_0(\omega, -\Omega) + C_{sc}(\omega, -\Omega)}.$$

The definition of C_0 and C_{sc} can be found in Eq. (A.6).

4.3.7 *Summary and Analysis*

In the previous sections we derived the PSDs in a heterodyne measurement given a laser with phase noise or RIN. First we considered the free space case, before combining the results with a dynamic cavity model. In this section we summarize our findings in Tab. 4.2 and analyze its implications on our experiments. In the cavity case $C_0(\omega, \Omega)$ does not depend on the local oscillator delay τ_{lo}, but $C_{sc}(\omega, \pm\Omega)$ does. By adjusting the delay line on the reference arm we can tune sign and amplitude of $C_{sc}(\omega, \Omega)$ to either reduce the impact of phase noise or RIN at a certain frequency Ω. In most cases the laser will be either dominated by phase noise or RIN and we can tune the local oscillator delay i.e. the dominant contributor is suppressed.

We derive the optimal delay $\tau_{lo}^{(opt)}(\Omega)$ that either minimizes phase noise or RIN contribution by requiring $\frac{\partial C_{sc}(\omega, \Omega)}{\partial \tau_{lo}} = 0$.

$$\tau_{lo}^{(opt)}(\Omega) = \tau - \left\{ \arctan\left[\frac{B(\omega)A(\omega+\Omega) - A(\omega)B(\omega+\Omega)}{A(\omega)A(\omega+\Omega) + B(\omega)B(\omega+\Omega)} \right] + \pi n \right\} / \Omega$$

$$(4.34)$$

For any $n \in \mathbb{Z}$ the term $C_{sc}(\omega, \Omega)$ has an extremum. To maximally suppress phase noise (RIN) in the detection one has to pick n to be even (odd). We emphasize that this procedure only minimizes detection noise at a certain cavity detuning and detection frequency. Furthermore, minimizing noise in one sideband (e.g. $+\Omega$) will not minimize noise in the other sideband ($-\Omega$). The only way to circumvent this problem is to insert a component into the reference arm that introduces a frequency dependent delay such as an optical cavity. In Fig. 4.9 we analyze how to suppress the influence of both phase noise and RIN separately for a high finesse cavity.

	Free Space	Cavity
$S_{VV}^{(PN)}(\Omega)/S_{\phi\phi}(|\Omega|)$	$\frac{D_0^2}{2}\sin^2\left(\frac{|\Omega|\tau_{lo}}{2}\right)$	$\frac{(D_0\mathcal{T})^2}{8}[C_0(\omega,\Omega) - C_{sc}(\omega,\Omega)]$
$S_{VV}^{(RIN)}(\Omega)/\text{RIN}^2(|\Omega|)$	$\frac{D_0^2}{8}\cos^2\left(\frac{|\Omega|\tau_{lo}}{2}\right)$	$\frac{(D_0\mathcal{T})^2}{32}[C_0(\omega,\Omega) + C_{sc}(\omega,\Omega)]$
Carrier	$\frac{D_0^2}{2}$	$\frac{D_0^2}{2}\left(\frac{\mathcal{T}}{\mathcal{A}+\mathcal{T}}\right)^2 \frac{(\kappa/2)^2}{(\kappa/2)^2 + \Delta^2}$

TABLE 4.2: We compare the noise measured in a heterodyne detection normalized by laser phase noise $S_{\phi\phi}(|\Omega|)$ (first row) or RIN $\text{RIN}^2(|\Omega|)$ (second row). In the third row we show the power measured at the carrier frequency.

	Description	Value
$\mathcal{R}$	mirror reflectivity	0.9999753
$\mathcal{T}$	mirror transmission	23.7 ppm
L	cavity length	5 mm
$\mathcal{F}$	finesse	127k
λ	laser wavelength	1550 nm
$\omega - \omega_{\text{lo}}$	local oscillator detuning	$2\pi \times 1$ MHz
κ	cavity linewidth	$2\pi \times 235$ kHz
G	transimpedance gain	50 kV/A
R_{D}	responsivity	1.04 A/W
P_{lo}	local oscillator power	0.35 mW
P_{s}	signal power	2.26 µW

TABLE 4.3: Parameters used to characterize our heterodyne detection noise.

Since we are neither looking at the first nor second generation cavity we summarize the relevant experimental parameters in Tab. 4.3.

The derivations in this chapter show that there are knobs to tune the influence of phase noise and RIN in our heterodyne detection. We continue to discuss what is the optimal scenario for our experiments. The ultimate noise limit we can reach is photon shot noise. We will now derive criteria which are required to lower phase noise and RIN contributions below the shot noise limit. The single-sided PSD, for a shot noise limited photo current, as derived by Schottky reads [167]

$$\widetilde{S}_{II}^{sn}(f) = 2eI. \tag{4.35}$$

Here e and I are the electron elementary charge and average current respectively. We relate the average photo current to the optical power incident on the photodetector my multiplying with the responsivity $I = R_{\text{D}}P$. Furthermore, we convert to the voltage PSD by multiplying with the photodetector gain G^2

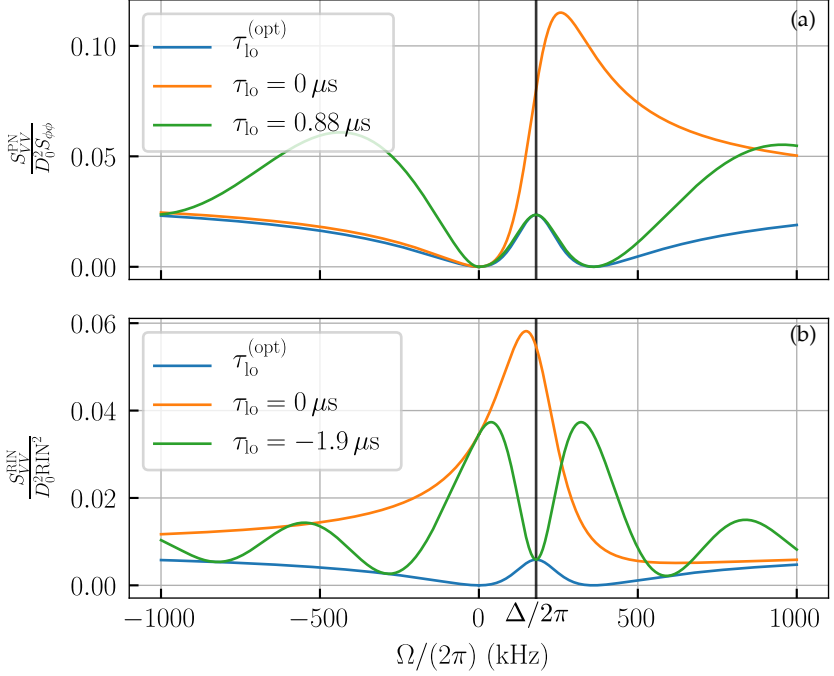$$\widetilde{S}_{VV}^{sn}(f) = 2eG^2R_{\text{D}}P. \tag{4.36}$$

FIGURE 4.9: *Suppression of phase noise or RIN in heterodyne detection by tuning local oscillator delay.* For cavity parameters described in Tab. 4.3 and a detuning $\Delta = 2\pi \times 180\,\text{kHz}$ we plot the normalized noise spectra for different local oscillator delays τ_{lo}. (a) The heterodyne PSD in absence of RIN is normalized by D_0^2 and $S_{\phi\phi}$ to make the quantity dimensionless and independent of input laser power and input laser phase noise. The orange curve corresponds to a constant delay of $\tau_{\text{lo}} - \tau = 0\,\mu\text{s}$ whereas for the green curve we choose $\tau_{\text{lo}} - \tau = 0.88\,\mu\text{s}$ to minimize noise at $\Omega = \Delta$. The blue curve denotes the noise level obtained by choosing the ideal delay for each frequency Ω to minimize phase noise according to Eq. (4.34). (b) The heterodyne PSD in absence of phase noise is normalized by D_0^2 and RIN^2. As in (a) the orange curve represents a delay line with $\tau_{\text{lo}} - \tau = 0\,\mu\text{s}$. The green curve arises from a delay line minimizing the influence of RIN at $\Omega = \Delta$ given by $\tau_{\text{lo}} - \tau = -1.9\,\mu\text{s}$. The blue curve denotes the noise level obtained by choosing the ideal delay for each frequency Ω to minimize RIN.

In our heterodyne detection scheme two beams are impinging on the detector. We choose the local oscillator power $P_{lo} \gg P_s$ such that the shot noise level is well approximated by the local oscillator $S_{VV}^{sn} = 4eG^2 R_D P_{lo}$. We multiplied by an additional factor of 2 since we defined P_{lo} as the power shining on only one of the two balanced photodiodes. We combine the results of this sections in Eqs. (4.32) and (4.33) and insert the definition of D_0 from Eq. (2.32) to find

$$S_{VV}^{(PN)} = 8 S_{\phi\phi}(GR_D\mathcal{T})^2 P_s P_{lo} \left[C_0(\omega,\Omega) - C_{sc}(\omega,\Omega) \right]$$
$$S_{VV}^{(RIN)} = 2 \text{RIN}^2 (GR_D\mathcal{T})^2 P_s P_{lo} \left[C_0(\omega,\Omega) + C_{sc}(\omega,\Omega) \right]. \qquad (4.37)$$

To be shot noise limited in the heterodyne detection we require $S_{VV}^{sn} > S_{VV}^{PN}$ as well as $S_{VV}^{sn} > S_{VV}^{RIN}$ which leads to the criteria

$$S_{\phi\phi} P_s < \frac{e}{2\mathcal{T}^2 R_D} \frac{1}{C_0(\omega,\Omega) - C_{sc}(\omega,\Omega)}$$
$$\text{RIN}^2 P_s < \frac{2e}{\mathcal{T}^2 R_D} \frac{1}{C_0(\omega,\Omega) + C_{sc}(\omega,\Omega)}.$$

In practice the right hand side of Eq. (4.38) is fixed by cavity and photodetector parameters that are difficult to tune or given by the requirements for particle c.m. cooling. To anyway fulfill the criteria either the noise figures of the laser must be sufficiently low or we are limited in the amount of signal power on the detector.

In Fig. 4.10 we show experimental data for heterodyne measurements with and without an optical cavity and compare the results to the developed theory. In (a) we show the normalized PSD of the detector signal of a heterodyne setup without as cavity, as shown in Fig. 2.14 for varying local oscillator delay lines. We choose $L_{lo} \leq 50\,\text{m}$ i.e. $|\Omega|\tau_{lo} = |\Omega|L_{lo}/c \ll 2\pi$ and approximate Eqs. (4.20) and (4.25) to find

$$S_{VV}^{(PN)}(\Omega) \approx \frac{D_0^2}{2} \left(\frac{|\Omega|L_{lo}}{2c} \right)^2 S_{\phi\phi}(|\Omega|) \qquad (4.38)$$

$$S_{VV}^{(RIN)}(\Omega) \approx \frac{D_0^2}{8} \text{RIN}^2(|\Omega|). \qquad (4.39)$$

In Fig. 4.10(a) we observe that the noise close to the carrier at $\Omega = 0$ indeed scales as $\propto L_{lo}^2$ and assume that phase noise dominates our heterodyne measurements. We continue to extract $S_{\phi\phi}$ from the measurements in
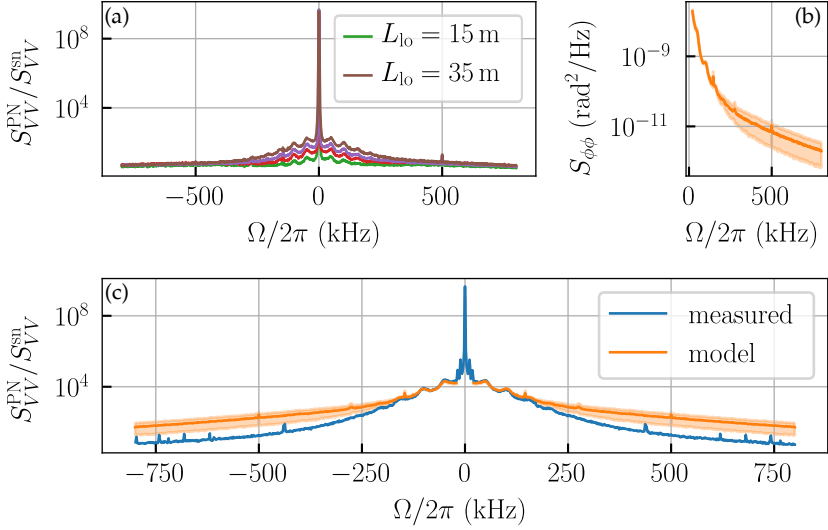
FIGURE 4.10: *Detected heterodyne noise PSD with and without cavity.* The *x* axes of all subfigures are labeled with respect to the beating frequency $\Delta\omega$. (a) For a heterodyne setup without an optical cavity, as shown in Fig. 2.14, we plot the PSD of the detector voltage, normalized to the PSD of shot noise. The sharp feature in the center is the carrier peak. The background far away from the carrier is limited by shot noise. The broad feature with ripples stem from excess laser noise. The different curves correspond to different local oscillator delay lines L_{lo}. We observe the noise increasing from the green to the brown curve corresponding to $L_{\mathrm{lo}} = \{15, 20, 25, 35\}$ m. (b) We employ Eq. (4.20) and extract $S_{\phi\phi}$ from the measurements in (a). The solid line denotes the mean of $S_{\phi\phi}$ with the shaded area corresponding to a standard deviation. (c) We conduct a heterodyne measurement with a cavity in the signal path as shown in Fig. 4.8. We insert $S_{\phi\phi}$ which we experimentally determined and plot in (b) into Eq. (4.32) for cavity parameters listed in Tab. 4.3. We compare the PSD measured with a cavity (blue) to the noise we expect from the model (orange). We observe that the model captures the noise at the carrier and overestimates the noise in the tail. This can be explained by uncertainties of the cavity parameters and limitations of the model. We assumed small and continuous phase fluctuation at the laser. Large phase jumps would not be captured by the model and lead to a different result. However, the model is able to predict the measured phase noise up to an order of magnitude.

(a) and plot the result including the uncertainty in (b). Finally, we include an optical cavity into the signal arm of the heterodyne setup as shown in Fig. 4.8 and compare the detected PSD to the expectation from our model according to Eq. (4.32) in combination with the experimentally determined phase noise PSD $S_{\phi\phi}$. In Fig. 4.10(c) we observe that the model qualitatively predicts the measured signal with better agreement close to the carrier and deviations in the tails. We insert $S_{\phi\phi}(2\pi \times 200\,\text{kHz})$ into Eq. (4.38) and find that we are limited to a cavity output power of $2P_{\text{s}} \approx 9\,\text{nW}$ to be shot noise limited at $\Omega = 2\pi \times 200\,\text{kHz}$, close to the frequency where we expect the sideband of the Stokes scattering from the particle's c.m. motion.

4.4 SIDEBAND-THERMOMETRY WITH AN OPTICAL CAVITY

The Raman effect was predicted in 1923 by Smekal [168] and observed by Raman for the first time in 1928 [169]. The Raman effect refers to the inelastic interaction of light and matter which is typically orders magnitude weaker than the elastic process of Rayleigh scattering [118]. Detecting the weak Raman signal was technically challenging and prevented the early success of Raman spectroscopy. The technical challenge was overcome in the early sixties when highly monochromatic, coherent and intense light sources became commercially available [170]. Nowadays a collection of Raman techniques has been developed to enhance the coupling strength and study the vibrational spectrum of various materials. The vibrational spectra create "fingerprints" for identification and interpretation of different specimens [171]. The phonon excitation by absorbing a photon and emission of a lower energy photon is referred to Stokes scattering, while the inverse process resulting in the annihilation of a phonon and the creation of a higher energy photon is called anti-Stokes scattering. As the latter requires the presence of a phonon in the system, the anti-Stokes scattering rate scales with the average phonon number $\bar{n}$ while the Stokes scattering rate scales with $\bar{n} + 1$ [122, 172]. The average occupation number of a harmonic oscillator in a thermal state is given by the Bose-Einstein distribution [120],

$$\bar{n} = \left[\exp\left(\frac{\hbar\Omega}{k_{\text{B}}T} \right) - 1 \right]^{-1}. \tag{4.40}$$

Using the Bose-Einstein distribution we can find the scaling of anti-Stokes scattering compared to Stokes scattering

$$\frac{\overline{n}}{\overline{n}+1} = \exp\left(-\frac{\hbar\Omega}{k_B T}\right). \tag{4.41}$$

The vibrational frequencies studied by the Raman spectroscopy community are in the terahertz regime and hence even at room temperature (300 K) the Stokes process dominates the anti-Stokes process. Therefore, most Raman techniques focus on detecting Stokes photons [142, 173, 174]. In levitated particle experiments at room temperature Stokes and anti-Stokes process are practically equally strong, as the c.m. frequencies are on the order of hundreds of kilohertz. To resolve an asymmetry between the two scattering rates we need to couple the system to a low temperature bath. In our measurements we can determine the scattering rates by measuring the number of Stokes and anti-Stokes photons corresponding to the areas under the respective sideband in a heterodyne measurement [117], hence the terminology sideband-thermometry. This technique has been used outside the Raman spectroscopy community to characterize the average motional energy of single atoms or atom clouds inside optical traps [38, 39, 175]. Recently, sideband-thermometry has been used both in free space levitated optomechanics [72, 73] as well as cavity levitated particle systems [70] to measure the average phonon number close to the motional ground-state.

4.4.1 *Cavity-Induced Sideband Asymmetry*

In our experiments, light from the tweezer at frequencies ω_{tw} coherently scatters into the cavity mode, into sidebands at $\omega_{tw} \pm \Omega_q$ with $q \in \{x, y, z\}$. On the detector we interfere the light leaking through one mirror with a local oscillator field at frequency ω_{lo}, as shown in Fig. 2.15. The detuning of the local oscillator w.r.t. the tweezer field is defined as $\Delta_{lo} = \omega_{tw} - \omega_{lo}$. The PSD of the photocurrent of the heterodyne detector S_{hh} contains a signature of Rayleigh scattered photons at Δ_{lo}, as well as Stokes scattered photons at frequencies $\Delta_{lo} - \Omega_q$ and anti-Stokes scattered photons at $\Delta_{lo} + \Omega_q$. The Rayleigh photons do not carry any information about the oscillators motion, but depend on the cavity detuning w.r.t. to the optical tweezer and the particle position relative to the cavity intensity profile as discussed in Sec. 3.5.1. To summarize our previous findings, Rayleigh scattering is maximal (minimal) for a particle at the antinode (node) of the cavity field. At $\Delta = 0$ the cavity maximally enhances Rayleigh scattering. As the detuning is increased, the Rayleigh scattered power decreases. The amount of (anti-)Stokes scattered photons, that we can detect behind a cavity mirror is more

intricate. We explain it in two steps. The coupling of mechanical motion and cavity mode is given by the optomechanical coupling rates in Eq. (3.3). Inelastic scattering from the z oscillator (tweezer axis) is maximal (minimal) at the antinode (node), similar to the Rayleigh scattering. Inelastic scattering from the y motion on the other hand follows the opposite dependence and is maximal (minimal) in the cavity node (antinode). As for the Rayleigh scattering the inelastic scattering is enhanced by the cavity depending on frequency and cavity detuning. In our experiments we cool the particle motion by enhancing anti-Stokes scattering with a blue detuned cavity. Therefore, we expect to see different scattering rates stemming from the cavity enhancement, which we refer to as cavity-induced sideband asymmetry. If we go one step further and consider a particle cooled close to ground-state, we expect an additional asymmetry of the sidebands, according to Eq. (4.41). This asymmetry will depend on the cooling rate of the cavity which in turn depends also on cavity detuning and particle position. Since we can independently measure the cavity parameters, we can compensate for the cavity-induced asymmetry, as long as the Stokes scattering is not suppressed strong enough to be buried by noise. To avoid suppressing the Stokes peak, beyond measurement capabilities, it is beneficial to have a cavity linewidth comparable to the mechanical frequency $\kappa \approx \Omega_y$. We define the measured asymmetry between the area under the anti-Stokes and Stokes peaks as

$$
A_q := \frac{\int_{-\delta}^{\delta} S_{\mathrm{hh}}(\Delta_{\mathrm{lo}} + \Omega_q + \Omega)d\Omega}{\int_{-\delta}^{\delta} S_{\mathrm{hh}}(\Delta_{\mathrm{lo}} - \Omega_q + \Omega)d\Omega}, \tag{4.42}
$$

where we assume that the peaks are narrow enough and sufficiently far apart to integrate over almost the full area by choosing an appropriate window 2δ. This spectral separation is not possible anymore close to ground-state, where the y peak gets sufficiently wide to overlap significantly with the x peak. In this case, we have to fit the x and y peaks simultaneously to appropriately determine the area. According to Refs. [70, 74], we can factorize the asymmetry as $A_q = A_q^{(c)} A_q^{(\mathrm{th})}$ with the thermal asymmetry $A_q^{(\mathrm{th})} = \overline{n}_q/(\overline{n}_q + 1)$ and $A_q^{(c)}$ incorporating the cavity-induced asymmetry. We assume here that both Stokes and anti-Stokes sidebands are detected with the same efficiency which we can verify by inverting the sign of the detuning of the local oscillator Δ_{lo}. From Eq. (2.11), we derive,

$$A_q^{(c)} = \frac{\kappa^2 + 4(\Delta + \Omega_q)^2}{\kappa^2 + 4(\Delta - \Omega_q)^2}. \tag{4.43}$$

The oscillator average phonon number is then given by

$$\bar{n}_q = \frac{A_q}{A_q^{(c)} - A_q}. \tag{4.44}$$

4.4.2 A Setup for Cavity Heterodyne Detection

In Sec. 4.5 we present the full setup including all improvements that were included over the course of the project. To focus on the key elements for sideband-thermometry, we now present a simplified setup in Fig. 4.11. The field E_{tw} at frequency ω_{tw} is split to derive the local oscillator E_{lo} at frequency ω_{lo} with detuning $\Delta_{\text{lo}} = 2\pi \times 1\,\text{MHz}$ for heterodyne detection as described in Sec. 2.4.2. The largest fraction of the light forms the optical trap with a focal power of $P_{\text{tw}} \approx 500\,\text{mW}$ that will scatter via the particle into the TEM$_{00}$ mode of an optical cavity. As explained in Sec. 2.3.3 we lock the cavity to the TEM$_{10}$. For this we derive a field E_{lock} at frequency ω_{lock} from the tweezer with the relation $\omega_{\text{lock}} - \omega_{\text{tw}} = \omega_{10} - \omega_{00} + \Delta$. Thereby, the lock beam is resonant with the optical cavity as well as the tweezer beam, up to a detuning Δ. We reiterate here that the difference of the resonance frequencies of the two cavity modes $\omega_{10} - \omega_{00}$ depends on the cavity length and lock laser wavelength.

In our cooling experiments we require ω_{lock} to be tuned, such that $\Delta \approx \Omega_y$ to enhance anti-Stokes scattering. As both the cavity length and the laser wavelength are affected by thermal drifts, $\omega_{10} - \omega_{00}$ is slightly different at the beginning of every experiment. To correct for this we zero point calibrate the detuning to $\Delta = 0$. We do this with a calibration beam E_{calib}, derived from the optical tweezer at frequency ω_{tw}. We imprint phase-modulation sidebands on the calibration field with an EOM at $\Omega_{\text{calib}} = 2\pi \times 200\,\text{kHz}$ and higher harmonics. Both the tweezer light scattered by the particle, as well as the calibration laser can be measured by the heterodyne detector, after leaking through the right cavity mirror. The far detuned lock beam is low in power and does not add a significant amount of shot noise on the detector. The calibration laser has a power $P_{\text{calib}} < 1\,\text{nW}$ and is turned off during measurements to not disturb the particle motion. The calibration steps are then:
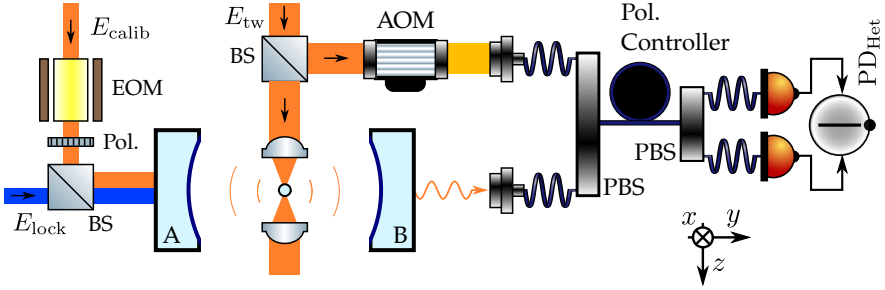
FIGURE 4.11: *Simplified setup for cavity cooling and heterodyne detection.* A fraction of the field E_{tw} is split to derive a local oscillator that is used as a reference field in heterodyne detection. The rest is focused to a diffraction limited spot to confine a particle in 3D which in turn scatters tweezer light into the cavity. The cavity length is locked to the TEM_{10} mode of a field E_{lock} as described in Sec. 2.3.3. The lock field is far detuned from the tweezer field and does not influence the heterodyne detection signal as the shot noise of the low power beam is negligible to the local oscillator field. By rotating the polarizer we can additionally inject the calibration field E_{calib} into the cavity. The calibration laser has the same frequency as the tweezer and has sidebands imprinted at multiples of $2\pi \times 200\,\text{kHz}$ which can be used to measure the cavity linewidth and detuning in-situ. To not affect the particle motion the laser can be fully turned off during measurements. The heterodyne detection scheme is explained in Sec. 2.4.2.

1. Position the particle outside of the optical cavity to avoid scattering into the cavity.

2. Set $\omega_{\text{lock}} - \omega_{\text{tw}}$ to the theoretical value of $\omega_{10} - \omega_{00} \approx 2\pi \times 4.2\,\text{GHz}$. For every change in cavity geometry this value has to be calculated again according to Eq. (2.24).

3. While sweeping the cavity length, monitor the intensity leaking through mirror B. As the cavity becomes resonant with the lock beam and the calibration beam for a certain length the intensity increases behind the cavity mirror. Tune ω_{lock} with a frequency generator until both the lock beam and the calibration beam become resonant at the same cavity length.

4. Lock the cavity and monitor the signal of the heterodyne detector. The PSD of the detected signal contains peaks at the beating frequencies of the local oscillator with the calibration beam carrier and sidebands, as shown in Fig. 4.12(a, b).
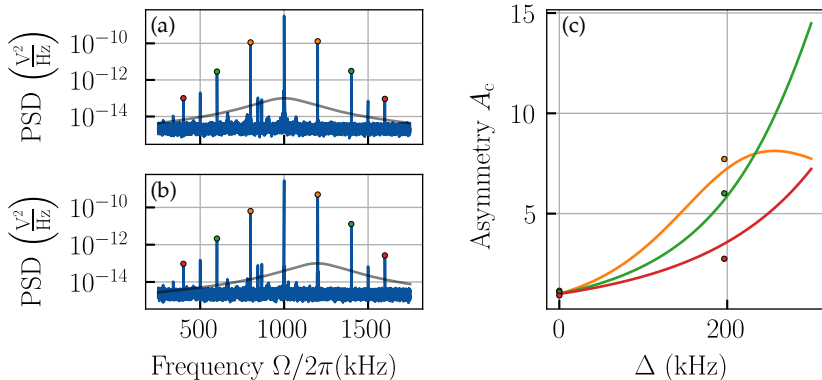
FIGURE 4.12: *In situ method for cavity detuning calibration.* (a, b) PSD (blue curve) of signal detected by PD_{PDH} in heterodyne detection setup as shown in Fig. 4.11 for two different cavity detunings. We measure a beating signal of the local oscillator and the calibration beam carrier and sidebands equally spaced by $\Omega_{calib} = 2\pi \times 200 \, \text{kHz}$. We overlay the cavity transfer function of Lorentzian lineshape in black to visualize the linewidth and detuning. The detunings are $\Delta = 0$ and $\Delta = 2\pi \times 196 \, \text{kHz}$ in (a) and (b) respectively. (c) With Eq. (4.43) we can relate the cavity detuning to the asymmetry between left and right sidebands. Each curve shows the expected asymmetry for a cavity linewidth $\kappa = 2\pi \times 320 \, \text{kHz}$ and peaks at Ω_{calib}, $2\Omega_{calib}$ and $3\Omega_{calib}$ with colors matching the markers of (a, b). Additionally, we show datapoints for the asymmetries measured in (a, b).

5. Fine tune ω_{lock} with the frequency generator until every sideband pair has the same amplitude on both sides of the carrier to achieve[5] $\Delta = 0$.

During experiments it is not feasible to set the detuning back to $\Delta = 0$ to confirm that $\omega_{10} - \omega_{00}$ has not drifted, as the particle is not cooled any more and can be lost from the trap. Instead we can measure the asymmetry of the calibration sidebands and compare them to the expected asymmetry as shown in Fig. 4.12(c).

---

5 After the fine tuning is complete we continue adjusting ω_{lock} to get an estimate for how precise we can determine $\Delta = 0$. We observe an uncertainty of less than $2\pi \times 10 \, \text{kHz}$ which corresponds to $\approx \kappa/30$ and has a neglectable influence on the cooling performance

4.4.3   *Cavity-Based Cooling Close to the Quantum Ground-State*

After discussing how to extract the mean phonon numbers from a sideband asymmetry and how to calibrate the zero point of the cavity detuning, we are set to interpret measurement data shown in Fig. 4.13. The setup used to record the heterodyne PSD is sketched out in Fig. 4.11 and described in detail in Sec. 2.4.2. Before considering the sideband asymmetries we present the experimental parameters in Tab. 4.4 and dissect the relevant contributions to the PSD S_{hh} detected by $\mathrm{PD_{Het}}$. For a system far away from the strong coupling regime, i.e. no significant hybridization of modes occurs [97, 176, 177], the full PSD is

$$S_{\mathrm{hh}} = S_{\mathrm{sn}} + S_{\mathrm{PN}} + S_{\mathrm{RR}} + \sum_{q \in \{x,y,z\}} \left(S_{\mathrm{qq}}^{(\Omega)} + S_{\mathrm{qq}}^{(-\Omega)} \right). \qquad (4.45)$$

The PSDs are in units of V^2/Hz, to improve readability we dropped the VV subscript used in Sec. 4.3 and imply e.g. $S_{\mathrm{sn}} = S_{VV}^{\mathrm{sn}}$. The different contributions in Eq. (4.45), from left to right, are respectively:

- Shot noise of the local oscillator[6]

- Phase noise of the laser transduced by the optical cavity

- The carrier peak at $\Omega = \Delta_{\mathrm{lo}}$, originating from Rayleigh scattered light interfering with the local oscillator

- Anti-Stokes and Stokes sidebands centered at $\Omega = \Delta_{\mathrm{lo}} + \Omega_q$ and $\Omega = \Delta_{\mathrm{lo}} - \Omega_q$ for each oscillator

The expressions for S_{sn} and S_{PN} are given in Sec. 4.3, additionally S_{RR} has a Lorentzian lineshape with a linewidth of $2\pi \times 1.6\,\mathrm{kHz}$ according to the manufacturer. In theory, the expression of Eq. (2.3) needs to be multiplied with the cavity transfer function Eq. (2.11), but as in our case the mechanical linewidths γ_q are small compared to the cavity linewidth κ we can simply correct each peak with a scaling factor, without altering the Lorentzian lineshape.

In Fig. 4.13(a) we show the heterodyne PSD for a particle positioned at the minimum of the cavity intensity profile (node). The light blue datapoints in the background are calculated from a 400 ms timetrace. The grey datapoints indicate contributions to S_{hh} from the electronic noise of the data acquisition

---

6 since $P_{\mathrm{lo}} \gg P_{\mathrm{s}}$ with P_{s} the power leaking through the cavity mirror

Parameter	Value
Trap Power P_{tw} (mW)	380(5)
LO Power P_{lo} (μW)	70(2)
LO Detuning $\Delta_{\text{lo}}/2\pi$ (MHz)	1
Cavity Linewidth $\kappa/2\pi$ (kHz)	320
Cavity Detuning $\Delta/2\pi$ (kHz)	196(20)
Pressure p (mbar)	1.8×10^{-5}
Particle Radius R (nm)	70
Mechanical Freq. $\Omega_{x,y,z}/2\pi$ (kHz)	$\{146, 167, 53\}$

TABLE 4.4: Experimental parameters for our sideband asymmetry cooling experiments.

system and are not included in Eq. (4.45). Using the Welch method [178], we divide the timetrace into 30 segments and average to reduce noise, plotted in dark blue. At $\Omega = \Delta_{\text{lo}}$, we observe the Rayleigh peak and close by noise from the cavity lock electronics in the range $|\Delta_{\text{lo}} - \Omega| < 2\pi \times 10\,\text{kHz}$. Away from the carrier, the noise floor is dominated by shot noise from the local oscillator, indicated with a horizontal red line. Deviations from the red line that are not Stokes and anti-Stokes sidebands are originating from phase noise of the carrier S_{PN}, which is more pronounced at frequencies $\Omega > \Delta_{\text{lo}}$ due to cavity enhancement. At $\Omega = \Delta_{\text{lo}} \pm \Omega_z$ we observe narrow features marked in light red originating from inelastic scattering with the z oscillator. As the optomechanical coupling of the z motion to the cavity and hence also the cooling rate is weak at the node, the motion is only very weakly damped, resulting in a narrow linewidth. At $\Omega = \Delta_{\text{lo}} \pm \Omega_x$ we observe the Stokes and anti-Stokes sidebands of the x oscillator. For a tweezer polarization perfectly orthogonal to the cavity axis we expect the peak to be as narrow as the peaks corresponding to the z motion. A small tilt of the polarization axis results in moderate cooling of the x motion. Finally, at $\Omega = \Delta_{\text{lo}} \pm \Omega_y$ the broad Stokes and anti-Stokes peaks of the strongly damped y motion can be seen. To guide the eye we overlay the data with a Lorentzian fit. We want to point out the narrow spike, particularly visible on top of the anti-Stokes peak, but also present for the Stokes peak. The spike has a different width and amplitude in different measurements and is not visible if we inject the laser directly into the cavity. We therefore assume, that the feature is not only a measurement artifact, but part of the

Parameter	x	y	z
Stokes Area (V^2)	1.9×10^{-11}	3.14×10^{-11}	2.0×10^{-10}
anti-S. Area (V^2)	8.5×10^{-11}	1.20×10^{-10}	3.6×10^{-10}
FWHM $\gamma_q/2\pi$ (kHz)	2	12	0.5
Asymmetry A	4.5	3.83	1.8
Cavity Asymmetry A_c	5.1	5.96	1.9
Phonon Number $\bar{n}$	7.5	1.86	18

TABLE 4.5: Measured Stokes and anti-Stokes peak parameters for a particle positioned in the cavity node as shown in Fig. 4.13.

y motion. Our current understanding is, that the spike might stem from a slight asymmetry of the particle shape, resulting in libration of the particle. To obtain a conservative estimate of the phonon number, we integrate over the Lorentzian, attributed to the y motion and add the area of the spikes. In Tab. 4.5 we list the measured areas under the x, y and z peak as well as the linewidths of the oscillators.

We estimate the phonon numbers from the measured asymmetries according to Eq. (4.44). At this point, a word of caution is warranted: the accuracy of the inferred phonon numbers strongly depends on the accuracy of our experimental parameters. To illustrate this we use Eq. (4.44) to derive the uncertainty of the phonon number resulting from uncertainties of both the measured asymmetry and the cavity induced asymmetry. We calculate $\partial \bar{n}_q / \partial A_q$, $\partial \bar{n}_q / \partial A_q^{(c)}$ and employ the error propagation formula [179] to derive

$$\frac{\delta \bar{n}_q}{\bar{n}_q} = (\bar{n}_q + 1) \sqrt{\left(A_q^{(c)} \frac{\delta A_q}{A_q} \right)^2 + \left(\frac{\delta A_q^{(c)}}{A_q^{(c)}} \right)^2}. \qquad (4.46)$$

We observe that particularly for large phonon numbers, measurement uncertainties of the cavity asymmetry or measured sideband asymmetry affect the phonon estimation severely. To fully understand the sensitivity of the phonon number accuracy, we investigate the cavity induced asymmetry $A_y^{(c)}$ and assume $\Delta = \Omega_y$ to simplify Eq. (4.43),

$$A_y^{(c)} = 1 + 16 \left(\frac{\Omega_y}{\kappa} \right)^2. \tag{4.47}$$

We use again Gaussian error propagation [179] to find the uncertainty of $A_c^{(y)}$ arising from the uncertainty of κ and Δ,

$$\frac{\delta A_y^{(c)}}{A_y^{(c)} - 1} = \sqrt{\left(2\frac{\delta\kappa}{\kappa} \right)^2 + \left(\frac{\delta\Delta}{\Omega_y} \right)^2}. \tag{4.48}$$

Operating in the resolved sideband regime $\kappa \ll \Omega_y$ or close to it makes sideband-thermometry challenging since $A_y^{(c)}$ increases quadratically with Ω_y/κ and amplifies the error contribution from the measured sideband asymmetry in Eq. (4.46). Larger mechanical frequencies on the other hand decrease the impact of imprecision on the cavity detuning Δ. We combine Eqs. (4.46) and (4.48) to estimate the phonon number uncertainty in our experiment. With $\Omega_y/\kappa \approx 0.5$ and a conservative estimate of $\delta\kappa/\kappa = \delta\Delta/\kappa \approx 0.1$ we obtain an uncertainty of $\delta\overline{n}_y \approx 4$ for the y oscillator.

One aspect that we have ignored so far in our analysis, which could affect the phonon number estimation, is the role of phase noise in the detection. As mentioned, we observe a small deviation from shot noise in Fig. 4.13(a) at $\Omega > 2\pi \times 1\,\mathrm{MHz}$. Since the detector cannot distinguish between phase fluctuations of the detected field due to laser phase noise or due to particle motion, the (anti-)Stokes scattered light from the particle can interfere destructively or constructively with laser phase noise on the detector depending on their phase relation. This effect becomes especially evident in Fig. 4.13(b). All experimental parameters are the same as for (a) except for the particle position relative to the cavity intensity profile. Instead of placing the particle in the node we choose the antinode or intensity maximum. Rayleigh scattered light couples maximally to the cavity and the noise level originating from phase noise is orders of magnitude higher than shot noise. Besides the carrier we only observe features stemming from the z motion of the particle marked in red and from the y motion, marked in green. As the tweezer is polarized along the x axis which is almost orthogonal to the cavity axis the noise level overshadows any weak x (anti-)Stokes peaks. Since the optomechanical coupling of the z oscillator is maximal at the antinode, we indeed see broad (anti-)Stokes peaks, but the cooling is ultimately limited by laser phase noise as discussed in Sec. 4.1.
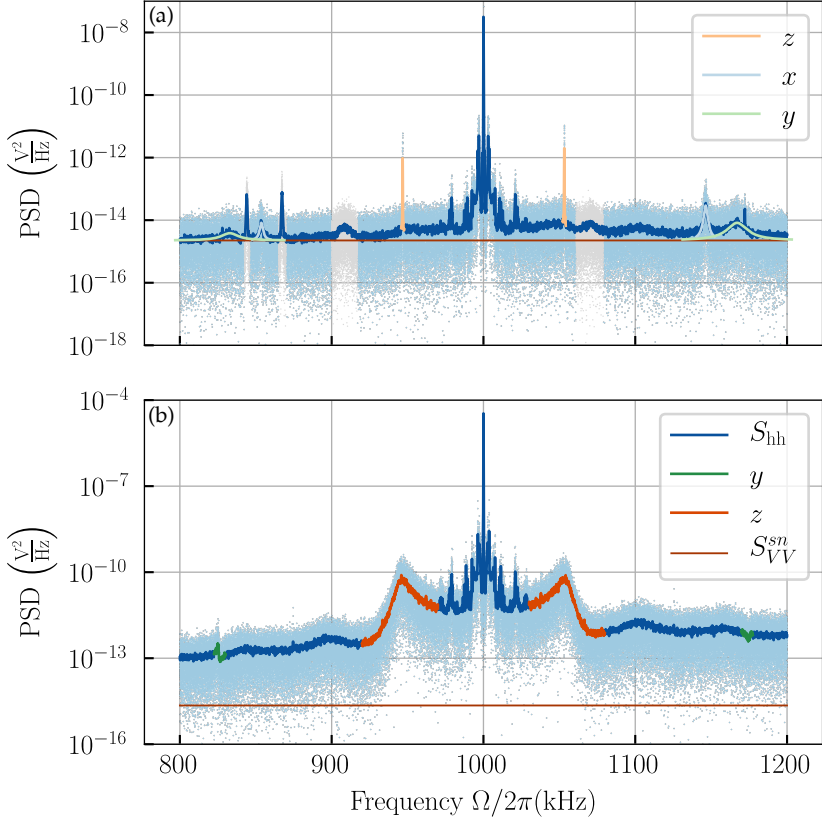
FIGURE 4.13: *Heterodyne spectra with sideband asymmetry of cavity cooled particles.* We detect light leaking through one cavity mirror with $\Delta_{\text{lo}} = 2\pi \times 1$ MHz. The central peak corresponds to Rayleigh scattered light while higher (lower) frequencies denote anti-Stokes (Stokes) scattering. We use the second generation cavity as described in Tab. 2.2, a trap power of $P_{\text{tw}} = 380(5)$ mW, particles with a radius of $R = 70$ nm and operate at a pressure of 1.8×10^{-5} mbar. We integrate for 400ms to obtain the light blue datapoints and derive through windowing the dark blue average curves. The horizontal red line represents the shot noise level of the local oscillator field of power $P_{\text{lo}} = 70(2)\,\mu$W. To guide the eye we mask the datapoints that are due to electronic noise of the data acquisition system in grey and mark features in green that correspond to the particles y motion, light blue for the x motion and red for the z motion. The PSDs in (a) and (b) correspond to a particle positioned a the cavity node and antinode respectively.

At $\Omega = \Delta_{lo} \pm \Omega_y$ we interestingly don't see sharp features corresponding to an uncooled y oscillator but destructive interference with the phase noise background showing that we indeed have to be careful when estimating PSD areas in the presence of phase noise.

In conclusion, we believe that we are close to ground-state cooling of a levitated particle with a minimum phonon occupation on the order of $\bar{n}_y \approx 10$. We are able to consider measurements, where the particle drifts through the cavity node and phase noise heating is negligible compared to gas recoil heating at 1.8×10^{-5} mbar. However, we still observe an elevated noise floor around the anti-Stokes peak arising from laser phase noise which might affect the phonon estimation. Slow drifts of the particle position as well as long waiting times to reach sufficiently high vacuum without losing the particle make experiments challenging. Maturing the system and improving stability will make it easier to acquire data for a longer time and scan cavity parameters. Thereby, we can find the optimal cooling configuration and decrease uncertainties on the cavity induced sideband asymmetry to enable more confident statements about the phonon number. To achieve this we reassembled the setup in the basement ($-$2nd floor) of the building after conducting the initial 3D cooling experiments on the 6th floor. We clearly observed an improvement in stability but could not reach ground-state cooling yet. In the next section we discuss the latest changes of the setup which should establish the necessary stability to overcome current limitations.

4.5 OPTICAL TRAPPING WITH A PARTICLE TRANSFER SYSTEM

In this section we discuss the implementation of a particle transfer system to further improve the trap stability w.r.t. the optical cavity. To achieve this we install a second optical tweezer that is not fiber-based on the damping stage of the optical cavity, as seen in Fig. 4.14. In Sec. 4.2 we concluded, that the movement of the optical tweezer relative to the cavity mainly stems from the transfer arm. By transferring the particle into a tweezer, that is formed by optics on the cavity damping stage itself, stability can be significantly improved. We additionally switch to a free space configuration, to have the freedom to rotate the tweezer polarization. Therefore, we can cool both and x and y motion to improve particle containment while pumping the chamber down to high vacuum. Only for ground-state measurements, we rotate the polarization to be perfectly vertical w.r.t. the cavity axis and to obtain minimal phonon numbers along the y direction. Furthermore, we

are not limited in trapping power anymore by an optical fiber. Therefore, the optical power can be chosen to reach minimal phonon numbers, as discussed in Sec. 4.1.
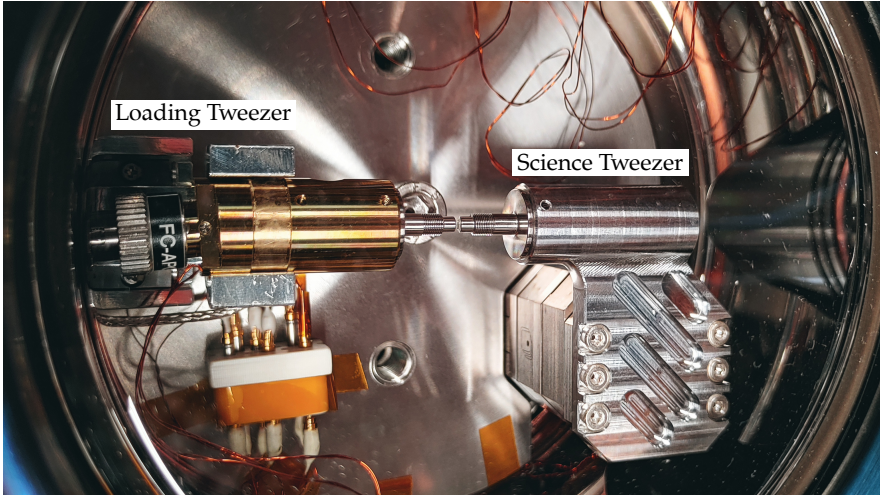

FIGURE 4.14: *Two tweezer setup without optical cavity.* Image taken through the top view port of our science chamber. The loading tweezer consists of a collimator mounted on a nanopositioner which is in turn attached to a hollow steel rod. The loading tweezer can be moved by retracting the steel rod to the left and inside the loading chamber. At the right end of the golden collimator we attach a custom lens holder which centers the trapping lens w.r.t. the collimator. The same holder and lens are used in the science tweezer on the right hand side. The science tweezer is also mounted on a nanopositioner but light couples into the holder through the viewport on the right and not a single-mode fiber. For first transfer tests we removed the cavity. It will be mounted via a rail attached to the screw holes visible in the damping plate below the tweezers, i.e. the center of the cavity is right at the middle between the loading and science tweezer lenses.

In the previous chapters we only used the fiber coupled optical trap, which we will here refer to as "loading tweezer". The new free space trap will be used to confine the particle during experiments and is hence denoted by "science tweezer". The particle trapping process and shift into the cavity was explained in Secs. 2.1 and 2.2.3 and is not affected by the science tweezer. To do experiments, we need to align the science tweezer with the center of the optical cavity. To achieve this, we need to trap a particle and monitor the amount of light, scattered into the cavity mode while tuning the tweezer

position. As we cannot directly trap the particle inside the science tweezer, we instead align the loading tweezer with the cavity. By collimating the diverging loading tweezer beam with the science tweezer we can overlap the focii of the two tweezers. Thereby, also the science tweezer is aligned with the center of the cavity. With the science tweezer in place we can realign the free space optics, shown in Fig. 4.15. This lengthy alignment process is only necessary during the first particle transfer. Once the science tweezer is aligned with the optical cavity we don't expect significant drifts that require realignment. In successive particle transfers, we align the loading tweezer with the science tweezer and are automatically located at the center of the cavity.

To transfer the particle from the loading to the science tweezer we proceed as follows. Once the focii are aligned, we gradually increase the power of the science tweezer while also gradually decreasing the power of the trapping tweezer. When the loading tweezer is completely turned off, the particle is only held by the science tweezer. The alignment of the tweezers w.r.t. each other is not only crucial to transfer the particle, but also to couple the science tweezer light back into the single-mode fiber inside the transfer arm. As we place the tweezers in between cavity mirrors any stray light, that is not collected, can couple into the cavity and raise the noise level on the detector or heat up the cavity housing. We showed in Sec. 2.3.5, that a temperature increase of the cavity housing induces a length drift of the cavity. Once the cavity length drifts too much the piezos are not able to compensate anymore for the drift and the cavity falls out of lock. To illustrate properly how all building blocks described here work together, we show the full setup in Figs. 4.15 and 4.16.

The latest status of the setup is, that we are able to trap particles with the loading tweezer and transfer the particle into the science tweezer. There appears to be no particular risk of losing the particle during the process. We observe, however, that the power, coupled from the science tweezer into the vacuum single-mode fiber, starts drifting after a few minutes. To mitigate the risk of destroying the fiber, we try to passively improve the mechanical stability and consider the implementation of a feedback system that keeps the loading tweezer aligned with the science tweezer.
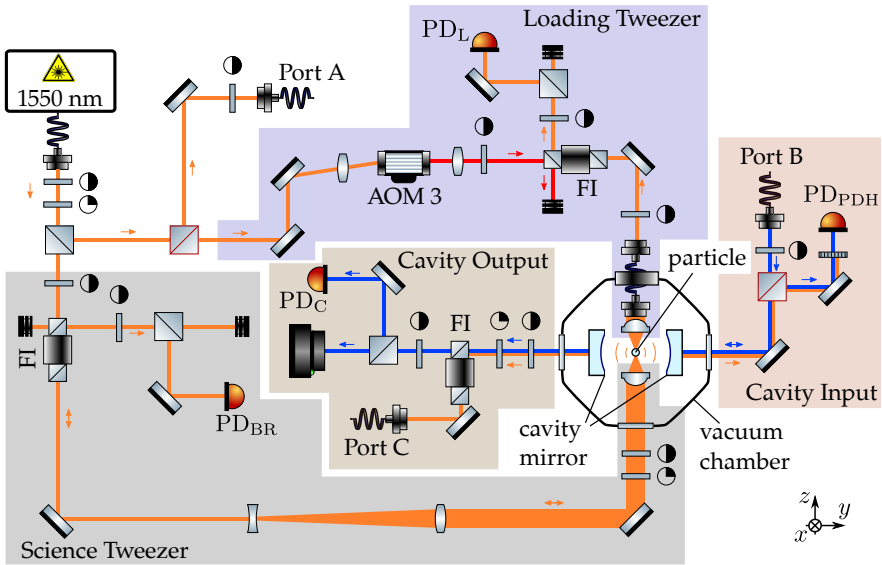
FIGURE 4.15: *Core setup for particle trapping, transfer and detection.* To simplify the sketch, we show components of the detection setup and cavity lock on a separate sketch in Fig. 4.16. We link the ports as indicated by the letter. All beam splitters with a black (red) outline are polarizing (non-polarizing) beam splitters and components labeled FI are Faraday isolators. In Tab. A.2 we list the optical components. All beams are derived from a *NKT Photonics E15* 1550 nm laser. In the sketched configuration, the half wave plate in the loading tweezer section is set to dump all power at the input of a FI. While loading the particle, the tweezer is positioned in a separate vacuum chamber (not shown) and the full power is used to trap a particle. The photodetector PD_L is used to monitor the trapping process. After aligning the loading tweezer with the science tweezer we rotate the half wave plate in front of the FI in the science tweezer section to turn on the science tweezer. At the same time, we rotate the half-wave plate in the loading tweezer section, to turn off the loading tweezer and transfer the particle. From port B we feed in a beam to lock the cavity length by using the signal of the photodetector PD_{PDH}. To reduce noise on the detector we cross polarize the beam w.r.t to the tweezer and use a polarizer to filter out the particle scattered light. On the opposite side of the cavity we use a photodiode to monitor the lock quality PD_c and an infrared camera to image the cavity mode. Mirror A is the high finesse mirror, therefore most of the particle scattered light leaks through mirror B. We feed the light that leaks out of the cavity to port C to detect it with the heterodyne setup.
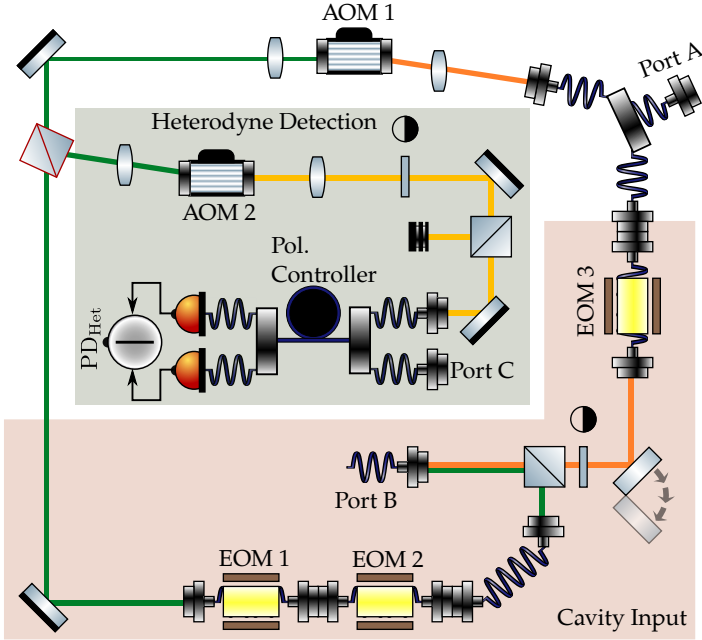
FIGURE 4.16: *Constituent setup for particle detection, cavity locking and calibration.* All components are sketched as described in Fig. 4.15. Light from the core setup enters from the top right through port A. We drive AOM1 (+1st order) and AOM2 (−1st order) at $2\pi \times 80\,\mathrm{MHz}$ and $2\pi \times 79\,\mathrm{MHz}$, resulting in a local oscillator detuning $\Delta_{\mathrm{lo}} = 1\,\mathrm{MHz}$. The heterodyne detection scheme is described in Sec. 2.4.2. As we lock to the TEM_{10} mode of the cavity, we use AOM1 and EOM1 to derive a beam at frequency close to $\omega_{10} - \omega_{00}$. We modulate PDH sidebands with EOM2 as described in Sec. 2.3.3. On the opposite side of the cavity input section, we modulate sidebands on the calibration beam before combining it with the lock beam. We implement a flip mirror to prevent the calibration beam from entering port B and consequently the cavity, while doing measurements. Details on the calibration procedure are described in Sec. 4.4.2.

5

OUTLOOK

When I started my PhD in January 2017, the most promising cooling results were obtained for parametric feedback cooling at a phonon occupation of $n = 63$ and limited by the feedback mechanism itself [51]. A cavity resolved sideband cooling systems, in combination with a Paul trap, had recently succeeded in bringing a levitated particle to pressures below few mbar and reached $n \approx 46k$, limited by signal-to-noise [58]. It seemed like the tools at hand were exhausted and ground-state was not yet reached without a clear path on how to overcome the challenges. When assembling our coherent scattering setup we did not expect that this technique would eventually pave the way to ground-state cooling but merely improve the detection efficiency of the particle motion through Purcell enhancement. In the years after, the field has grown and developed in many directions as summarized in Chapter 1. Not only has it improved the tools at hand, but it found better ones to reach the milestone of ground-state cooling [70, 72, 73].

When we observed the then record cooling performance of our coherent scattering setup [68], despite being designed for other tasks, we replaced the first generation optical tweezer and cavity with a new one that was actually optimized for cavity cooling. We went to great lengths to improve the mechanical stability of our setup to reach phonon numbers $n \approx 10$ and approach ground-state, but had to conclude that further improvement through a particle transfer to a more stable tweezer has to be implemented to go the final distance.

In [99] the path to a variety of quantum applications after reaching ground-state is outlined. A first step there is the coherent coupling between the particle and other quantum systems by achieving a higher coupling than decoherence rate of particle and external quantum system. In current cavity experiments (including ours) the decoherence rate is limited by surrounding gas particles. In order to achieve lower pressures, vacuum loading techniques have to be combined with coherent scattering setups [98]. To increase the coupling rate to an external system, the coupling rate to the cavity has to be increased which in practice also increases the phase noise heating contribution as discussed in Sec. 4.1. To obtain high coupling rates and low phonon numbers one has to fully optimize the position stability of the optical tweezer w.r.t. the optical cavity. Instead of coupling the particle

to an external system, high coupling rates can be achieved by either placing a second quantum system (e.g. particle, atom, ion) into the same optical cavity or coupling two spatial degrees of freedom of one particle via the cavity [176, 177].

In cold atoms experiments full control over all degrees of freedom is desirable to maximize fidelities in coherent quantum networks [37]. To obtain 2D ground-state cooling of a particle, the trapping beam polarization can be rotated, cooling both the x and y motion at the same time at the cavity field node [103]. As the z oscillator can only be cooled at the antinode, which is furthermore limited by phase noise, an additional cooling scheme has to be implemented. The recent free space ground-state cooling experiments are focused on cooling the motion along the tweezer axis and could form a perfect combination with cavity cooling to obtain a 3D ground-state [72, 73].

A

A.1 CLASSICAL NOISE SOURCES IN HETERODYNE DETECTION

In Sec. 4.3 we calculate the implications of phase noise and RIN on the heterodyne detection signal. To focus in the main body on the interpretation of the results, we note certain derivations here.

A.1.1 *Relative Intensity Noise*

We use Eq. (4.21), to define amplitude fluctuations of signal and local oscillator beams as

$$E_s^{(0)}(t - t_0) = \overline{E}_s^{(0)}[1 + \beta_{\text{RIN}} \sin(\Omega t + \psi_0)]$$
$$E_{\text{lo}}^{(0)}(t - (t_0 + \tau_{\text{lo}})) = \overline{E}_{\text{lo}}^{(0)}\{1 + \beta_{\text{RIN}} \sin[\Omega(t - \tau_{\text{lo}}) + \psi_0]\}.$$

We apply the product to sum rule as well as the sum to product rule from App. A.2.1 and derive

$$
\begin{aligned}
\frac{E_s^{(0)}(t - t_0)E_{\text{lo}}^{(0)}(t - (t_0 + \tau_{\text{lo}}))}{\overline{E}_s^{(0)}\overline{E}_{\text{lo}}^{(0)}} = &1 + \frac{\beta_{\text{RIN}}^2}{2}\cos(\Omega\tau_{\text{lo}}) \\
&+ 2\beta_{\text{RIN}}\cos\left(\frac{\Omega\tau_{\text{lo}}}{2}\right) \\
&\times \sin\left(\Omega t + \psi_0 - \frac{\Omega\tau_{\text{lo}}}{2}\right) \\
&- \frac{\beta_{\text{RIN}}^2}{2}\cos(2\Omega t + 2\psi_0 - \Omega\tau_{\text{lo}}). \quad \text{(A.1)}
\end{aligned}
$$

In analogy to the derivation in Sec. 4.3.1, we insert this expression in Eq. (4.13) for $\Delta\phi = 0$ to write the detector signal as

$$\frac{D}{D_0} = \left[1 + \frac{\beta_{\text{RIN}}^2}{2}\cos(\Omega\tau_{\text{lo}})\right]\cos(\Delta\omega t + \phi_0)$$

$$+\beta_{\text{RIN}}\cos\left(\frac{\Omega\tau_{\text{lo}}}{2}\right)\sin\left[(\Delta\omega + \Omega)t + \phi_0 + \psi_0 - \frac{\Omega\tau_{\text{lo}}}{2}\right]$$

$$-\beta_{\text{RIN}}\cos\left(\frac{\Omega\tau_{\text{lo}}}{2}\right)\sin\left[(\Delta\omega - \Omega)t + \phi_0 - \psi_0 + \frac{\Omega\tau_{\text{lo}}}{2}\right]$$

$$-\frac{\beta_{\text{RIN}}^2}{4}\cos[(\Delta\omega + 2\Omega)t + \phi_0 + 2\psi_0 - \Omega\tau_{\text{lo}}]$$

$$-\frac{\beta_{\text{RIN}}^2}{4}\cos[(\Delta\omega - 2\Omega)t + \phi_0 - 2\psi_0 + \Omega\tau_{\text{lo}}]. \tag{A.2}$$

A.1.2 *Phase Noise in Presence of an Optical Cavity*

Instead of going through the derivation of the noise again we want to rely on results obtained in the free space case. To do so we define $\phi_0^{(n)} := \phi_0 + \omega\tau_n$ as well as $\tau_{\text{lo}}^{(n)} := \tau_{\text{lo}} - \tau_n$ and $\psi_0^{(n)} := \psi_0 - \Omega\tau_n$. We assume again phase noise of the form Eq. (4.15). For the phase fluctuation between the local oscillator and $E_{\text{s}}^{(n)}$ (Eq. (4.28)) we write

$$\Delta\phi(t) = \beta_{\text{PN}}\sin\{\Omega[t - (t_0 + \tau_{\text{lo}})] + \psi\} - \beta_{\text{PN}}\sin\{\Omega[t - (t_0 + \tau_n)] + \psi\}$$

$$= -2\beta_{\text{PN}}\sin\left(\frac{\Omega\tau_{\text{lo}}^{(n)}}{2}\right)\cos\left(\Omega t - \frac{\Omega}{2}\tau_{\text{lo}}^{(n)} + \psi_0^{(n)}\right). \tag{A.3}$$

With Eq. (4.18) we derive similarly

$$D_n = \cos(\Delta\omega t + \phi_0^{(n)})$$

$$+\beta_{\text{PN}}\sin\left(\frac{\Omega\tau_{\text{lo}}^{(n)}}{2}\right)\sin\left[(\Delta\omega + \Omega)t + \phi_0^{(n)} + \psi_0^{(n)} - \frac{\Omega\tau_{\text{lo}}^{(n)}}{2}\right]$$

$$+\beta_{\text{PN}}\sin\left(\frac{\Omega\tau_{\text{lo}}^{(n)}}{2}\right)\sin\left[(\Delta\omega - \Omega)t + \phi_0^{(n)} - \psi_0^{(n)} + \frac{\Omega\tau_{\text{lo}}^{(n)}}{2}\right] \tag{A.4}$$

As previously we obtain carrier and sideband signals. The next step is to calculate the infinite sum of the terms D_n to derive the total detector

signal. Since the sidebands and carrier are at different frequencies and don't interfere we can analyse the three terms independently. For the carrier we apply Cor. A.2.1.2 and find the limit of the sum as

$$D_c := -\mathcal{T}D_0 \sum_{n=0}^{\infty} \mathcal{R}^n \cos(\Delta\omega t + \phi_0 + \omega\tau_n)$$

$$\frac{D_c}{\mathcal{T}D_0} = B(\omega)\sin(\Delta\omega t + \omega\tau + \phi_0) - A(\omega)\cos(\Delta\omega t + \omega\tau + \phi_0).$$

Since we have to find similar limits for the sidebands it is convenient to define the coefficients $A(\omega)$ and $B(\omega)$ to simplify the expressions,

$$A(\omega) = \frac{1 - \mathcal{R}\cos(2\omega\tau)}{1 - 2\mathcal{R}\cos(2\omega\tau) + \mathcal{R}^2}$$

$$B(\omega) = \frac{\mathcal{R}\sin(2\omega\tau)}{1 - 2\mathcal{R}\cos(2\omega\tau) + \mathcal{R}^2}.$$

As shown in Theorem A.2.2 we can calculate the interference of the sine and cosine term and derive D_c.

$$D_c = \mathcal{T}D_0 C \sin(\Delta\omega t + \omega\tau + \phi_0 + \Phi)$$

$$C = \sqrt{\frac{1}{(1 - \mathcal{R})^2 + 4\mathcal{R}\sin^2(\omega\tau)}}$$

$$\Phi = \arctan\left[\frac{\mathcal{R}\cos(2\omega\tau) - 1}{\mathcal{R}\sin(2\omega\tau)}\right]$$

We recall the cavity linewidth $\kappa = \frac{1-\mathcal{R}}{\sqrt{\mathcal{R}}}\tau$, cavity resonance frequency ω_c and detuning $\Delta = \omega_c - \omega$. By considering the cavity close to resonance we can expand $\sin(\omega\tau) \approx -\Delta\tau$ and rewrite D_c to obtain the lorentzian lineshape we derived in Sec. 2.3.1.

$$D_c = D_0 \frac{\mathcal{T}}{\mathcal{A} + \mathcal{T}} \sqrt{\frac{(\kappa/2)^2}{(\kappa/2)^2 + \Delta^2}} \sin(\Delta\omega t + \omega\tau + \phi_0 + \Phi) \qquad \text{(A.5)}$$

After deriving again the expected steady-state cavity transfer function for the carrier we will focus now on the transmission of phase noise by looking at the sidebands at $\pm\Omega$ and find the expressions D_Ω^{PN} as

$$
\frac{D_{\Omega}^{\text{PN}}}{D_0} := - \mathcal{T} \beta_{\text{PN}} \sum_{n=0}^{\infty} \mathcal{R}^n \sin\left(\frac{\Omega \tau_{\text{lo}}^{(n)}}{2}\right)
$$

$$
\times \sin\left[(\Delta\omega + \Omega)t + \phi_0^{(n)} + \psi_0^{(n)} - \frac{\Omega \tau_{\text{lo}}^{(n)}}{2}\right]
$$

$$
= \frac{\mathcal{T} \beta_{\text{PN}}}{2} \sum_{n=0}^{\infty} \mathcal{R}^n \{ \; \cos[(\Delta\omega + \Omega)t + \phi_0 + \psi_0 + (\omega - \Omega)\tau_n]
$$

$$
- \cos[(\Delta\omega + \Omega)t + \phi_0 + \psi_0 - \Omega\tau_{\text{lo}} + \omega\tau_n]\}.
$$

As for the carrier we continue by writing the the limit of the infinite sum by applying Cor. A.2.1.2 and find

$$
D_{\Omega}^{\text{PN}} = \frac{\mathcal{T} \beta_{\text{PN}} D_0}{2} \{ A(\omega) \cos[(\Delta\omega + \Omega)t + \phi_0 + \psi_0 + (\omega - \Omega)\tau]
$$

$$
- B(\omega) \sin[(\Delta\omega + \Omega)t + \phi_0 + \psi_0 + (\omega - \Omega)\tau]
$$

$$
- A(\omega + \Omega) \cos[(\Delta\omega + \Omega)t + \phi_0 + \psi_0 - \Omega\tau_{\text{lo}} + \omega\tau]
$$

$$
+ B(\omega + \Omega) \sin[(\Delta\omega + \Omega)t + \phi_0 + \psi_0 - \Omega\tau_{\text{lo}} + \omega\tau]\}.
$$

With Cor. A.2.2.1 we can again calculate the interference signal

$$
D_{\Omega}^{\text{PN}} = \frac{\mathcal{T} \beta_{\text{PN}} D_0}{2} C_{\Omega}^{\text{PN}} \sin[(\Delta\omega + \Omega)t + \Phi_{\Omega}^{\text{PN}}]
$$

$$
C_{\Omega}^{\text{PN}} = \sqrt{C_0(\omega, \Omega) - C_{sc}(\omega, \Omega)},
$$

by defining the functions

$$
\begin{aligned}
C_0(\omega, \Omega) &:= A(\omega)^2 + B(\omega)^2 + A(\omega + \Omega)^2 + B(\omega + \Omega)^2 \\
C_s(\omega, \Omega) &:= 2\sin[|\Omega|(\tau - \tau_{\text{lo}})][B(\omega)A(\omega + \Omega) - A(\omega)B(\omega + \Omega)] \\
C_c(\omega, \Omega) &:= 2\cos[|\Omega|(\tau - \tau_{\text{lo}})][A(\omega)A(\omega + \Omega) + B(\omega)B(\omega + \Omega)] \\
C_{sc}(\omega, \Omega) &:= C_s(\omega, \Omega) + C_c(\omega, \Omega).
\end{aligned}
\tag{A.6}
$$

Furthermore the phase of the transmitted noise sideband are given by

$$
\begin{aligned}
\Phi_c =\;& A(\omega)\sin(\Omega\tau) - B(\omega)\cos(\Omega\tau) \\
& -A(\omega+\Omega)\sin(\Omega\tau_{lo}) + B(\omega+\Omega)\cos(\Omega\tau_{lo}) \\
\Phi_s =\;& A(\omega)\cos(\Omega\tau) + B(\omega)\sin(\Omega\tau) \\
& -A(\omega+\Omega)\cos(\Omega\tau_{lo}) - B(\omega+\Omega)\sin(\Omega\tau_{lo}) \\
\Phi_\Omega^{PN} =\;& \arctan\left(\frac{\Phi_c}{\Phi_s}\right) + \omega\tau + \phi_0 + \psi_0.
\end{aligned}
$$

We can repeat this calculation and derive a similar result for $D_{-\Omega}^{PN}$

$$
\begin{aligned}
D_{-\Omega}^{PN} =\;& \frac{\mathcal{T}\beta_{PN}D_0}{2}C_{-\Omega}^{PN}\sin[(\Delta\omega-\Omega)t + \Phi_{-\Omega}^{PN}] \\
C_{-\Omega}^{PN} =\;& \sqrt{C_0(\omega,-\Omega) - C_{sc}(\omega,-\Omega)} \\
\Phi_c =\;& -A(\omega)\sin(\Omega\tau_{lo}) - B(\omega)\cos(\Omega\tau_{lo}) \\
& +A(\omega-\Omega)\sin(\Omega\tau) + B(\omega-\Omega)\cos(\Omega\tau) \\
\Phi_s =\;& A(\omega)\cos(\Omega\tau_{lo}) - B(\omega)\sin(\Omega\tau_{lo}) \\
& -A(\omega-\Omega)\cos(\Omega\tau) + B(\omega-\Omega)\sin(\Omega\tau) \\
\Phi_{-\Omega}^{PN} =\;& \arctan\left(\frac{\Phi_c}{\Phi_s}\right) + \omega\tau + \phi_0 - \psi_0.
\end{aligned}
$$

Finally we can express the PSD of the heterodyne signal, given the PSD of the input laser phase noise

$$
S_{VV}^{PN}(\Omega) = \frac{(D_0\mathcal{T})^2}{4}S_{\phi\phi}(|\Omega|) \times
\begin{cases}
(C_\Omega^{PN})^2, & \text{for } \Omega > 0 \\
(C_{-\Omega}^{PN})^2, & \text{for } \Omega \leq 0
\end{cases}
\tag{A.7}
$$

A.1.3   *Relative Intensity Noise in Presence of an Optical Cavity*

Using the definitions from the previous sections we consider the case of no phase noise and analyze the influence of an optical cavity on RIN in heterodyne measurements. The interfering fields are given by

$$
\begin{aligned}
E_s^{(0)}(t - (t_0 + \tau_n)) =\;& E_s^{(0)}\{1 + \beta_{RIN}\sin[\Omega(t - \tau_n) + \psi_0]\} \\
E_{lo}^{(0)}(t - (t_0 + \tau_{lo})) =\;& E_{lo}^{(0)}\{1 + \beta_{RIN}\sin[\Omega(t - \tau_{lo}) + \psi_0]\}.
\end{aligned}
$$

We apply the product to sum rule as well as the sum to product rule from App. A.2.1, neglect sidebands at 2Ω that scale with β_{RIN}^2 and derive

$$\frac{E_s^{(0)}\left(t - (t_0 + \tau_n)\right) E_{\text{lo}}^{(0)}\left(t - (t_0 + \tau_{\text{lo}})\right)}{\overline{E}_s^{(0)} \overline{E}_{\text{lo}}^{(0)}} = 1 + \frac{\beta_{\text{RIN}}^2}{2} \cos(\Omega \tau_{\text{lo}}^{(n)})$$

$$+ 2\beta_{\text{RIN}} \cos\left(\frac{\Omega \tau_{\text{lo}}^{(n)}}{2}\right)$$

$$\times \sin\left(\Omega t + \psi_0^{(n)} - \frac{\Omega \tau_{\text{lo}}^{(n)}}{2}\right)$$

We use the result of Eq. (4.22) and derive D_n as

$$D_n = \left[1 + \frac{\beta_{\text{RIN}}^2}{2} \cos(\Omega \tau_{\text{lo}}^{(n)})\right] \cos(\Delta\omega t + \phi_0^{(n)})$$

$$+ \beta_{\text{RIN}} \cos\left(\frac{\Omega \tau_{\text{lo}}^{(n)}}{2}\right) \sin\left[(\Delta\omega + \Omega)t + \phi_0^{(n)} + \psi_0^{(n)} - \frac{\Omega \tau_{\text{lo}}^{(n)}}{2}\right]$$

$$- \beta_{\text{RIN}} \cos\left(\frac{\Omega \tau_{\text{lo}}^{(n)}}{2}\right) \sin\left[(\Delta\omega - \Omega)t + \phi_0^{(n)} - \psi_0^{(n)} + \frac{\Omega \tau_{\text{lo}}^{(n)}}{2}\right] \quad (A.8)$$

Instead of repeating the derivation of the Lorentzian lineshape for the carrier we focus on the first order sidebands at $\pm\Omega$ and find

$$\frac{D_\Omega}{D_0} := -\mathcal{T}\beta_{\text{RIN}} \sum_{n=0}^{\infty} \mathcal{R}^n \cos\left(\frac{\Omega \tau_{\text{lo}}^{(n)}}{2}\right)$$

$$\times \sin\left[(\Delta\omega + \Omega)t + \phi_0^{(n)} + \psi_0^{(n)} - \frac{\Omega \tau_{\text{lo}}^{(n)}}{2}\right]$$

$$= -\frac{\mathcal{T}\beta_{\text{RIN}}}{2} \sum_{n=0}^{\infty} \mathcal{R}^n \{\sin[(\Delta\omega + \Omega)t + \phi_0 + \psi_0 + (\omega - \Omega)\tau_n]$$

$$+ \sin[(\Delta\omega + \Omega)t + \phi_0 + \psi_0 - \Omega\tau_{\text{lo}} + \omega\tau_n]\}.$$

We continue by applying Cor. A.2.1.2 to write the the limit of the infinite sum as

$$D_\Omega = \frac{-\mathcal{T}\beta_{\text{RIN}}D_0}{2}\{A(\omega)\sin[(\Delta\omega+\Omega)t+\phi_0+\psi_0+(\omega-\Omega)\tau]$$
$$+B(\omega)\cos[(\Delta\omega+\Omega)t+\phi_0+\psi_0+(\omega-\Omega)\tau]$$
$$+A(\omega+\Omega)\sin[(\Delta\omega+\Omega)t+\phi_0+\psi_0-\Omega\tau_{\text{lo}}+\omega\tau]$$
$$+B(\omega+\Omega)\cos[(\Delta\omega+\Omega)t+\phi_0+\psi_0-\Omega\tau_{\text{lo}}+\omega\tau]\}$$

and make the result more easily interpretable by calculating the interference signal with Cor. A.2.2.1,

$$D_\Omega = \frac{-\mathcal{T}\beta_{\text{RIN}}D_0}{2}C_\Omega^{\text{RIN}}\sin[(\Delta\omega+\Omega)t+\Phi_\Omega^{\text{RIN}}]$$
$$C_\Omega^{\text{RIN}} = \sqrt{C_0(\omega,\Omega)+C_{sc}(\omega,\Omega)}.$$

The phase of the RIN sidebands are given by

$$\Phi_c = A(\omega)\cos(\Omega\tau)+B(\omega)\sin(\Omega\tau)$$
$$+A(\omega+\Omega)\cos(\Omega\tau_{\text{lo}})+B(\omega+\Omega)\sin(\Omega\tau_{\text{lo}})$$
$$\Phi_s = -A(\omega)\sin(\Omega\tau)+B(\omega)\cos(\Omega\tau)$$
$$-A(\omega+\Omega)\sin(\Omega\tau_{\text{lo}})+B(\omega+\Omega)\cos(\Omega\tau_{\text{lo}})$$
$$\Phi_\Omega^{\text{RIN}} = \arctan\left(\frac{\Phi_c}{\Phi_s}\right)+\omega\tau+\phi_0+\psi_0.$$

Repeating the derivations for the sideband at $-\Omega$ we find the detector signal as

$$D_{-\Omega} = \frac{\mathcal{T}\beta_{\text{RIN}}D_0}{2}C_{-\Omega}^{\text{RIN}}\sin[(\Delta\omega-\Omega)t+\Phi_{-\Omega}^{\text{RIN}}]$$
$$C_{-\Omega}^{\text{RIN}} = \sqrt{C_0(\omega,-\Omega)+C_{sc}(\omega,-\Omega)}$$
$$\Phi_c = A(\omega)\cos(\Omega\tau_{\text{lo}})-B(\omega)\sin(\Omega\tau_{\text{lo}})$$
$$+A(\omega-\Omega)\cos(\Omega\tau)-B(\omega-\Omega)\sin(\Omega\tau)$$
$$\Phi_s = A(\omega)\sin(\Omega\tau_{\text{lo}})+B(\omega)\cos(\Omega\tau_{\text{lo}})$$
$$+A(\omega-\Omega)\sin(\Omega\tau)+B(\omega-\Omega)\cos(\Omega\tau)$$
$$\Phi_{-\Omega}^{\text{RIN}} = \arctan\left(\frac{\Phi_c}{\Phi_s}\right)+\omega\tau+\phi_0-\psi_0$$

Finally we express the PSD of the heterodyne signal, given the PSD of the input laser RIN

$$S_{VV}^{RIN}(\Omega) = \frac{(D_0 \mathcal{T})^2}{16} RIN^2(|\Omega|) \times \begin{cases} (C_{\Omega}^{RIN})^2, & \text{for } \Omega > 0 \\ (C_{-\Omega}^{RIN})^2, & \text{for } \Omega \leq 0 \end{cases}. \tag{A.9}$$

A.2   MATHEMATICS

A.2.1   *Trigonometric Identities*

As stated in Abramowitz & Stegun [180, p. 72-74]. All statements hold for $\theta, \phi \in \mathbb{C}$, although they will be real in the cases considered.

Product to Sum:

$$2\cos(\theta)\cos(\phi) = \cos(\theta - \phi) + \cos(\theta + \phi)$$
$$2\sin(\theta)\sin(\phi) = \cos(\theta - \phi) - \cos(\theta + \phi)$$
$$2\sin(\theta)\cos(\phi) = \sin(\theta + \phi) + \sin(\theta - \phi)$$
$$2\cos(\theta)\sin(\phi) = \sin(\theta + \phi) - \sin(\theta - \phi)$$

Sum to Product:

$$\sin(\theta) \pm \sin(\phi) = 2\sin\left(\frac{\theta \pm \phi}{2}\right)\cos\left(\frac{\theta \mp \phi}{2}\right)$$
$$\cos(\theta) + \cos(\phi) = 2\cos\left(\frac{\theta + \phi}{2}\right)\cos\left(\frac{\theta - \phi}{2}\right)$$
$$\cos(\theta) - \cos(\phi) = -2\sin\left(\frac{\theta + \phi}{2}\right)\sin\left(\frac{\theta - \phi}{2}\right)$$

Euler's Formula:

$$e^{i\phi} = \cos(\phi) + i\sin(\phi)$$
$$2\cos(\phi) = e^{i\phi} + e^{-i\phi}$$
$$2i\sin(\phi) = e^{i\phi} - e^{-i\phi}$$

Angle Sum and Difference:

$$\sin(\theta \pm \phi) = \sin(\theta)\cos(\phi) \pm \cos(\theta)\sin(\phi)$$
$$\cos(\theta \pm \phi) = \cos(\theta)\cos(\phi) \mp \sin(\theta)\sin(\phi)$$

Double Angle:

$$\sin(2\phi) = 2\sin(\phi)\cos(\phi)$$
$$\cos(2\phi) = 2\cos(\phi)^2 - 1 = 1 - 2\sin(\phi)^2$$

Inverse Trigonometric Functions:
The statements hold for $x \in \mathbb{R}$

$$\arctan(x) = \frac{i}{2}\ln\left(\frac{i+x}{i-x}\right)$$
$$\sin(\arctan(x)) = \frac{x}{\sqrt{1+x^2}}$$
$$\cos(\arctan(x)) = \frac{1}{\sqrt{1+x^2}}$$

The first statement can be found in Abramowitz & Stegun [180, p. 80] while the second and third follow easily by inserting the first statement into Euler's Formula.

A.2.2 *Calculus*

Theorem A.2.1 (Geometric Series). *Given $z \in \mathbb{C}$ with $|z| < 1$ the geometric series has the property*

$$\sum_{n=0}^{\infty} z^n = \frac{1}{1-z}.$$

Proof. Given $z \in \mathbb{C}$ and $N \in \mathbb{N}$, let $s(N) = \sum_{n=0}^{N} z^n$ be the N-th partial sum. The following relations hold for $s(N)$,

$$s(N+1) = s(N) + z^{N+1}$$
$$s(N+1) = zs(N) + 1.$$

Combining the two expressions we obtain

$$zs(N) + 1 = s(N) + z^{N+1}$$

$$s(N) = \frac{1 - z^{N+1}}{1 - z}$$

$$\lim_{N \to \infty} s(N) = \frac{1}{1 - z}.$$

□

Corollary A.2.1.1 (Fourier Series). *Given $r \in \mathbb{R}$ with $0 \leq r < 1$ and $\phi \in \mathbb{R}$ it holds*

$$\sum_{n=0}^{\infty} r^n \cos(n\phi) = \frac{1 - r\cos(\phi)}{1 - 2r\cos(\phi) + r^2}$$

$$\sum_{n=0}^{\infty} r^n \sin(n\phi) = \frac{r\sin(\phi)}{1 - 2r\cos(\phi) + r^2}.$$

Proof. Define $z := re^{i\phi}$. We use Theorem A.2.1 to write

$$\sum_{n=0}^{\infty} \left(re^{i\phi}\right)^n = \frac{1}{1 - re^{i\phi}}$$

$$\sum_{n=0}^{\infty} \left(re^{i\phi}\right)^n = \frac{1 - re^{-i\phi}}{(1 - re^{i\phi})(1 - re^{-i\phi})}$$

$$\sum_{n=0}^{\infty} \left(re^{i\phi}\right)^n = \frac{1 - r\cos(\phi)}{1 - 2r\cos(\phi) + r^2} + \frac{r\sin(\phi)i}{1 - 2r\cos(\phi) + r^2}.$$

Furthermore the left hand side can be formulated as

$$\sum_{n=0}^{\infty} \left(re^{i\phi}\right)^n = \sum_{n=0}^{\infty} r^n \cos(n\phi) + i \sum_{n=0}^{\infty} r^n \sin(n\phi).$$

The statement follows from comparing real and imaginary part.   □

Corollary A.2.1.2. *Given $r \in \mathbb{R}$ with $0 \leq r < 1$ and ψ, ω and $\tau \in \mathbb{R}$, as well as $\tau_n := (2n+1)\tau$ it is*

$$\sum_{n=0}^{\infty} r^n \cos(\omega \tau_n + \psi) = \left(\frac{1 - r\cos(2\omega\tau)}{1 - 2r\cos(2\omega\tau) + r^2} \right) \cos(\omega\tau + \psi)$$

$$- \left(\frac{r\sin(2\omega\tau)}{1 - 2r\cos(2\omega\tau) + r^2} \right) \sin(\omega\tau + \psi)$$

$$\sum_{n=0}^{\infty} r^n \sin(\omega \tau_n + \psi) = \left(\frac{1 - r\cos(2\omega\tau)}{1 - 2r\cos(2\omega\tau) + r^2} \right) \sin(\omega\tau + \psi)$$

$$+ \left(\frac{r\sin(2\omega\tau)}{1 - 2r\cos(2\omega\tau) + r^2} \right) \cos(\omega\tau + \psi).$$

Proof. Using the angle sum identity we decompose the cosine as

$$\begin{aligned} \cos(\omega\tau_n + \psi) &= \cos(\omega(2n+1)\tau + \psi) \\ &= \cos(2\omega\tau n)\cos(\omega\tau + \psi) - \sin(2\omega\tau n)\sin(\omega\tau + \psi), \end{aligned}$$

set $\phi := 2\omega\tau$ and write

$$\begin{aligned} \sum_{n=0}^{\infty} r^n \cos(\omega\tau_n + \psi) &= \cos(\omega\tau + \psi) \sum_{n=0}^{\infty} r^n \cos(\phi n) \\ &\quad - \sin(\omega\tau + \psi) \sum_{n=0}^{\infty} r^n \sin(\phi n). \end{aligned}$$

The first statement follows by applying Cor. A.2.1.1. The second statement can be proven analogously. $\qquad\square$

Theorem A.2.2 (Sine and Cosine Sum). *Given $a, b, \omega, t \in \mathbb{R}$ it holds*

$$a\sin(\omega t) + b\cos(\omega t) = \sqrt{a^2 + b^2} \sin\left(\omega t + \arctan\left(\frac{b}{a} \right). \right)$$

Proof. We start with the right hand side of the equation and apply trigonometric identities from above to derive

$$\sin\left(\omega t + \arctan\left(\frac{b}{a}\right)\right) = \cos\left(\arctan\left(\frac{b}{a}\right)\right)\sin(\omega t)$$

$$+ \sin\left(\arctan\left(\frac{b}{a}\right)\right)\cos(\omega t)$$

$$= \left(\frac{a}{\sqrt{a^2 + b^2}}\right)\sin(\omega t)$$

$$+ \left(\frac{b}{\sqrt{a^2 + b^2}}\right)\cos(\omega t).$$

After multiplying by $\sqrt{a^2 + b^2}$ we show the statement. $\qquad\square$

Corollary A.2.2.1 (Trigonometric Sums). *Given $\omega, t \in \mathbb{R}$ and $N \in \mathbb{N}$ and $a_n, \phi_n \in \mathbb{R}, \forall n \in \mathbb{N}$ we can write*

$$\sum_{n=0}^{N} a_n \sin(\omega t + \phi_n) = A\sin(\omega t + \Phi)$$

$$A = \sqrt{\left(\sum_{n=0}^{N} a_n \sin(\phi_n)\right)^2 + \left(\sum_{n=0}^{N} a_n \cos(\phi_n)\right)^2}$$

$$\Phi = \arctan\left(\frac{\sum_{n=0}^{N} a_n \sin(\phi_n)}{\sum_{n=0}^{N} a_n \cos(\phi_n)}\right).$$

Proof. We start with the left hand side of the equation and apply trigonometric identities from above to find

$$\sum_{n=0}^{N} a_n \sin(\omega t + \phi_n) = \sin(\omega t)\sum_{n=0}^{N} a_n \cos(\phi_n) + \cos(\omega t)\sum_{n=0}^{N} a_n \sin(\phi_n).$$

The corollary then directly follows from applying Theorem A.2.2. $\qquad\square$

A.2.3 *Statistics*

We define the variance $\mathrm{var}[f]$, root mean square $\mathrm{RMS}[f]$ and arithmetic mean $E[f]$ of a function $f(t)$ as

$$E[f] = \lim_{T \to \infty} \frac{1}{2T} \int_{-T}^{T} f(t)dt$$

$$\mathrm{var}[f] = \lim_{T \to \infty} \frac{1}{2T} \int_{-T}^{T} f(t)^2 dt$$

$$\mathrm{RMS}[f] = \lim_{T \to \infty} \sqrt{\frac{1}{2T} \int_{-T}^{T} f(t)^2 dt}.$$

For a periodic bounded function, i.e. $f(t + T) = f(t) < \infty, \forall t \in \mathbb{R}$ it suffices to integrate over a period instead of the infinite interval

$$E[f] = \frac{1}{T} \int_{0}^{T} f(t)dt$$

$$\mathrm{var}[f] = \frac{1}{T} \int_{0}^{T} f(t)^2 dt$$

$$\mathrm{RMS}[f] = \sqrt{\frac{1}{T} \int_{0}^{T} f(t)^2 dt}.$$

Proof. We first observe that $f(t)^2$ is a periodic bounded function with $f(t + T)^2 = f(t)^2 < \infty, \forall t \in \mathbb{R}$ if $f(t)$ is periodic and bounded. As the integral over a non-negative function is also non-negative we can square the last line and the statement for the $\mathrm{RMS}[f]$ follows from the one for the $\mathrm{var}[f]$. We now assume $g(t + \tau) = g(t), \forall t \in \mathbb{R}$ and define $N := \lfloor T/\tau \rfloor$ to write

$$\frac{1}{2T} \int_{-T}^{T} g(t)dt = \frac{1}{2T} \sum_{n=0}^{N-1} \left[\int_{n\tau}^{(n+1)\tau} g(t)dt + \int_{-(n+1)\tau}^{-n\tau} g(t)dt \right]$$
$$+ \frac{1}{2T} \left[\int_{N\tau}^{T} g(t)dt + \int_{-T}^{-N\tau} g(t)dt \right].$$

As the integral over a bounded function over a finite interval is also bounded it holds

$$\lim_{T \to \infty} \frac{1}{2T} \left[\int_{N\tau}^{T} g(t)dt + \int_{-T}^{-N\tau} g(t)dt \right] = 0.$$

We continue to investigate the first integral inside the sum and substitute $t' := t - n\tau$ to find

$$\int_{n\tau}^{(n+1)\tau} g(t)dt = \int_0^\tau g(t' + n\tau)dt' = \int_0^\tau g(t')dt'.$$

With the substitution $t' := t - (n - N)\tau$ we can find similarly for the second integral inside the sum

$$\int_{-(n+1)\tau}^{-n\tau} g(t)dt = \int_0^\tau g(t')dt'.$$

We combine these results and derive

$$\lim_{T\to\infty} \frac{1}{2T} \int_{-T}^{T} g(t)dt = \lim_{T\to\infty} \frac{N}{T} \int_0^\tau g(t)dt = \frac{1}{\tau} \int_0^\tau g(t)dt.$$

For the last equality we used that $\lim_{T\to\infty} \lfloor T/\tau \rfloor = T/\tau$.

$\square$

In particular we derive expressions for trigonometric functions, given $\omega, t, \phi_0, \phi_1 \in \mathbb{R}$ and $T = 2\pi/\omega$ as

$$\text{var}[\cos(\omega t + \phi_0))\sin(\omega t + \phi_1)] = \frac{\sin(\phi_1 - \phi_0)}{2}$$
$$\text{var}[\cos(\omega t + \phi_0))\cos(\omega t + \phi_1)] = \frac{\cos(\phi_1 - \phi_0)}{2}$$
$$\text{var}[\sin(\omega t + \phi_0))\sin(\omega t + \phi_1)] = \frac{\cos(\phi_1 - \phi_0)}{2}.$$

Proof. It suffices to show that one of the three statements is correct, since the other two follow by shifting ϕ_0 or ϕ_1 by $\pi/2$ on both sides of the equation. By using the angle sum identities in App. A.2.1 we calculate

$$\cos(\omega t + \phi_0))\sin(\omega t + \phi_1) = (\cos(\omega t)\cos(\phi_0) - \sin(\omega t)\sin(\phi_0))$$
$$\times (\sin(\omega t)\cos(\phi_1) + \cos(\omega t)\sin(\phi_1))$$

Therefore we need to solve the integrals

$$\begin{aligned}
\text{var}[\cos(\omega t + \phi_0))\sin(\omega t + \phi_1)] = &\frac{\cos(\phi_0)\cos(\phi_1)}{T}\int_0^T \cos(\omega t)\sin(\omega t)dt \\
&-\frac{\sin(\phi_0)\sin(\phi_1)}{T}\int_0^T \cos(\omega t)\sin(\omega t)dt \\
&+\frac{\cos(\phi_0)\sin(\phi_1)}{T}\int_0^T \cos(\omega t)^2 dt \\
&-\frac{\sin(\phi_0)\cos(\phi_1)}{T}\int_0^T \sin(\omega t)^2 dt.
\end{aligned}$$

Using the tabulated integrals from Abramowitz & Stegun [180, p. 78] we obtain

$$\text{var}[\cos(\omega t + \phi_0))\sin(\omega t + \phi_1)] = \frac{\cos(\phi_0)\sin(\phi_1)}{2} - \frac{\sin(\phi_0)\cos(\phi_1)}{2}.$$

The statement then follows by applying the trigonometric sum difference rule in reverse.   □

A.3 COMPONENTS

In this section we list components used in the setup, i.e. vacuum parts, mechanical and optical components. We list part numbers in tables, grouped according to the sections of the setup where they are used. We then reference the tables in the thesis.

Name	Manufacturer	Part Number
Science Chamber	Kimball Physics	MCF600-SphOct-F2C8
Loading Chamber	Hositrad	CU35
Electrical Feedthrough	Kurt J. Lesker	IFDGG091053
Viewport	Torr Scientific Ltd.	VPZ38VAR
Gates	Htc vacuum	GVB-SS-CF35-M
Pressure Gauges	Thyracont	VSH89D
Transfer Arm	Thermionics	FLMH-275-50
Turbo Pump	Edwards	nEXT300D
Scroll Pump	Edwards	NXDS6i

TABLE A.1: Vacuum Setup. In addition we use a *Schäfter&Kirchhoff* fiber feedthrough with a part number *V-KF16-PMC-1550-10.1-NA012-APC/APC-90/200-P*.

Name	Manufacturer	Part Number
Laser (1550 nm)	NKT Photonics	Koheras Adjustik E15
AOM	Gooch & Housego	3080
EOM (PDH)	Thorlabs	LN65-10-P-A-A-BNL
Detector PD_{PDH}	MenloSystems	FPD510-FS-NIR
Detector PD_z	Newport	2117-FC-M
Detector $PD_{x,y}$	E. Hebestreit	[114]
Detector PD_c	Thorlabs	PDA20CS2
Infrared Camera	Hamamatsu	C11512-01
Polarizer	Codixx	*colorPol* IR 1300 BC5

TABLE A.2: Components used in the coherent scattering setup. Beam splitters, mirrors and lenses are standard components from Thorlabs, unless otherwise stated.

LIST OF SYMBOLS

Mathematical Symbols

i	imaginary unit
$J_n(\beta)$	n-th Bessel function of the first kind

Physical Constants [181]

ϵ_0	vacuum permittivity	$8.854\,187\,812\,8 \times 10^{-12}\,\mathrm{F\,m^{-1}}$
ϵ_p	dielectric constant of silica at 1550 nm	2.07
$\hbar$	reduced Planck constant	$1.054\,571\,817 \times 10^{-34}\,\mathrm{J\,s}$
c	speed of light in vacuum	$299\,792\,458\,\mathrm{m\,s^{-1}}$
k_B	Boltzmann constant	$1.380\,649 \times 10^{-23}\,\mathrm{J\,K^{-1}}$
M	molar mass of dry air	$28.97 \times 10^{-3}\,\mathrm{kg\,mol^{-1}}$

Common Variables

α	effective polarizability
α_dp	dipole polarizability
Δ	detuning cavity
Δ_lo	detuning local oscillator
κ	cavity linewidth
λ	laser wavelength
λ_c	wave length of cavity mode
λ_tw	wave length of optical tweezer
$\mathcal{A}$	mirror absorption
$\mathcal{F}$	Finesse of an optical cavity
$\mathcal{R}$	mirror reflectivity

$\mathcal{T}$ mirror transmission

NA   numerical aperture

Ω frequency lower than optical frequency

ω optical frequency

ω_c frequency of cavity mode

ω_{fsr} free spectral range of optical cavity

ω_{tw} frequency of optical tweezer

$\bar{n}_{x,y,z}$ average phonon number

ρ particle density

$\boldsymbol{E}$ complex electric field vector

$\boldsymbol{F}_{grad}$ gradient force

$\boldsymbol{F}_{scat}$ scattering force

$\widetilde{S}_{qq}$ single-sided power spectral density of quantity q

$\{\gamma_x, \gamma_y, \gamma_z\}$ dampings of particle motion

$\{\Gamma_x^{(d)}, \Gamma_y^{(d)}, \Gamma_z^{(d)}\}$ single phonon heating rate due to trap displacement noise

$\{\Gamma_x^{(PN)}, \Gamma_y^{(PN)}, \Gamma_z^{(PN)}\}$ single phonon heating rate due to laser phase noise

$\{\Gamma_x^{(RIN)}, \Gamma_y^{(RIN)}, \Gamma_z^{(RIN)}\}$ single phonon heating rate due to RIN

$\{\Gamma_x^{(r)}, \Gamma_y^{(r)}, \Gamma_z^{(r)}\}$ single phonon heating rate due to photon recoil

$\{\Omega_x, \Omega_y, \Omega_z\}$ oscillation frequencies of levitated particle

$\{g_x, g_y, g_z\}$ optomechanical coupling rates

$\{x_{zpf}, y_{zpf}, z_{zpf}\}$ zero-point fluctuation of oscillator $\{x, y, z\}$

a_s real field absorption coefficient

E complex scalar electric field

k wave number

k_c wave number of cavity mode

k_{tw} wave number of optical tweezer

L cavity length

m mass of nanoparticle

$n_{x,y,z}$ n-th vibration level

p gas pressure

P_{tw} optical power

R radius of a particle

r_s, r_A, r_B real field reflection coefficient

S_{qq} double-sided power spectral density of quantity q

T temperature of a thermal bath

t_s, t_A, t_B real field transmission coefficient

$T_{x,y,z}$ effective temperature of particle's c.m. motion

U_0 depth of trapping potential

V particle volume

V_c cavity mode volume

w_c beam waist of cavity mode

w_x beam waist of optical tweezer along polarization axis

w_y beam waist of optical tweezer along cavity axis

x spatial degree of freedom along optical tweezer polarization axis

y spatial degree of freedom along optical cavity axis

z spatial degree of freedom along optical tweezer propagation axis

z_R Rayleigh range of optical tweezer

ROC_A, ROC_B radius of curvature of mirrors A, B

g_A, g_B geometric cavity parameter of mirrors A, B

LIST OF FIGURES

BIBLIOGRAPHY

1. Favero, I. & Marquardt, F. "Focus on optomechanics". *New Journal of Physics* **16** (2014).

2. Weidner, R. T., Sells, R. L., Yearian, M. R. & Meyerhof, W. E. "Elementary Modern Physics". *American Journal of Physics* **30**, 607 (1962).

3. Heisenberg, W. "Über den anschaulichen Inhalt der quantentheoretischen Kinematik und Mechanik". *Zeitschrift für Physik* **43**, 172 (1927).

4. Sen, D. "The uncertainty relations in quantum mechanics". *Current Science* **107**, 203 (2014).

5. Estermann, I. & Stern, O. "Beugung von Molekularstrahlen". *Zeitschrift für Physik* **61**, 95 (1930).

6. Hertz, H. "Ueber einen Einfluss des ultravioletten Lichtes auf die electrische Entladung". *Annalen der Physik* **267**, 983 (1887).

7. Planck, M. "Ueber das Gesetz der Energieverteilung im Normalspectrum". *Annalen der Physik* **309**, 553 (1901).

8. Einstein, A. "Über einen die Erzeugung und Verwandlung des Lichtes betreffenden heuristischen Gesichtspunkt". *Annalen der Physik* **322**, 132 (1905).

9. Millikan, R. A. "A Direct Determination of h." *Physical Review* **4**, 73 (1914).

10. Feynman, R. "The Feynman Lectures on Physics; Vol. I ". *American Journal of Physics* **33**, 750 (1965).

11. Crookes, W. "XV. On attraction and repulsion resulting from radiation". *Philosophical Transactions of the Royal Society* **164**, 501 (1874).

12. Zöllner, F. "Untersuchungen über die Bewegungen strahlender und bestrahlter Körper". *Annalen der Physik* **236**, 296 (1877).

13. Osborne, R. "On certain dimensional properties of matter in the gaseous state. - Part I. Experimental researches on thermal transpiration of gases through porous plates and on the laws of transpiration and impulsion, including an experimental proof that gas is not a continuous plenum. - Part II. On an extension of the dynamical theory of gas, which includes the stresses, tangential and normal, caused by a varying condition of gas, and affords an explanation of the phenomena of transpiration and impulsion". *Philosophical Transactions of the Royal Society* **170**, 727 (1879).

14. Lebedew, P. "Untersuchungen über die Druckkräfte des Lichtes". *Annalen der Physik* **311**, 433 (1901).

15. Nichols, E. F. & Hull, G. F. "The Pressure Due to Radiation. (Second Paper.)" *Physical Review (Series I)* **17**, 26 (1903).

16. Frisch, R. "Experimenteller Nachweis des Einsteinschen Strahlungsrückstoßes". *Zeitschrift für Physik* **86**, 42 (1933).

17. Ashkin, A. "Acceleration and Trapping of Particles by Radiation Pressure". *Physical Review Letters* **24**, 156 (1970).

18. Ashkin, A. & Dziedzic, J. M. "Optical levitation by radiation pressure". *Applied Physics Letters* **19**, 283 (1971).

19. Braginskiǐ, V. B. & Manukin, A. B. "Ponderomotive Effects of Electromagnetic Radiation". *Soviet Journal of Experimental and Theoretical Physics* **25**, 653 (1967).

20. Braginskiǐ, V. B., Manukin, A. B. & Tikhonov, M. Y. "Investigation of Dissipative Ponderomotive Effects of Electromagnetic Radiation". *Soviet Journal of Experimental and Theoretical Physics* **31**, 829 (1970).

21. "Cooling of a Mirror by Radiation Pressure". *Physical Review Letters* **83**, 3174 (1999).

22. Metzger, C. H. & Karrai, K. "Cavity cooling of a microlever". *Nature* **432**, 1002 (2004).

23. Carmon, T., Rokhsari, H., Yang, L., Kippenberg, T. J. & Vahala, K. J. "Temporal Behavior of Radiation-Pressure-Induced Vibrations of an Optical Microcavity Phonon Mode". *Physical Review Letters* **94**, 2 (2005).

24. Arcizet, O., Cohadon, P. F., Briant, T., Pinard, M. & Heidmann, A. "Radiation-pressure cooling and optomechanical instability of a micromirror". *Nature* **444**, 71 (2006).

25. Schliesser, A., Del'Haye, P., Nooshi, N., Vahala, K. J. & Kippenberg, T. J. "Radiation pressure cooling of a micromechanical oscillator using dynamical backaction". *Physical Review Letters* **97**, 243905 (2006).

26. Gigan, S., Böhm, H. R., Paternostro, M., Blaser, F., Langer, G., Hertzberg, J. B., Schwab, K. C., Bäuerle, D., Aspelmeyer, M. & Zeilinger, A. "Self-cooling of a micromirror by radiation pressure". *Nature* **444**, 67 (2006).

27. Kleckner, D. & Bouwmeester, D. "Sub-kelvin optical cooling of a micromechanical resonator". *Nature* **444**, 75 (2006).

28. Favero, I., Metzger, C., Camerer, S., König, D., Lorenz, H., Kotthaus, J. P. & Karrai, K. "Optical cooling of a micromirror of wavelength size". *Applied Physics Letters* **90** (2007).

29. Regal, C. A., Teufel, J. D. & Lehnert, K. W. "Measuring nanomechanical motion with a microwave cavity interferometer". *Nature Physics* **4**, 555 (2008).

30. Thompson, J. D., Zwickl, B. M., Jayich, A. M., Marquardt, F., Girvin, S. M. & Harris, J. G. "Strong dispersive coupling of a high-finesse cavity to a micromechanical membrane". *Nature* **452**, 72 (2008).

31. Corbitt, T. & Mavalvala, N. "Quantum noise in gravitational-wave interferometers". *Journal of Optics B: Quantum and Semiclassical Optics* **6** (2004).

32. O'Connell, A. D., Hofheinz, M., Ansmann, M., Bialczak, R. C., Lenander, M., Lucero, E., Neeley, M., Sank, D., Wang, H., Weides, M., Wenner, J., Martinis, J. M. & Cleland, A. N. "Quantum ground state and single-phonon control of a mechanical resonator". *Nature* **464**, 697 (2010).

33. Chan, J., Alegre, T. P., Safavi-Naeini, A. H., Hill, J. T., Krause, A., Gröblacher, S., Aspelmeyer, M. & Painter, O. "Laser cooling of a nanomechanical oscillator into its quantum ground state". *Nature* **478**, 89 (2011).

34. Teufel, J. D., Donner, T., Li, D., Harlow, J. W., Allman, M. S., Cicak, K., Sirois, A. J., Whittaker, J. D., Lehnert, K. W. & Simmonds, R. W. "Sideband cooling of micromechanical motion to the quantum ground state". *Nature* **475**, 359 (2011).

35. Boozer, A. D., Boca, A., Miller, R., Northup, T. E. & Kimble, H. J. "Cooling to the Ground State of Axial Motion for One Atom Strongly Coupled to an Optical Cavity". *Physical Review Letters* **97**, 083602 (2006).

36. Kaufman, A. M., Lester, B. J. & Regal, C. A. "Cooling a Single Atom in an Optical Tweezer to Its Quantum Ground State". *Physical Review X* **2**, 041014 (2012).

37. Reiserer, A., Nölleke, C., Ritter, S. & Rempe, G. "Ground-State Cooling of a Single Atom at the Center of an Optical Cavity". *Physical Review Letters* **110**, 223003 (2013).

38. Diedrich, F., Bergquist, J. C., Itano, W. M. & Wineland, D. J. "Laser Cooling to the Zero-Point Energy of Motion". *Physical Review Letters* **62**, 403 (1989).

39. Monroe, C., Meekhof, D. M., King, B. E., Jefferts, S. R., Itano, W. M., Wineland, D. J. & Gould, P. "Resolved-Sideband Raman Cooling of a Bound Atom to the 3D Zero-Point Energy". *Physical Review Letters* **75**, 4011 (1995).

40. King, B. E., Wood, C. S., Myatt, C. J., Turchette, Q. A., Leibfried, D., Itano, W. M., Monroe, C. & Wineland, D. J. "Cooling the Collective Motion of Trapped Ions to Initialize a Quantum Register". *Physical Review Letters* **81**, 1525 (1998).

41. Roos, C. S., Leibfried, D., Mundt, A., Schmidt-Kaler, F., Eschner, J. & Blatt, R. "Experimental Demonstration of Ground State Laser Cooling with Electromagnetically Induced Transparency". *Physical Review Letters* **85**, 5547 (2000).

42. Morigi, G., Eschner, J. & Keitel, C. H. "Ground State Laser Cooling Using Electromagnetically Induced Transparency". *Physical Review Letters* **85**, 4458 (2000).

43. Applegate, R. W., Squier, J., Vestad, T., Oakey, J. & Marr, D. W. "Optical trapping, manipulation, and sorting of cells and colloids in microfluidic systems with diode laser bars". *Optics Express* **12**, 4390 (2004).

44. Moffitt, J. R., Chemla, Y. R., Izhaky, D. & Bustamante, C. "Differential detection of dual traps improves the spatial resolution of optical tweezers". *Proceedings of the National Academy of Sciences of the United States of America* **103**, 9006 (2006).

45. Berns, M. W. "Laser Scissors and Tweezers to Study Chromosomes: A Review". *Frontiers in Bioengineering and Biotechnology* **8**, 721 (2020).

46. Matthews, J. N. "Commercial optical traps emerge from biophysics labs". *Physics Today* **62**, 26 (2009).

47. Li, T., Kheifets, S. & Raizen, M. G. "Millikelvin cooling of an optically trapped microsphere in vacuum". *Nature Physics* **7**, 527 (2011).

48. Li, T., Kheifets, S., Medellin, D. & Raizen, M. G. "Measurement of the Instantaneous Velocity of a Brownian Particle". *Science* **328**, 1673 (2010).

49. Gieseler, J., Deutsch, B., Quidant, R. & Novotny, L. "Subkelvin Parametric Feedback Cooling of a Laser-Trapped Nanoparticle". *Physical Review Letters* **109**, 103603 (2012).

50. Ranjit, G., Atherton, D. P., Stutz, J. H., Cunningham, M. & Geraci, A. A. "Attonewton force detection using microspheres in a dual-beam optical trap in high vacuum". *Physical Review A* **91**, 051805 (2015).

51. Jain, V., Gieseler, J., Moritz, C., Dellago, C., Quidant, R. & Novotny, L. "Direct Measurement of Photon Recoil from a Levitated Nanoparticle". *Physical Review Letters* **116**, 243601 (2016).

52. Vovrosh, J., Rashid, M., Hempston, D., Bateman, J., Paternostro, M. & Ulbricht, H. "Parametric feedback cooling of levitated optomechanics in a parabolic mirror trap". *Journal of the Optical Society of America B* **34**, 1421 (2017).

53. Setter, A., Toroš, M., Ralph, J. F. & Ulbricht, H. "Real-time Kalman filter: Cooling of an optically levitated nanoparticle". *Physical Review A* **97**, 033822 (2018).

54. Kiesel, N., Blaser, F., Delić, U., Grass, D., Kaltenbaek, R. & Aspelmeyer, M. "Cavity cooling of an optically levitated submicron particle". *Proceedings of the National Academy of Sciences of the United States of America* **110**, 14180 (2013).

55. Asenbaum, P., Kuhn, S., Nimmrichter, S., Sezer, U. & Arndt, M. "Cavity cooling of free silicon nanoparticles in high vacuum". *Nature Communications* **4**, 2743 (2013).

56. Mestres, P., Berthelot, J., Spasenović, M., Gieseler, J., Novotny, L. & Quidant, R. "Cooling and manipulation of a levitated nanoparticle with an optical fiber trap". *Applied Physics Letters* **107**, 151102 (2015).

57. Millen, J., Fonseca, P. Z. G., Mavrogordatos, T., Monteiro, T. S. & Barker, P. F. "Cavity Cooling a Single Charged Levitated Nanosphere". *Physical Review Letters* **114**, 123602 (2015).

58. Fonseca, P. Z. G., Aranas, E. B., Millen, J., Monteiro, T. S. & Barker, P. F. "Nonlinear Dynamics and Strong Cavity Cooling of Levitated Nanoparticles". *Physical Review Letters* **117**, 173602 (2016).

59. Chang, D. E., Regal, C. A., Papp, S. B., Wilson, D. J., Ye, J., Painter, O., Kimble, H. J. & Zoller, P. "Cavity opto-mechanics using an optically levitated nanosphere". *Proceedings of the National Academy of Sciences of the United States of America* **107**, 1005 (2009).

60. Barker, P. F. & Shneider, M. N. "Cavity cooling of an optically trapped nanoparticle". *Physical Review A* **81**, 023826 (2010).

61. Romero-Isart, O., Juan, M. L., Quidant, R. & Cirac, J. I. "Toward quantum superposition of living organisms". *New Journal of Physics* **12**, 033015 (2010).

62. Yin, Z.-q., Li, T. & Feng, M. "Three-dimensional cooling and detection of a nanosphere with a single cavity". *Physical Review A* **83**, 013816 (2011).

63. Meyer, N., de los Ríos Sommer, A., Mestres, P., Gieseler, J., Jain, V., Novotny, L. & Quidant, R. "Resolved-Sideband Cooling of a Levitated Nanoparticle in the Presence of Laser Phase Noise". *Physical Review Letters* **123**, 153601 (2019).

64. Vuletić, V., Chan, H. W. & Black, A. T. "Three-dimensional cavity Doppler cooling and cavity sideband cooling by coherent scattering". *Physical Review A* **64**, 033405 (2001).

65. Murr, K., Nußmann, S., Puppe, T., Hijlkema, M., Weber, B., Webster, S. C., Kuhn, A. & Rempe, G. "Three-dimensional cavity cooling and trapping in an optical lattice". *Physical Review A* **73**, 063415 (2006).

66. Leibrandt, D., Labaziewicz, J., Vuletić, V. & Chuang, I. "Cavity Sideband Cooling of a Single Trapped Ion". *Physical Review Letters* **103**, 103001 (2009).

67. Hosseini, M., Duan, Y., Beck, K. M., Chen, Y.-T. & Vuletić, V. "Cavity Cooling of Many Atoms". *Physical Review Letters* **118**, 183601 (2017).

68. Windey, D., Gonzalez-Ballestero, C., Maurer, P., Novotny, L., Romero-Isart, O. & Reimann, R. "Cavity-Based 3D Cooling of a Levitated Nanoparticle via Coherent Scattering". *Physical Review Letters* **122**, 123601 (2019).

69. Delić, U., Reisenbauer, M., Grass, D., Kiesel, N., Vuletić, V. & Aspelmeyer, M. "Cavity Cooling of a Levitated Nanosphere by Coherent Scattering". *Physical Review Letters* **122**, 123602 (2019).

70. Delić, U., Reisenbauer, M., Dare, K., Grass, D., Vuletić, V., Kiesel, N. & Aspelmeyer, M. "Cooling of a levitated nanoparticle to the motional quantum ground state". *Science* **367**, 892 (2020).

71. Tebbenjohanns, F., Frimmer, M. & Novotny, L. "Optimal position detection of a dipolar scatterer in a focused field". *Physical Review A* **100**, 043821 (2019).

72. Tebbenjohanns, F., Mattana, M. L., Rossi, M., Frimmer, M. & Novotny, L. "Quantum control of a nanoparticle optically levitated in cryogenic free space". *Nature* **595**, 378 (2021).

73. Magrini, L., Rosenzweig, P., Bach, C., Deutschmann-Olek, A., Hofer, S. G., Hong, S., Kiesel, N., Kugi, A. & Aspelmeyer, M. "Real-time optimal quantum control of mechanical motion at room temperature". *Nature* **595**, 373 (2021).

74. Tebbenjohanns, F., Frimmer, M., Jain, V., Windey, D. & Novotny, L. "Motional Sideband Asymmetry of a Nanoparticle Optically Levitated in Free Space". *Physical Review Letters* **124**, 13603 (2020).

75. Dania, L., Bykov, D. S., Knoll, M., Mestres, P. & Northup, T. E. "Optical and electrical feedback cooling of a silica nanoparticle levitated in a Paul trap". *Physical Review Research* **3**, 013018 (2021).

76. Ranjit, G., Cunningham, M., Casey, K. & Geraci, A. A. "Zeptonewton force sensing with nanospheres in an optical lattice". *Physical Review A* **93**, 053801 (2016).

77. Rodenburg, B., Neukirch, L. P., Vamivakas, A. N. & Bhattacharya, M. "Quantum model of cooling and force sensing with an optically trapped nanoparticle". *Optica* **3**, 318 (2016).

78. Hempston, D., Vovrosh, J., Toroš, M., Winstone, G., Rashid, M. & Ulbricht, H. "Force sensing with an optically levitated charged nanoparticle". *Applied Physics Letters* **111**, 133111 (2017).

79. Hebestreit, E., Frimmer, M., Reimann, R. & Novotny, L. "Sensing Static Forces with Free-Falling Nanoparticles". *Physical Review Letters* **121**, 063602 (2018).

80. Ricci, F., Cuairan, M. T., Conangla, G. P., Schell, A. W. & Quidant, R. "Accurate Mass Measurement of a Levitated Nanomechanical Resonator for Precision Force-Sensing". *Nano Letters* **19**, 6711 (2019).

81. Ahn, J., Xu, Z., Bang, J., Ju, P., Gao, X. & Li, T. "Ultrasensitive torque detection with an optically levitated nanorotor". *Nature Nanotechnology* **15**, 89 (2020).

82. Reimann, R., Doderer, M., Hebestreit, E., Diehl, R., Frimmer, M., Windey, D., Tebbenjohanns, F. & Novotny, L. "GHz Rotation of an Optically Trapped Nanoparticle in Vacuum". *Physical Review Letters* **121**, 033602 (2018).

83. Van Der Laan, F., Reimann, R., Militaru, A., Tebbenjohanns, F., Windey, D., Frimmer, M. & Novotny, L. "Optically levitated rotor at its thermal limit of frequency stability". *Physical Review A* **102**, 013505 (2020).

84. Monteiro, F., Ghosh, S., Van Assendelft, E. C. & Moore, D. C. "Optical rotation of levitated spheres in high vacuum". *Physical Review A* **97**, 051802 (2018).

85. Ahn, J., Xu, Z., Bang, J., Deng, Y. H., Hoang, T. M., Han, Q., Ma, R. M. & Li, T. "Optically Levitated Nanodumbbell Torsion Balance and GHz Nanomechanical Rotor". *Physical Review Letters* **121**, 33603 (2018).

86. Jin, Y., Yan, J., Rahman, S. J., Li, J., Yu, X. & Zhang, J. "6 GHz hyperfast rotation of an optically levitated nanoparticle in vacuum". *Photonics Research* **9**, 1344 (2021).

87. Kuhn, S., Kosloff, A., Stickler, B. A., Patolsky, F., Hornberger, K., Arndt, M. & Millen, J. "Full rotational control of levitated silicon nanorods". *Optica* **4**, 356 (2017).

88. Bang, J., Seberson, T., Ju, P., Ahn, J., Xu, Z., Gao, X., Robicheaux, F. & Li, T. "Five-dimensional cooling and nonlinear dynamics of an optically levitated nanodumbbell". *Physical Review Research* **2**, 43054 (2020).

89. Van Der Laan, F., Tebbenjohanns, F., Reimann, R., Vijayan, J., Novotny, L. & Frimmer, M. "Sub-Kelvin Feedback Cooling and Heating Dynamics of an Optically Levitated Librator". *Physical Review Letters* **127**, 123605 (2021).

90. Neukirch, L. P., Gieseler, J., Quidant, R., Novotny, L. & Vamivakas, N. "A Study of Optically Levitated NV Centers". *The Rochester Conferences on Coherence and Quantum Optics and the Quantum Information and Measurement meeting*, M6.01 (2013).

91. Rahman, A. T. & Barker, P. F. "Laser refrigeration, alignment and rotation of levitated Yb3+:YLF nanocrystals". *Nature Photonics* **11**, 634 (2017).

92. Conangla, G. P., Schell, A. W., Rica, R. A. & Quidant, R. "Motion Control and Optical Interrogation of a Levitating Single Nitrogen Vacancy in Vacuum". *Nano Letters* **18**, 3956 (2018).

93. Perdriat, M., Pellet-Mary, C., Huillery, P., Rondin, L. & Hétet, G. "Spin-Mechanics with Nitrogen-Vacancy Centers and Trapped Particles". *Micromachines* **12** (2021).

94. Rondin, L., Gieseler, J., Ricci, F., Quidant, R., Dellago, C. & Novotny, L. "Direct measurement of Kramers turnover with a levitated nanoparticle". *Nature Nanotechnology* **12**, 1130 (2017).

95. Militaru, A., Innerbichler, M., Frimmer, M., Tebbenjohanns, F., Novotny, L. & Dellago, C. "Escape dynamics of active particles in multistable potentials". *Nature Communications* **12**, 2446 (2021).

96. Militaru, A., Lasanta, A., Frimmer, M., Bonilla, L. L., Novotny, L. & Rica, R. A. "Kovacs Memory Effect with an Optically Levitated Nanoparticle". *Physical Review Letters* **127**, 130603 (2021).

97. De los Ríos Sommer, A., Meyer, N. & Quidant, R. "Strong optomechanical coupling at room temperature by coherent scattering". *Nature Communications* **12**, 276 (2021).

98. Bykov, D. S., Mestres, P., Dania, L., Schmöger, L. & Northup, T. E. "Direct loading of nanoparticles under high vacuum into a Paul trap for levitodynamical experiments". *Applied Physics Letters* **115**, 034101 (2019).

99. Gonzalez-Ballestero, C., Aspelmeyer, M., Novotny, L., Quidant, R. & Romero-Isart, O. "Levitodynamics: Levitation and control of microscopic objects in vacuum". *Science* **374** (2021).

100. Romero-Isart, O., Pflanzer, A. C., Blaser, F., Kaltenbaek, R., Kiesel, N., Aspelmeyer, M. & Cirac, J. I. "Large Quantum Superpositions and Interference of Massive Nanometer-Sized Objects". *Physical Review Letters* **107**, 020405 (2011).

101. Kaltenbaek, R., Hechenblaikner, G., Kiesel, N., Romero-Isart, O., Schwab, K. C., Johann, U. & Aspelmeyer, M. "Macroscopic quantum resonators (MAQRO)". *Experimental Astronomy* **34**, 123 (2012).

102. Stickler, B. A., Papendell, B., Kuhn, S., Schrinski, B., Millen, J., Arndt, M. & Hornberger, K. "Probing macroscopic quantum superpositions with nanorotors". *New Journal of Physics* **20**, 122001 (2018).

103. Gonzalez-Ballestero, C., Maurer, P., Windey, D., Novotny, L., Reimann, R. & Romero-Isart, O. "Theory for cavity cooling of levitated nanoparticles via coherent scattering: Master equation approach". *Physical Review A* **100**, 013805 (2019).

104. Delić, U., Grass, D., Reisenbauer, M., Damm, T., Weitz, M., Kiesel, N. & Aspelmeyer, M. "Levitated cavity optomechanics in high vacuum". *Quantum Science and Technology*, 025006 (2020).

105. "CAS - CERN Accelerator School : Vacuum Technology: Snekersten, Denmark 28 May - 3 Jun 1999. CAS - CERN Accelerator School : Vacuum Technology" (1999).

106. Ashkin, A. & Dziedzic, J. M. "Optical levitation in high vacuum". *Applied Physics Letters* **28**, 333 (1976).

107. Kuo, S. C. & Sheetz, M. P. "Optical tweezers in cell biology". *Trends in Cell Biology* **2**, 116 (1992).

108. Grant, A. "Ashkin, Mourou, and Strickland share 2018 Nobel Prize in Physics". *Physics Today*, 1945 (2018).

109. Ashkin, A. & Dziedzic, J. M. "Feedback stabilization of optically levitated particles". *Applied Physics Letters* **30**, 202 (1977).

110. Chu, S. "Laser Manipulation of Atoms and Particles". *Science* **253**, 861 (1991).

111. Grimm, R., Weidemüller, M. & Ovchinnikov, Y. B. "Optical Dipole Traps for Neutral Atoms". *Advances In Atomic, Molecular, and Optical Physics* **42**, 95 (2000).

112. Millen, J., Monteiro, T. S., Pettit, R. & Nick Vamivakas, A. "Optomechanics with levitated particles". *Reports on Progress in Physics* **83**, 026401 (2020).

113. Gieseler, J. "Dynamics of optically levitated nanoparticles in high vacuum". PhD thesis (ICFO, Universitat Politècnica de Catalunya, 2014).

114. Hebestreit, E. "Thermal Properties of Levitated Nanoparticles". PhD thesis (ETH Zurich, 2017).

115. Maia Neto, P. A. & Nussenzveig, H. M. "Theory of optical tweezers". *Europhysics Letters* **50**, 702 (2000).

116. Callegari, A., Mijalkov, M., Burak Gököz, A. & Volpe, G. "Computational toolbox for optical tweezers in the geometrical optics regime". *Biophotonics Congress: Optics in the Life Sciences Congress 2019 (BODA,BRAIN,NTM,OMA,OMP)* **32** (2019).

117. Tebbenjohanns, F. "Linear feedback cooling of a levitated nanoparticle in free space". PhD thesis (ETH Zurich, 2020).

118. Novotny, L. & Hecht, B. "Principles of Nano-Optics" 2nd ed. (Cambridge University Press, 2012).

119. Hebestreit, E., Reimann, R., Frimmer, M. & Novotny, L. "Measuring the internal temperature of a levitated nanoparticle in high vacuum". *Physical Review A* **97**, 43803 (2018).

120. Clerk, A. A., Devoret, M. H., Girvin, S. M., Marquardt, F. & Schoelkopf, R. J. "Introduction to quantum noise, measurement, and amplification". *Reviews of Modern Physics* **82**, 1155 (2010).

121. Reimann, R. "Cooling and Cooperative Coupling of Single Atoms in an Optical Cavity". PhD thesis (Rheinische Friedrich-Wilhelms-Universität Bonn, 2014).

122. Cardona, M. & Güntherodt, G. "Light Scattering in Solids II" (Springer-Verlag Berlin Heidelberg, 1982).

123. Tanji-Suzuki, H., Leroux, I. D., Schleier-Smith, M. H., Cetina, M., Grier, A. T., Simon, J. & Vuletić, V. "Interaction between Atomic Ensembles and Optical Resonators. Classical Description". *Advances in Atomic, Molecular and Optical Physics* **60**, 201 (2011).

124. Perot, A. & Fabry, C. "On the Application of Interference Phenomena to the Solution of Various Problems of Spectroscopy and Metrology". *The Astrophysical Journal* **9**, 87 (1899).

125. Siegmann, A. E. "Lasers" (University Science Books, 1986).

126. Pulker, H. "Coatings on Glass" 2nd ed. (Elsevier, 1999).

127. Loudon, R. "The Quantum Theory of Light" (Clarendon Press, Oxford, 1973).

128. Mielke, S. L., Ryan, R. E., Hilgeman, T., Lesyna, L., Madonna, R. G. & Van Nostrand, W. C. "Measurements of the phase shift on reflection for low-order infrared Fabry–Perot interferometer dielectric stack mirrors". *Applied Optics* **36**, 8139 (1997).

129. Garmire, E. "Theory of quarter-wave-stack dielectric mirrors used in a thin Fabry-Perot filter". *Applied Optics* **42**, 5442 (2003).

130. Barger, R. L., Sorem, M. & Hall, J. "Frequency stabilization of a cw dye laser". *Applied Physics Letters* **22**, 573 (1973).

131. Drever, R. W. P., Hall, J. L., Kowalski, F. V., Hough, J., Ford, G. M., Munley, a. J. & Ward, H. "Laser phase and frequency stabilization using an optical resonator". *Applied Physics B* **31**, 97 (1983).

132. Black, E. D. "An introduction to Pound–Drever–Hall laser frequency stabilization". *American Journal of Physics* **69**, 79 (2001).

133. Benedikter, J., Hümmer, T., Mader, M., Schlederer, B., Reichel, J., Hänsch, T. W. & Hunger, D. "Transverse-mode coupling and diffraction loss in tunable Fabry–Pérot microcavities". *New Journal of Physics* **17**, 053051 (2015).

134. Mccarron, D. J. "A Guide to Acousto-Optic Modulators". `http://www.jila1.nickersonm.com/papers/AGuidetoAcousto-OpticModulators.pdf`. [Online; accessed 21-February-2021]. (2007).

135. Lawrence, M. J., Willke, B., Husman, M. E., Gustafson, E. K. & Byer, R. L. "Dynamic response of a Fabry–Perot interferometer". *Journal of the Optical Society of America B* **16**, 523 (1999).

136. Malitson, I. H. "Interspecimen Comparison of the Refractive Index of Fused Silica*,†". *Journal of the Optical Society of America* **55**, 1205 (1965).

137. Williams, M. L. "CRC Handbook of Chemistry and Physics, 76th edition". *Occupational and Environmental Medicine* **53**, 504 (1996).

138. Ellis, J. D. "Homodyne and Heterodyne Comparison", 33 (Society of Photo-Optical Instrumentation Engineers, 2014).

139. Gerrard, A. & Burch, J. M. "Introduction to matrix methods in optics" 1st ed. (John Wiley & Sons, Ltd., 1975).

140. Griffiths, D. J. "Introduction to electrodynamics" 4th ed. (Pearson, 2013).

141. Purcell, E. M. "Spontaneous Emission Probabilities at Ratio Frequencies". *Physical Review* **69**, 681 (1946).

142. Motsch, M., Zeppenfeld, M., Pinkse, P. W. & Rempe, G. "Cavity-enhanced Rayleigh scattering". *New Journal of Physics* **12**, 063022 (2010).

143. Donley, E. A., Heavner, T. P., Levi, F., Tataw, M. O. & Jefferts, S. R. "Double-pass acousto-optic modulator system". *Review of Scientific Instruments* **76**, 063112 (2005).

144. Romero-Isart, O., Pflanzer, A., Juan, M., Quidant, R., Kiesel, N., Aspelmeyer, M. & Cirac, J. "Optically levitating dielectrics in the quantum regime: Theory and protocols". *Physical Review A* **83**, 13803 (2011).

145. Beresnev, S. A., Chernyak, V. G. & Fomyagin, G. A. "Motion of a spherical particle in a rarefied gas. Part 2. Drag and thermal polarization". *Journal of Fluid Mechanics* **219**, 405 (1990).

146. Gieseler, J., Quidant, R., Dellago, C. & Novotny, L. "Dynamic relaxation of a levitated nanoparticle from a non-equilibrium steady state". *Nature Nanotechnology* **9**, 358 (2014).

147. Kustura, K., Rusconi, C. C. & Romero-Isart, O. "Quadratic quantum Hamiltonians: General canonical transformation to a normal form". *Physical Review A* **99**, 022130 (2019).

148. Pino, H., Prat-Camps, J., Sinha, K., Venkatesh, B. P. & Romero-Isart, O. "On-chip quantum interference of a superconducting microsphere". *Quantum Science and Technology* **3**, 025001 (2018).

149. Henkel, C., Pötting, S. & Wilkens, M. "Loss and heating of particles in small and noisy traps". *Applied Physics B* **69**, 379 (1999).

150. Hossein-Zadeh, M. & Vahala, K. J. "Observation of optical spring effect in a microtoroidal optomechanical resonator". *Optics Letters* **32**, 1611 (2007).

151. Genes, C., Vitali, D., Tombesi, P., Gigan, S. & Aspelmeyer, M. "Ground-state cooling of a micromechanical oscillator: Comparing cold damping and cavity-assisted cooling schemes". *Physical Review A* **77**, 33804 (2008).

152. Jain, V. "Levitated optomechanics at the photon recoil limit". PhD thesis (ETH Zurich, 2017).

153. Rabl, P., Genes, C., Hammerer, K. & Aspelmeyer, M. "Phase-noise induced limitations on cooling and coherent evolution in optomechanical systems". *Physical Review A* **80**, 1 (2009).

154. Safavi-Naeini, A. H., Gröblacher, S., Hill, J. T., Chan, J., Aspelmeyer, M. & Painter, O. "Squeezed light from a silicon micromechanical resonator". *Nature* **500**, 185 (2013).

155. Hoang, T. M., Ahn, J., Bang, J. & Li, T. "Electron spin control of optically levitated nanodiamonds in vacuum". *Nature Communications* **7**, 12250 (2016).

156. Rahman, A. T., Frangeskou, A. C., Kim, M. S., Bose, S., Morley, G. W. & Barker, P. F. "Burning and graphitization of optically levitated nanodiamonds in vacuum". *Scientific Reports* **6**, 21633 (2016).

157. Lewittes, M., Arnold, S. & Oster, G. "Radiometric levitation of micron sized spheres". *Applied Physics Letters* **40**, 455 (1982).

158. Sato, S., Harada, Y. & Waseda, Y. "Optical trapping of microscopic metal particles". *Optics Letters* **19**, 1807 (1994).

159. Huisken, J. & Stelzer, E. H. K. "Optical levitation of absorbing particles with a nominally Gaussian laser beam". *Optics Letters* **27**, 1223 (2002).

160. Gehm, M. E., O'Hara, K. M., Savard, T. A. & Thomas, J. E. "Dynamics of noise-induced heating in atom traps". *Physical Review A* **58**, 3914 (1998).

161. Hobbs, P. C. D. "Building electro-optical systems" 2nd ed. (John Wiley & Sons, Inc., 2009).

162. Redding, D., Regehr, M. & Sievers, L. "Dynamic models of Fabry-Perot interferometers". *Applied Optics* **41**, 2894 (2002).

163. Kammler, D. W. "A First Course in Fourier Analysis" 1st ed. (Cambridge University Press, 2008).

164. Ronnekleiv, E. "Fiber DFB Lasers for Sensor Applications". PhD thesis (Norwegian University of Science and Technology, 1999).

165. Cranch, G. A., Englund, M. A. & Kirkendall, C. K. "Intensity Noise Characteristics of Erbium-Doped Distributed-Feedback Fiber Lasers". *IEEE Journal of Quantum Electronics* **39**, 1579 (2003).

166. Riehle, F. "Frequency Standards" (WILEY-VCH Verlag GmbH & Co. KGaA, 2004).

167. Schottky, W. "Über spontane Stromschwankungen in verschiedenen Elektrizitätsleitern". *Annalen der Physik* **362**, 541 (1918).

168. Smekal, A. "Zur Quantentheorie der Streuung und Dispersion". *Naturwissenschaften* **16**, 612 (1928).

169. Raman, C. V. & Krishnan, K. S. "A New Type of Secondary Radiation". *Nature* **121**, 501 (1928).

170. Gardiner, D. J. & Graves, P. R. "Practical Raman Spectroscopy" 1st ed. (Springer-Verlag, 1989).

171. Das, R. S. & Agrawal, Y. K. "Raman spectroscopy: Recent advancements, techniques and applications". *Vibrational Spectroscopy* **57**, 163 (2011).

172. Tschannen, C. D., Frimmer, M., Gordeev, G., Vasconcelos, T. L., Shi, L., Pichler, T., Reich, S., Heeg, S. & Novotny, L. "Anti-Stokes Raman Scattering of Single Carbyne Chains". *ACS Nano* **15**, 12249 (2021).

173. Jeanmaire, D. L. & Van Duyne, R. P. "Surface raman spectroelectrochemistry: Part I. Heterocyclic, aromatic, and aliphatic amines adsorbed on the anodized silver electrode". *Journal of Electroanalytical Chemistry and Interfacial Electrochemistry* **84**, 1 (1977).

174. Brenan, C. J. & Hunter, I. W. "Volumetric Raman Microscopy Through a Turbid Medium". *Journal of Raman Spectroscopy* **27**, 561 (1996).

175. Jessen, P. S., Gerz, C., Lett, P. D., Phillips, W. D., Rolston, S. L., Spreeuw, R. J. C. & Westbrook, C. I. "Observation of quantized motion of Rb atoms in an optical field". *Physical Review Letters* **69**, 49 (1992).

176. Ranfagni, A., Vezio, P., Calamai, M., Chowdhury, A., Marino, F. & Marin, F. "Vectorial polaritons in the quantum motion of a levitated nanosphere". *Nature Physics* **17**, 1120 (2021).

177. Toroš, M., Delić, U., Hales, F. & Monteiro, T. S. "Coherent-scattering two-dimensional cooling in levitated cavity optomechanics". *Physical Review Research* **3**, 023071 (2021).

178. Welch, P. "The use of fast Fourier transform for the estimation of power spectra: A method based on time averaging over short, modified periodograms". *IEEE Transactions on Audio and Electroacoustics* **15**, 70 (1967).

179. Ku, H. H. "Notes on the Use of Propagation of Error Formulas". *Journal of Research of the National Bureau of Standards, Section C: Engineering and Instrumentation* **70C**, 263 (1966).

180. Abramowitz, M. & Stegun, I. "Handbook of Mathematical Functions with Formulas, Graphs, and Mathematical Tables" 9th ed. (National Bureau of Standards Applied Mathematics, 1970).

181. Tiesinga, E., Mohr, P. J., Newell, D. B. & Taylor, B. N. "CODATA recommended values of the fundamental physical constants: 2018". *Reviews of Modern Physics* **93**, 025010 (2021).

ACKNOWLEDGMENTS

When I moved to Zurich in 2010 I did not know what to expect. I suppose most people who studied at ETH would agree with the assessment, that the first year is rough. A new environment, a tight schedule and of course Basisprüfung. However, after the first year time starts to fly, Bachelor, Master and not a PhD, but first a job outside of university. After the master thesis, I felt like it is time to see the world of industry. During my internship in Sensirion, I got the chance to join a startup which focused on the fabrication of plasmonic biosensors - my first contact with optics. I knew this is the direction I want to go to in a PhD. I am thankful to Lukas, who gave me a chance to work in his group, despite the different background and for creating an extraordinary work environment with an amazing team. Here I want to take the chance to thank all the people that were part of this journey.

Thank you René, for being a great mentor and friend, inside and outside of the lab. It was great, to not only have the help of an expert on lasers and cavities, but also all kind of everyday problems, ranging from fixing a bike to treating medical conditions. Most people would be bothered by solving the problems of your former co-workers, luckily you enjoy it! Thank you, Barbara and Martin who take care of everything in the lab. Without you two no orders would be placed (or paid) or the Beermol fridge would run empty. Thanks to the current members and alumni of the photonics lab for a great time, playing foosball, having Glühwein and fondue and also working together. There was always someone to discuss and help, no matter the problem. I want to thank Andrei, Fons and Massi for great discussions and proofreading this thesis. The same holds for Johannes and Jaya who already took over the setup and will hopefully enjoy working with it and only rarely wonder "what the hell did René and Dominik think when assembling it". Thanks to Felix and Karol for being the best electronic geeks and to Ronja, Moritz, Anna, Sotos, Jialiang, Mary and Laric for entertaining coffee breaks. Thanks to the sailing enthusiasts, Alfonso and Joanna for a good time on and off the boat and of course to the footballers Cla Duri, Andreas, Lujun, Sebastian, Klaus and Xavi for winning the Boltzmann cup not only once, but twice during the PhD. Especially our first triumph came as a surprise and wouldn't have been possible without Irene. She is not only a perfect addition to any sports team, but also a great friend. Before moving on to the

who are always there to help and support me. I am enormously lucky to have you and wouldn't be here otherwise.

CURRICULUM VITAE

EDUCATION

2013 – 2015	ETH Zürich, Zürich, Switzerland *Final degree:* Master of Science in Physics
2010 – 2013	ETH Zürich (grammar school) Zürich, Switzerland *Final degree:* Bachelor of Science in Physics
– 2010	Schule Schloss Salem (grammar school) Überlingen, Germany

EMPLOYMENT

2017 – 2022	Doctoral Student and Research Assistant *Photonics Laboratory, ETH Zürich*, Zürich, Switzerland
2016 – 2017	Process Engineer *LSPR AG*, Zürich, Switzerland
2015 – 2016	R&D Intern *Sensirion*, Stäfa, Switzerland

PUBLICATIONS

Articles in peer-reviewed journals:

1. **Windey, D.**, Gonzalez-Ballestero, C., Maurer, P., Novotny, L., Romero-Isart, O. & Reimann, R. "Cavity-Based 3D Cooling of a Levitated Nanoparticle via Coherent Scattering". *Physical Review Letters* **122**, 123601 (12 2019).

2. Reimann, R., Doderer, M., Hebestreit, E., Diehl, R., Frimmer, M., **Windey, D.**, Tebbenjohanns, F. & Novotny, L. "GHz Rotation of an Optically Trapped Nanoparticle in Vacuum". *Physical Review Letters* **121**, 033602 (3 2018).

3. Gonzalez-Ballestero, C., Maurer, P., **Windey, D.**, Novotny, L., Reimann, R. & Romero-Isart, O. "Theory for cavity cooling of levitated nanoparticles via coherent scattering: Master equation approach". *Physical Review A* **100**, 013805 (1 2019).

4. Tebbenjohanns, F., Frimmer, M., Jain, V., **Windey, D.** & Novotny, L. "Motional Sideband Asymmetry of a Nanoparticle Optically Levitated in Free Space". *Physical Review Letters* **124**, 013603 (1 2020).

5. Van der Laan, F., Reimann, R., Militaru, A., Tebbenjohanns, F., **Windey, D.**, Frimmer, M. & Novotny, L. "Optically levitated rotor at its thermal limit of frequency stability". *Physical Review A* **102**, 013505 (1 2020).